

Investigation on Alkali-Surfactant-Foam (ASF) for Enhanced Oil Recovery, Experimentally and Theoretically

Hosseini Nasab, Seyed Mojtaba

DOI

[10.4233/uuid:7a4be37b-350a-4fd6-9e16-944cb02a312a](https://doi.org/10.4233/uuid:7a4be37b-350a-4fd6-9e16-944cb02a312a)

Publication date

2017

Document Version

Final published version

Citation (APA)

Hosseini Nasab, S. M. (2017). *Investigation on Alkali-Surfactant-Foam (ASF) for Enhanced Oil Recovery, Experimentally and Theoretically*. [Dissertation (TU Delft), Delft University of Technology]. <https://doi.org/10.4233/uuid:7a4be37b-350a-4fd6-9e16-944cb02a312a>

Important note

To cite this publication, please use the final published version (if applicable). Please check the document version above.

Copyright

Other than for strictly personal use, it is not permitted to download, forward or distribute the text or part of it, without the consent of the author(s) and/or copyright holder(s), unless the work is under an open content license such as Creative Commons.

Takedown policy

Please contact us and provide details if you believe this document breaches copyrights. We will remove access to the work immediately and investigate your claim.

**Investigation on Alkali-
Surfactant-Foam (ASF) for
Enhanced Oil Recovery,
Experimentally and
Theoretically**

Seyed Mojtaba Hosseini Nasab

Investigation on Alkali-Surfactant-Foam (ASF) for Enhanced Oil Recovery, Experimentally and Theoretically

Proefschrift

ter verkrijging van de graad van doctor
aan de Technische Universiteit Delft,
op gezag van de Rector Magnificus Prof.ir. K.C.A.M. Luyben;
voorzitter van het College voor Promoties,
in het openbaar te verdedigen op
dinsdag 5 September 2017 om 15:00 uur

Door

Seyed Mojtaba HOSSEINI NASAB

Master of Science in Chemical Engineering,

Tarbiat Modares University, Tehran, Iran

geboren te Yazd, Iran

This dissertation has been approved by the promotor:

Prof. dr. P. L. J. Zitha

Composition of the doctoral committee:

Rector Magnificus,	chairman
Prof. dr. P. L. J. Zitha	Delft University of Technology, promotor

Independent members:

Dr. F. Douarche	IFP Energies Nouvelles
Prof.dr. W.R. Rossen	Delft University of Technology
Prof. dr. H. Bertin	Université de Bordeaux
Prof.dr. J. Bruining	Delft University of Technology
Prof.dr.ir. T.J. Heimovaara	Delft University of Technology
Dr. K.H.A.A. Wolf	Delft University of Technology
Prof.dr.ir. J.D. Jansen	Delft University of Technology, reserve member



Published and distributed by: S.M. Hosseini Nasab

E-mail: hosseininasab100@gmail.com

This thesis was accomplished with financial support from Ministry of Science, Research and Technology (MSRT), I.R. IRAN.

An electronic version of this dissertation is available at

<http://repository.tudelft.nl/>.

Copyright © 2017 by S.M. Hosseini Nasab

All rights reserved. No part of the material protected by this copyright notice may be reproduced or utilized in any form or by any means, electronic or mechanical, including photocopying, recording or any information storage and retrieval system, without written permission of the author.

چراغ دل به نور جان برافروخت

به نام آن که جان را فکرت آموخت

پدر و مادر عزیزم

تقدیم میکنم به:

To my dear parents: Seyed Mohammad and Ozra

Table of Contents

Chapter 1 Introduction	1
1.1 Enhanced Oil Recovery.....	1
1.2 Gas Injection.....	3
1.3 Foam Flooding	4
1.4 ASF Flooding	6
1.5 Research Objective of Thesis	7
1.6 Thesis Outline.....	9
Chapter 2 Numerical Simulation of Foam Flooding in Porous Media in Absence and Presence of Oil	11
2.1 Abstract	11
2.2 Introduction	12
2.3 Theoretical Description of LE-IT Foam Model	15
2.4 Overview of the Core-flood Experiments	18
2.4.1 Materials and Methods.....	18
2.4.2 Core-flooding Set-up and Procedure	19
2.5 Results and Discussion	22
2.5.1 Numerical Modelling of Foam Flooding in Absence of Oil.....	22
2.5.2 Simulation of Foam Flooding in the Presence of Oil	26
2.6 Conclusions	30
Chapter 3 Mechanistic Modelling of Alkali/Surfactant/Polymer Flooding Process at Under-Optimum Salinity Condition for EOR	33
3.1 Abstract	33
3.2 Introduction	34
3.3 Experiment Materials and Methods.....	39
3.4 Results and Discussion	41
3.4.1 Geochemical Model.....	41
3.4.2 Surfactant Phase Behaviour Simulation.....	42
3.4.3 Bulk Polymer and Surfactant Simulation	44

3.4.4 ASP Flooding Model.....	45
3.5 Sensitivity Analysis	55
3.5.1 Effect of ASP slug size and surfactant concentration.....	56
3.5.2 The combination effect of surfactant concentration and ASP slug size.....	58
3.6 Conclusion	60
Chapter 4 Investigation of Certain Physical-Chemical Features of Oil Recovery by an Optimized Alkali-Surfactant-Foam System	63
4.1 Abstract.....	63
4.2 Introduction	64
4.3 Theoretical Background	66
4.3.1 Entering, Spreading & Bridging Coefficients, Lamella Number.....	66
4.3.2 Surfactant Phase Behaviour	68
4.3.3 Role of Alkalinity in ASF EOR	69
4.4 Experimental Materials and Methods.....	71
4.4.1 Materials.....	71
4.4.2 Micro-emulsion Phase Behaviour Tests.....	71
4.4.3 Surface and Interfacial Tension Measurements	72
4.4.4 Bulk Foam Stability	73
4.4.5 Experiments Overview.....	75
4.5 Results and Discussion	77
4.5.1 Surfactant Phase Behaviour Investigation	77
4.5.2 Bulk Foam Stability	80
4.6 Conclusions	90
Chapter 5 Optimal Alkali/Surfactant/Foam Flooding Process for EOR:A CT Scan Study	93
5.1 Abstract.....	93
5.2 Introduction	94
5.3 Experimental Description	96
5.3.1 Materials.....	96
5.3.2 Core-Flow Experimental Setup.....	97
5.3.3 CT Scan Setting and Processing	98
5.3.4 Experimental Procedure	100
5.4 Results and Discussion	102

5.4.1 Foam flow in porous media in absence of oil	102
5.4.2 Displacement of oil by foam.....	106
5.5 Conclusions	119
Chapter 6 A New Chemical-Enhanced Oil Recovery Method?	121
6.1 Abstract	121
6.2 Introduction	122
6.3 Experimental Description.....	124
6.3.1 Materials	124
6.3.2 Experimental Setup.....	125
6.3.3 Experimental Procedure.....	128
6.4 Results and Discussion	129
6.4.1 Fluids Properties	130
6.4.2 Chemical Flooding.....	131
6.4.3 Capillary Desaturation Curves.....	133
6.5 Conclusion Remarks.....	135
Chapter 7 Summary and Conclusion	137
7.1 Summary	137
7.2 Conclusion.....	138
Bibliography.....	143
List of Figures	155
List of Tables.....	163
Nomenclature.....	165
Acknowledgement.....	167
About the Author.....	171
Scientific Publications	173

Chapter 1

Introduction

1.1 Enhanced Oil Recovery

Worldwide “the race is on” to develop sustainable energy alternatives, including renewable sources such as wind and solar power. The share of oil in the global energy consumption in 2015 was 32.9%, while natural gas had a market share of 23.8% of the primary energy consumption (BP, 2016). The share of renewables, besides hydropower, currently accounts for 2.8% of the primary energy consumption, with wind energy being the largest renewable energy source (BP, 2016). Yet, several industry forecasts predict that by 2030 there will still be a vast huge gap between resource availability and demand, and that fossil fuels will remain the main source of energy supply (“OPEC” 2016). Carbon Capture Utilization and Storage (CCUS) offers opportunities to combine power generation from fossil fuels by reinjecting CO₂ into maturing oil fields. CCUS can enhance energy security by collecting CO₂ and using it for Enhanced Oil Recovery (EOR), while at the same time making hydrocarbon-based power generation carbon neutral. There are currently 14 large-scale CCUS projects in operation around the world, with a further eight under construction. The majority of these projects will utilize CO₂ for EOR (World Energy Outlook, 2016).

A large part of the current oil production comes from mature fields where most of the easy to produce oil reservoirs are already depleted. In addition, the rate of discoveries of new oil reservoirs during the last decades has been declining steadily. As the probability of continuous large new oil discoveries is getting smaller, the costs that are involved in the exploration of

new oil and gas fields around the world become extremely high. To meet the increase in energy demand, the energy sector should increase production. Therefore, increase of the oil recovery factors from mature fields is critical to meet growing energy demands in the coming decades (Alvarado & Manrique, 2010). This could be achieved by the introduction of new technologies for maturing oil fields, such as (Enhanced Oil Recovery) EOR (“IEA”, 2016). Crude oil production from oil reservoirs includes three distinct phases: primary, secondary, and tertiary recovery. Primary oil production utilizes the natural reservoir pressure or lifting to drive oil into the production wellbore. The contribution of primary oil recovery ranges from 15% to 25% of an Oil Initially-In-Place (OIIP) of one reservoir. The secondary recovery phase extends a field’s productive life after pressure depletion of a reservoir, usually by injection of water, or possibly gas, to either maintain the reservoir pressure or displace oil towards a production wellbore. The recovery factor by secondary recovery ranges from 20 to 40% of OIIP (Kokal & Al-Kaabi, 2010). This means that on average between 50% and 70% of identified oil is left behind in the reservoirs.

The main reasons for large amounts of oil to remain unproduced are: 1) capillary forces which cause the trapping of oil, 2) low-permeable and fractured characteristics of reservoir formation, 3) layering and heterogeneity of a reservoir and 4) poor mobility control and poor volumetric sweep efficiency during the secondary phase of oil production. Due to the high demands for energy, the need to improve the recovery factor and to accelerate oil production is of a great importance. The Department of Energy (DoE) of US, and many industry experts are on record in stating that tertiary oil recovery process, known as EOR, offer prospects for producing oil up to 60% - 70% of OIIP after primary and secondary phases (DoE, 2016). EOR includes chemical flooding, miscible and immiscible gas flooding and thermal methods. Although most of the EOR methods are undertaken in the tertiary phase of oil production, several EOR methods, such as miscible CO₂ flooding, low salinity water flooding, and foam injection, can also be applied in the secondary phase of oil production. Chemical EOR, such as polymer flood, surfactants and alkali flooding or a combination of these, can be a solution to increase the mobility control and improve the sweep efficiency by increasing viscosity, and decrease the capillary force by reducing the interfacial tension (IFT). The challenge to EOR lies in the complex interaction of the injected agent(s) with the formation and reservoir fluids

(Schlumberger, 2015). Carbonate reservoirs, that are mainly oil wet and fractured, can pose specific difficulties for a high recovery during water flooding in the secondary phase.

Gas injection, in either continuous or Water-Alternative-Gas (WAG) modes and mainly under miscible conditions, was particularly successful in the USA (Christensen et al., 2001; Crogh et al., 2002). However, both continuous and WAG injection suffer from gas segregation due to gravity override and early breakthrough due to both viscous fingering and channelling through thief zones (Rossen & Shen, 2007). Thermal EOR techniques, such as steam flooding and *in-situ* combustion, have classically been used for recovering heavy oil, since they provide a significant oil viscosity reduction. Thermal EOR methods are not always applicable, for deep reservoirs, due to high capital investment; and even for thin/small reservoirs, that would be economically unjustifiable (Khoshnevis Gargar et al., 2014).

1.2 Gas Injection

Most of the oil production by EOR was, in the past (Jacquard, 1991) as well as in the recent years (OGJ Survey, 2014), produced by gas injection from both oil and gas-condensate reservoirs. It has long been recognized that phase and volumetric behaviour of gas-oil systems during gas injection has a significant effect on oil recovery efficiency. Gas flooding typically includes the injection of CO₂, flue gas, natural gas or nitrogen into oil reservoirs under either miscible or immiscible conditions.

Under miscible conditions injected gas ‘completely mixes’ with oil, forming a new single oleic phase. This leads to lowering of viscosity, swelling of the oleic phase, and reduction of the Interfacial Tension (IFT) between the oleic and water phases. CO₂ flooding above a certain Minimum Miscibility Pressure (MMP) is a typical example of miscible gas flooding where CO₂ behaves as a ‘solvent’ and can potentially recover 100% of the oil initially in place. Under ‘Immiscible’ conditions, injected gas, like nitrogen, does not ‘mix completely’ with the oleic phase. Swelling and viscosity reduction of the oleic phase may still occur if sufficient gas undergoes mass-transfer into the oleic phase. However, swelling and viscosity reduction are limited compared to the miscible flooding conditions. This is the case for CO₂ injection under the MMP, where traditionally one of the main purposes is to provide the energy or drive by

increased pressure. The method of gas injection depends heavily on the availability of gas. Hydrocarbon gases are usually exported. However, in many cases exporting produced gas is either impossible or not economically viable. At Prudhoe Bay (Alaska, USA), it was not economically viable to construct a new pipeline to transport the hydrocarbon gas, which led to the decision to use it for reinjection into the reservoir (McGuire & Holt, 2003). The CO₂ EOR injected into the Permian basin reservoirs in Texas (USA) originates from natural CO₂ reservoirs in Colorado (USA) (Gozalpour et al., 2005). When injection of the gases is the desirable EOR method while no gas is present locally, large investments are necessary to transport the gas to the production site. Therefore, the usage of hydrocarbon gas and CO₂ is limited by its availability and the costs.

Gas injection suffers from poor volumetric sweep efficiency due to gravity segregation, viscous fingering, channelling and through high permeability streaks. These effects are due to low viscosity and density of injected gas compared to oil and reservoir water. For a favourable volumetric sweep efficiency, the mobility ratio between displacing and displaced fluids should be less than unity. One of the most effective methods for achieving this is by foaming the gas.

1.3 Foam Flooding

Foam is a dispersion of a gas phase in a liquid phase, where the thin liquid films (called lamellae) between gas bubbles are stabilized by a surfactant which adsorbs onto the gas/liquid interfaces. The flow of the gas and surfactant solution through the porous media results in *in-situ* foam generation. Foam, in a porous media characteristic of reservoir formation, flows so that the liquid phase is mainly continuous and the gas phase is discontinued by lamellae (Hiraski, 1989). Foam can be used for a gas shut-off, a gas mobility reduction during gas EOR processes, an aquifer remediation, a water shut-off, an acid diversion during matrix acidizing, and for hydraulic fracturing (Rossen, 1996; Schramm et al., 1993). The use of foam can reduce the gas relative permeability (k_{rg}) by trapping the gas in bubbles in the porous media. The presence of bubbles also increases the effective viscosity of the gas phase. These mechanisms lead to a more favourable mobility ratio, which may improve the displacement efficiency of oil in the foam EOR process. Another potential application of foam is conformance control in

heterogeneous reservoirs. Foam has a lower mobility in high permeability layers, which can hinder the flow in a thief zone and consequently divert the foam flow from high to low permeability layers (Kovscek & Radke, 1994; Schramm & Smith, 1996). Thus, foam can improve oil recovery over gas continuous injection or WAG in three main ways: 1) reducing the mobility of displacing fluid (gas or foam) and increasing apparent viscosity of the gas phase, which provides a favourable mobility ratio; 2) blocking a high-permeable swept zone and diverting foam and fluids into the low permeable/un-swept zone; 3) reducing capillary forces by reducing interfacial tensions.

Foam mobility control, an essential foam characteristic for EOR, is controlled by 'foam texture', i.e. the number of lamellae per unit volume of porous media. Foam texture scales like the inversely proportional to the bubble size. It depends on several physical parameters including pore geometry, pore size distribution, surfactant formulation, flow rate, oil saturation etc. Foam texture consisting of small bubble size reduces gas mobility significantly and is called strong foam. There are three main foam generation mechanisms on the pore-level: snap-off, lamellae division, and leave-behind (Schramm & Smith, 1996). Capillary snap-off is one of the most important foam generation mechanism in porous media. Several studies have shown that gas mobility can be reduced several hundred folds when foam is generated by a snap-off mechanism (Ettinger & Radke, 1992). Lamellae, generated by each one of aforementioned three mechanisms, ensure that foam stability is not diminished, as foam is thermodynamically metastable.

Foam stability depends upon capillary pressure, gas diffusion, salinity, disjoining pressure, the anti-foaming effect of oil, surfactant concentration and mechanical distributions. Several experimental studies have shown that oil is detrimental to foam stability at an oil saturation above 5% to 20% (Schramm & Smith, 1996). Thus, foam mobility in the presence of oil is much higher than in the absence of oil, due to the destabilization and coarsening effects of oil on foam (Schramm et al., 1993). Strong foam in porous media can be generated when the pressure gradient is higher than the minimum pressure gradient (Dickson et al., 2002; Falls et al., 1988; Rossen & Bruining, 2007). The minimum pressure gradient for foam generation is a function of porosity, permeability, pore size distribution and total velocity. The minimum

pressure gradient increases with the decrease of permeability (Gauglitz et al., 2002).

Foam flow in porous media in absence of oil exhibits two different flow regimes under steady-state conditions at constant total superficial velocity, depending on the gas fractional flow of foam flow: 1) the low-quality regime and 2) the high-quality regime, where quality indicates the gas fractional flow f_g of foam at the inlet. In the low quality-regime, the pressure gradient is only a function of the superficial velocity of the gas phase, while in the high-quality regime, it is only dependent on the superficial velocity the water phase. Consequently, during the foam quality-scan test at a fixed total Darcy velocity, in the high-quality regime the pressure gradient decreases with increasing foam quality, while in the low-quality regime the pressure gradient increases with increasing foam quality (Kam & Rossen, 2003). As foam strength increases by increasing foam quality, subsequently at a certain water saturation, foam starts to coalesce and dries out suddenly as capillary pressure reaches the ‘limiting capillary pressure (P_{c^*})’. Water saturation at the limiting capillary pressure P_{c^*} , so-called ‘critical water saturation (S_w^*)’, at which the maximum foam strength is reached in the high-quality regime, and below which foam weakens in the low-quality regime. Water saturation is reduced during strong foam flow, which causes a rise of capillary pressure (Khatib et al., 1988). But, if the final capillary pressure is lower than the limiting capillary pressure, foam flow falls in the low-quality regime rather than the high-quality regime.

1.4 ASF Flooding

Alkali-Surfactant-Polymer (ASP) is one of the most attractive chemical-Enhanced Oil Recovery (cEOR) methods. In properly designed ASP formulations, the alkali-surfactant provides ultralow IFT between the drive fluid and the displaced oil, and polymers ensure a good mobility control. Nevertheless, the efficiency of ASP can be much less than expected under various reservoir conditions, such as low permeability, high temperature, high formation brine salinity and the presence of divalent cations (Ca^{+2} , Mg^{+2}) in the formation brine. This is due to polymer degradation and low injectivity, alkali precipitation and scaling in the well and in the surface equipment. Moreover, polymers substantially reduce the capability of the treatment of produced water to be used for re-injection, upcycling or discharge.

This is due to the fact that polymers used for secondary and tertiary oil recovery are linear anionic homopolymers or copolymers, such as hydrolyzed polyacrylamide or acrylamide copolymers. Anionic polymers cause the water phase to have a strong anionic charge, which cannot easily be neutralized by the treatment and processing of the produced polymer water phase. Other restrictions concern the use of high molecular weight polymers in low permeability, High Salinity High Temperature (HPHT) reservoirs. Polymer injectivity is rather low in low permeability reservoirs, which may lead to clogging of the formation or even to unwanted fracturing (Delamaide et al., 2014; Zechner et al., 2013; Zechner, Clemens et al., 2014). Foam offers better properties than polymers for conformance control issues, because of the behaviour of foam with ‘selective mobility reduction’. Foam has been identified as an attractive alternative to polymer in Alkaline-Surfactant-Polymer (ASP) flooding for either low permeability reservoir formations or for reservoirs with high salinity formation water (Guo et al., 2012; Srivastava et al., 2009). Alkali-Surfactant-Foam (ASF) flooding is a new EOR method, which uses foam as a mobility control agent instead of polymer, and provides low IFT to increase the capillary number (Guo et al., 2012). Others have proposed similar processes under the name of Alkali-Surfactant Gas (ASG) or Low Tension Gas (LTG) flooding (Szlendak et al., 2013; Tang et al., 2014; Wu et al., 2010). IFT reduction has led to an increase in the capillary number to improve sweep efficiency (Kang et al., 2010; Yuqiang et al., 2008). For water-flooded oil reservoirs, low IFT-generating formulations, such as ASP and ASF chemical agents, are sought for EOR applications, in order to mobilize the residual oil which is trapped by capillary forces. Surfactant formulations reduce capillary forces, enabling the residual oil to be produced (Iglauer et al., 2010). A process based on surfactant phase behaviour screening has been described for evaluating potential EOR surfactants (Levitt et al., 2009). This approach is based on a well-established relationship between a low IFT and micro-emulsion phase behaviour.

1.5 Research Objective of Thesis

This Ph.D. thesis is aimed at providing further insights and a better understanding of the Alkali-Surfactant-Foam (ASF) flooding process for oil recovery. We wanted to discover the

mechanism of oil displacement by ASF flooding in terms of 1) the formation of oil bank 2) the transport of dispersed oil, 3) the movement and pushing of oil bank(s) and dispersed oil by foam. The main premise of this thesis is, whether immiscible foam flooding as an EOR technique can be improved by ASF flooding in a combination of the mechanisms of ASP EOR and Foam EOR methods? In order to answer this main question of the thesis, the following more specific objectives were formulated:

- Investigation of the dynamic of immiscible foam flow in the porous media at transient and steady-state conditions in the absence and presence of oleic phase by numerical modelling. To this end, we aim to determine the foam model parameters dedicated to the effect of water saturation, surfactant concentration, capillary number (gas velocity) and oil saturation functions.
- Developing of a mechanistic model to explore the causes behind the comparable amount of oil recovery by ASP flooding at under-optimum and at optimum salinity conditions of micro-emulsion phase behaviour. The aim is to use a research simulator, that combines multiphase multicomponent simulation with robust phase behaviour modelling together with the geochemical module.
- Investigating and better understanding of ASF' mechanisms under bulk condition by discovering a synergistic effect between surfactant phase behaviour and foam stability. The focus is on the interaction of ASF chemical agents with oil in the presence and absence of a naphthenic acid component and *in-situ* soap generation. The impact of alkalinity, salinity, IFT reduction and *in-situ* soap generation were systematically studied.
- Investigating why, despite the possibility of generating strong foam in the presence of oil, incremental oil recovery by the foam flooding is limited. To this end, identifying how foam behaves physico-chemically in the oil recovery process from a rock in terms of microscopic displacement of trapped oil and volumetric sweep efficiency.
- Proposing a new chemical EOR approach that has the potential to overcome the drawbacks of chemical EOR methods involving alkali and polymers.

1.6 Thesis Outline

This thesis is based on a number of articles published by the author, describing the results in the research area of ASF flooding EOR process. The dissertation consists of seven chapters.

Chapter 1 is the introduction. The remainder of the thesis is composed of two parts. The first part consists of chapters two and three, and is devoted to numerical simulation and mechanistic modelling of Foam flooding EOR process, and ASP flooding EOR process. The second part includes chapters four to six, and is based on the systematic laboratory experimental study of ASF EOR and the proposal of a novel chemical EOR approach.

Chapter 2 presents an integrated approach for the numerical simulation of foam flooding in a porous media in the absence and presence of oleic phase. To conduct the numerical simulation, a foam model was applied that is based on a Local Equilibrium (LE) and Implicit-Texture (IT). The foam model describes dependency of the foam mobility reduction factor, using several independent functions of the relevant physical variables (liquid saturation, foam velocity, etc.). Firstly, numerical simulations investigated the effect of surfactant concentration on pressure drop across the core in the foam flooding in the absence of oil. Secondly, numerical simulations investigated oil displacement by foam, where the main goal was determining the foam model parameters dedicated to the oil saturation-dependent function.

Chapter 3 is devoted to mechanistic modelling of the alkaline/surfactant/polymer flooding process at under-optimum salinity conditions for EOR. The numerical simulation is based on the recent experimental study of ASP floods, based on a single Internal Olefin Sulfonate (IOS) in natural sandstone cores with varying salinity from under-optimum to optimum conditions, indicating that high recovery factors can also be obtained at under-optimum salinity conditions. Developing a mechanistic model was aimed to explore the causes behind the comparable amount of oil recovery by ASP flooding at under-optimum, and at optimum salinity conditions of micro-emulsion phase behaviour. The results provide a basis to perform improved modelling of the under-optimum salinity series of experiments and optimizing the design of ASP flooding methods for the field scale with more complicated geochemical conditions.

Chapter 4 presents a laboratory study of the ASF method to better understand its mechanisms under the bulk condition. The focus is on the interaction of ASF chemical agents

with oil in the presence and absence of a naphthenic acid component, and *in-situ* soap generation. The impact of alkalinity, salinity, IFT reduction and in-situ soap generation were systematically studied by measurement of 1) surfactant phase behaviour using the glass tube test method, 2) interfacial tension, and 3) foam stability analysis. This approach aimed to discover a synergistic effect between surfactant phase behaviour and foam stability under the bulk conditions, to come up with an optimized ASF EOR process. The method discussed in this study can be successfully applied to formulate high-performance chemical agents for the achievement of the ASF EOR process according to the reservoir fluid condition, i.e. the properties of oil and formation water.

Chapter 5 addresses the question why the incremental oil recovery remains low despite the fact that strong foam was generated. It further explores why a large part of the oil recovered by immiscible foam flooding consists of a mixture with surfactant solutions. The chapter presents an experimental study of an ASF flooding process as a tertiary oil recovery method to improve immiscible foam flooding. The Alkali-Surfactant (AS) formulation, including two anionic surfactant formulations, was formulated: IOS, which exhibits low interfacial tension (IFT), AOS which creates strong foam.

Chapter 6 is directed toward issues of using polymer and alkali in the chemical EOR methods for the low permeable and high salinity reservoirs, that can lead to polymer degradation and low injectivity, alkali precipitation and scaling in the well and in the surface equipment. This chapter reports on an experimental study of a new chemical EOR approach that has the potential to overcome the aforementioned drawbacks. The new chemical formulation consists of the combination of a non-polymeric viscosity enhancement compound and a blend of two surfactants. The performance of this chemical formulation was evaluated by a series of core-flood tests on Bentheimer sandstone cores, under stable gravity conditions, with the aid of X-ray Computed Tomography. A significant reduction in the residual oil saturation was observed by constructing the Capillary Desaturation Curves (CDC), suggesting that the proposed formulation is potentially a robust chemical EOR agent.

Chapter 7 presents the main conclusions of this Ph.D. dissertation.

Chapter 2

Numerical Simulation of Foam Flooding in Porous Media in Absence and Presence of Oil

2.1 Abstract

This chapter reports a series of numerical simulations of foam core-flood experiments in the absence and presence of oil. The experiments consisted of the co-injection of gas and Alpha-Olefin Sulfonate (AOS) surfactant solution into Bentheimer sandstone samples initially saturated with the surfactant solution [see (Simjoo & Zitha, 2013)]. The foam model implemented in the PumaFlow simulator (in-house reservoir simulator of IFPEN) is based on a local equilibrium and describes dependency of foam mobility reduction factor using several independent functions, such as liquid saturation, foam velocity, oil saturation and capillary number.

First, a series of numerical simulation was conducted to investigate the effect of surfactant concentration on pressure drop across the core for the foam flooding in the absence of oil. To this end, the dry-out and gas velocity functions in the foam model were determined from the experimental data obtained at low and high-quality regimes of foam flow at a constant

The content described in this chapter is published in: Hosseini-Nasab et al. "Numerical Simulation of Foam Flooding in Porous Media in Absence and Presence of Oil", 8th International Conference on Porous Media & Annual Meeting (InterPore) on May 9 - 12, 2016, Cincinnati, Ohio, USA.

injection velocity. Next, pressure drop profiles of foam flooding at two different surfactant concentrations were modelled to determine the parameters of the surfactant-dependent function in the foam model. The simulation results fit the experimental data of pressure drops very well.

Then, the numerical simulations investigated the oil displacement, by foam where the main goal was to determine the foam model parameters dedicated to the oil saturation-dependent function. The pressure drop across the core, oil-cut, and oil recovery factor were modelled, and an excellent match was obtained between the pressure profile and the oil recovery obtained numerically compared with those obtained from the corresponding core-flood experiments.

2.2 Introduction

Gas injection for EOR suffers from poor sweep efficiency. Three reasons are associated with this deficiency of gas flooding: 1) segregation and gravity override due to the lower density of gas compared to oil and/or water, 2) viscous fingering due to a high mobility ratio between injected gas and oil and/or water, and 3) channeling through high-permeability streaks or layers in heterogeneous and layered reservoir (Lake et al., 2014). Foam can improve the volumetric sweep efficiency by reducing gas mobility, providing a favourable mobility ratio and contacting a larger fraction of the reservoir to mitigate the effect of heterogeneity, gas segregation and viscous instability (Rossen, 1996; Farajzadeh et al., 2010; Simjoo et al., 2011).

Design of the foam EOR process for field-scale application requires an accurate prediction and description of foam behaviour in porous media with and without the oleic phase. Modelling of foam flow in a porous media can be categorized into two different approaches: the local equilibrium with implicit texture (LE-IT) foam model, and the population balance approach. The LE-IT foam model assumes that a local steady state of foam dynamics in terms of creation and destruction of foam is reached instantaneously, wherever gas and surfactant (as a foaming agent) coexist in porous media (Rossen & Wang, 1999; Boeije & Rossen, 2013; Ma et al., 2015). This model implicitly takes into account the presence of foam generation and coalescence through a mobility interpolation factor, which itself depends on water saturation, gas velocity and other factors (Cheng et al., 2000). Application of the LE-IT foam model for the field-scale requires dependency of the model parameters on the variety of geological

properties of the reservoir, in particular permeability, porosity and fracture geometry in each direction (Farajzadeh et al., 2015). The LE-IT empirical foam model is unable to model the correct foam density as a function of foam quality where the foam quality can vary in thick reservoirs based upon various factors, such as permeability, pore size distribution etc.

The population balance approach describes the dynamics of foam generation and destruction where the foam mobility reduction is based on the bubble size and bubble density (foam texture) (Kovscek et al., 1995; 2010). Although the population balance model provides a comprehensive mechanistic description of foam flow in porous media, it requires many physical parameters which are not easy to determine for the field application. On the other hand, the empirical LE-IT model is more pragmatic and simpler for the field-scale simulation, as it requires fewer simulation parameters and, there are less numerical difficulties and lower computational costs compared to the population balance model (Kapetas et al., 2015; Rossen & Boeije, 2015). Much work in the literature has focused on the simulation of foam flooding in the absence of an oleic phase. Simjoo and Zitha (2015) studied the transient foam flow in an oil-free porous media by using the stochastic bubble population model. The premise of this model is that foam flow in porous media is a complex fluid and bubble generation is a stochastic process. They obtained a good match between the numerically calculated fluid saturation and pressure data compared with those obtained from the experiments at which foam was generated by co-injecting nitrogen and alpha olefin sulfonate surfactant into Bentheimer sandstone. Boeije et al. (2015) proposed a method to calculate the parameters of the water-saturation-dependent function as well as the shear-thinning function from the foam pressure gradient data at low and high-quality regimes at a fixed total velocity. This method can provide the initial estimates for the foam model physical parameters to be used in the reservoir simulator for foam simulation at a large scale. Ma et al. (2013) estimated the parameters of the water-saturation-dependent function to describe the dry-out effect in the absence of the oil phase. In their approach, shear-thinning behaviour at the low-quality regime of foam flooding was ignored.

The effect of permeability variation of porous media on the behaviour of foam flow in the absence of oil was studied experimentally and theoretically by Kepetas et al. (2015). They

showed that permeability can have a significant impact on the critical foam saturation, such that the higher permeability layer exhibits lower critical water saturation (S_w^*). However, they did not come up with a robust correlation between the permeability and the transition abruptness characteristic of the LE-IT foam model for the foam quality-scan experiments at different foam-flow regimes. Jones et al. (2016) fitted the core-flood results of foam flooding without oil for different surfactant concentrations by the LE-IT foam model. To be able to predict the effect of the concentration on the foam apparent viscosity, they extended the model such that five foam parameters vary with surfactant concentration.

Lotfollahi et al. (2015) presented a numerical model to simulate foam flooding in the presence of micro-emulsion phase. However, in this work no validation was given with respect to the experimental data. Similarly, Lashgari et al. (2015) applied the black-oil model system coupled with the micro-emulsion phase behaviour model for simulation of low-tension gas flooding. They used the IFT reduction as the main factor to control the incremental oil recovery, even though this mechanism in foam flooding does not always function. Therefore, most of the research has modelled foam flow in porous media, either in the absence or in the presence of oleic phase. On the other hand, many experimental data of foam flooding for EOR purposes have been reported.

Thus, the aim of this study was to investigate the application of the LE-IT foam model for numerical modelling of foam flow in sandstone rock, both in the absence and in the presence of an oleic phase. The foam model used is similar to that in the CMG-STARSTM simulator (Computer Modelling Group Ltd., 2007). To this end, first the parameters of the dry-out and gas velocity functions in the foam model were determined by a least-square matching of the model to the experimental data obtained at low and high-quality regimes at a constant superficial velocity. Then, numerical simulations were conducted to investigate the effect of the surfactant concentration on the pressure drop across the core sample for the core-flood laboratory data of foam flooding in the absence of oil. Thereafter, the effect of oil on the modelling of foam flooding was elaborated by fitting foam parameters to the experimental data of the foam flooding in the presence of oil.

The structure of this chapter is as follows. First, we describe the main features of the foam

model used in this study. Next we present an overview of the experimental study on foam flooding in sandstone porous media with and without the oleic phase. The chapter proceeds with the simulation results obtained from numerical modelling of the experimental data, and finally the main conclusions are drawn.

2.3 Theoretical Description of LE-IT Foam Model

Features of the local equilibrium and implicit-texture (LE-IT) foam model, in PumaFlow reservoir simulator, are described as follows. Reduction of gas mobility due to presence of a foaming agent is assigned to the relative permeability function, while gas-phase viscosity is assumed unchanged, no matter whether a foaming agent is present or not. The relative permeability reduction factor is interpolated between a (maximum) reference value, known or measured in optimal foaming conditions, and a unity value in the absence of the foaming agent. Gas relative permeability in the presence of foam, k_{rg}^{foam} , is rescaled to gas relative permeability in the absence of foam (i.e. continuous gas), k_{rg}^{gas} , by multiplying k_{rg}^{gas} by a dimensionless interpolation factor, FM .

$$k_{rg}^{foam} = k_{rg}^{gas} \times FM \quad (2-1)$$

The FM function, also known as the mobility reduction factor, is a product of various functions to capture the different physical effects on the foam stability in porous media. The FM function generally includes the contributions of four variables, namely surfactant concentration, water saturation, gas phase velocity and oil saturation.

$$FM = \frac{1}{1 + (M_{ref} - 1)F_1F_2F_3F_4} \quad (2-2)$$

The term M_{ref} is the (reference) maximum foam mobility reduction factor obtained without the impact of other factors (F_1, F_2, \dots). The functions F_1, F_2, F_3 and F_4 incorporate the effects of a foaming agent concentration, water saturation, oil saturation and capillary number (gas phase velocity), respectively. The F_i values are within the range [0; 1]: the closer they are to 1 the more efficient the foam will be. Through the indices (as described in the following part), one

can decide to neglect the dependency on some parameters by simply inputting $e_i = 0$.

$$F_1 = \left[\frac{\text{Min}(\bar{C}_{f,W}, \bar{C}_{f,W}^{ref})}{\bar{C}_{f,W}^{ref}} \right]^{e_s} \quad (2-3)$$

$$F_2 = 0.5 + \frac{\arctan[f_w (S_w - S_w^*)]}{\pi} \quad (2-4)$$

$$F_3 = \left[\frac{\max(0, S_o^* - S_o)}{S_o^*} \right]^{e_o} \quad (2-5)$$

$$F_4 = \left[\frac{N_c^{ref}}{\max(N_c, N_c^{ref})} \right]^{e_c} \quad (2-6)$$

F_1 is a power-law relationship to describe the effect of the foaming agent concentration. It is controlled by parameters $\bar{C}_{f,W}^{ref}$ and e_s , where $\bar{C}_{f,W}^{ref}$ is the critical surfactant concentration above which gas mobility is independent of surfactant concentration (C_s). $\bar{C}_{f,W}^{ref}$ depends on surfactant type and is larger than the Critical Micelle Concentration (CMC). When surfactant concentration is larger than the CMC value, foam becomes more stable due to the increase of disjoining pressure (Kovscek & Radke, 1994; Schramm & Smith, 1996). Note, that the foam coalescence rate is lower than the foam film creation rate, as long as the disjoining pressure is larger than the local capillary pressure (Buchavzov & Stubenrauch, 2007; Ekserova & Krugliakov, 1998; Schulze-Schlarmann et al., 2006).

F_2 is namely a foam dry-out function, which describes the dependency of foam strength on water saturation S_w . S_w^* in the function F_2 is the critical water saturation at which the maximum foam strength is reached in a high-quality regime ('foam quality' referring to gas fractional flow), and below which foam weakens in a low-quality regime (Kam & Rossen, 2003). For the water saturation lower than S_w^* as the foam quality increases, foam (in a high-quality regime) begins to significantly dry out and coarsen by the 'limiting capillary pressure, P_c^* ' (Khatib et al., 1988). During a foam quality-scan test with a fixed superficial velocity, the high-quality regime is the range of foam quality where the pressure gradient decreases with increasing foam quality, while in the low-quality regime the pressure gradient increases with increasing foam

quality (Tanzil et al., 2002). In the F_2 function, f_w is the dry-out coefficient that controls the collapse rate of the foam in the high-quality regime as a function of water saturation (Kapetas et al., 2015). This coefficient (f_w) has a significant effect on the predictions of the pressure gradient, particularly near the transition between the low/high-quality regimes.

Larger values of f_w yield a sharper transition between the high and low-quality regimes, which means that foam dries out faster; while small values cause a gradual transition between the regimes, which means that the foam gradually dries out. If the transition between high and low-quality regimes is abrupt, then the S_w^* parameter corresponds to the water saturation at the limiting capillary pressure P_c^* , i.e. the water saturation at which foam strength collapses (Gauglitz et al., 2002). F_3 represents the destabilization effect of oil on the foam stability. The S_o^* parameter is the oil saturation threshold above which foam is destroyed and the mobility reduction factor decreases. The e_o is the exponent of the function of F_3 , which controls the rate of disappearance of the foam when oil is present. By setting a zero value for this exponent, one can neglect any detrimental effect of the presence of oil on the generated foam and, thus, on the gas mobility control properties.

F_4 is the shear-thinning velocity effect that represents the influence of non-Newtonian power-law shear thinning of foam rheology on the foam strength. It was noted that the apparent foam viscosity decreases as the velocity increases, as result of which the foam behaves as a non-Newtonian shear thinning fluid (Hirasaki & Lawson, 1985; Xu & Rossen, 2003). In the F_4 function, N_c is the capillary number, and $0 < N_c^{ref} < 1$ is a range of reference rheology capillary number values. The capillary number is a dimensionless number, which is defined by the ratio of viscous forces to capillary forces. It is defined by the following equation:

$$N_c = u \times \mu_{app} / \varphi \sigma_{wg} = k \times \nabla p / \sigma_{wg} \quad (2-7)$$

where u is the total Darcy velocity (gas + liquid), μ_{app} is the apparent viscosity of the displacing fluid in the porous media (here i.e. foam), φ is porosity of rock, k is absolute brine-permeability of rock, ∇p is the pressure gradient, and σ_{wg} is the surface tension between gas and foaming agent solution, which is a function of the concentration of the surfactant agent in the aqueous phase. Other definitions of the capillary number have been used in the literature

(Lake et al., 2014), but Eq. (2–7) is the most commonly used for foam flooding (Simjoo et al., 2012). The capillary pressure has an important impact on the foam stability and, in this study, the capillary number is used to model this effect.

Since the maximum value of function F_4 is equal to 1, therefore the value of N_c^{ref} should be set equal to the lowest capillary number expected in the simulations. Below this value of the capillary number (i.e. N_c^{ref}), the shear-thinning behaviour is not represented. The parameter e_C controls the significance of the shear thinning; the larger it is, the stronger the shear-thinning behaviour effect becomes. A value of $e_C = 0$ represents Newtonian behaviour. It is an advantage for foam to be a shear thinning fluid for improved sweep efficiency purposes in reservoir applications, because near the injection wellbore where the velocity is high, the apparent foam viscosity will be low and, thus, the injectivity will be high (Ashoori et al., 2011). However, deep in the reservoir, the apparent foam viscosity will be high, and therefore foam will act as an efficient mobility control agent.

2.4 Overview of the Core-flood Experiments

2.4.1 Materials and Methods

Brine was prepared by adding sodium chloride (NaCl, Merck) at a fixed concentration of 3 wt% in de-ionized water (pH=6.8±0.1). Surfactant solutions with different surfactant concentrations were prepared with the same salinity as the brine. Normal hexadecane (n-C₁₆) with a density of 0.78±0.01 g/cm³ was used as model oil. The surface and interfacial tensions were measured using a KSV Sigma tensiometer by the DuNouy ring method. Surface tension of 1.0 wt% AOS surfactant solution was 28.0 ±0.1 mN/m, and IFT between the surfactant solution and model oil was found to be 1.9 ±0.1 mN/m (both measured at 20°C). The CMC of the AOS solution in the presence of brine was 4.0×10⁻³ wt%. The properties of the chemicals used in this work are summarized in Table 2.1, and the physical properties of the core samples are presented in Table 2.2. Details of the experiment conditions and results can be found elsewhere (Simjoo and Zitha, 2013).

Table 2.1: Properties of the materials used to conduct the experiments at the ambient temperature 21°C and atmospheric pressure

Materials	Formulation	Molecular weight (g/mole)	Viscosity (cP)	Active content (wt%)	Supplier
Salt	NaCl	58.50	solid	99.98	Merck
Oil	n-C16	226.00	3.3 ± 0.01	99.99	Sigma
Surfactant	AOS	315.00	1.08 ± 0.01	40.00	Stepan
Gas	N ₂	28.01	0.017	99.98%	3M
Rock	mainly SiO ₂	--	--	93.00%	Bentheim mine

Table 2.2: Physical properties of the core samples used in the core-flooding experiment

Core sample	Bentheimer
Length (cm)	17.0±0.1
Diameter (cm)	3.8 ±0.1
Porosity (%)	21.0 ±0.1
Pore volume (cm ³)	42.5 ±0.5
Core density (g/ cm ³)	2.65 ±0.02
Brine permeability (Darcy)	2.5 ±0.1

2.4.2 Core-flooding Set-up and Procedure

The set-up used to perform the core-floods is shown schematically in Fig. 2.1. The sequences and conditions used to conduct the core-flooding experiments are summarized in Table 2.3.

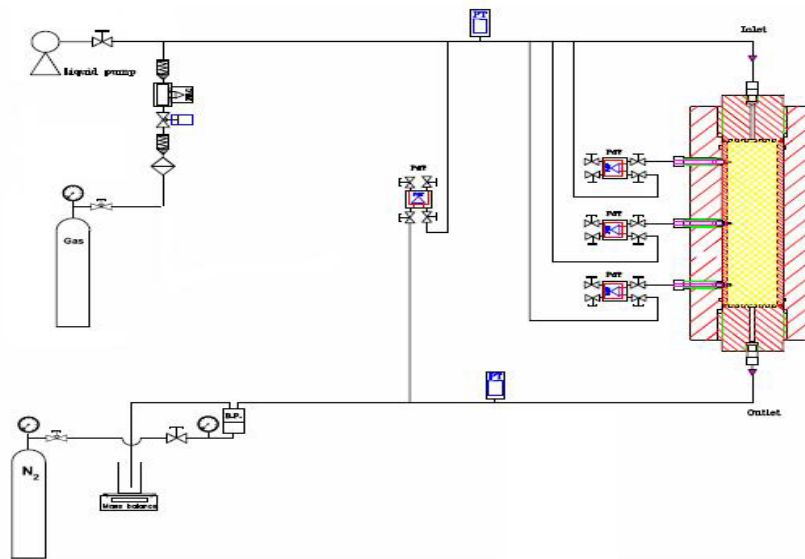


Fig. 2.1: Schematic of the experimental set-up used to perform the core-flooding experiments. The core-holder was held vertically on the bench of the CT scanner.

First, air from the core sample was removed by flushing it with CO_2 at 5 bar injection pressure. Then, the dry core sample was saturated by injecting approximately 10 pore volumes (PV) of brine while increasing back-pressure up to 25 bar. Back pressure was increased to ensure that any CO_2 present in the core was dissolved into the water phase (100% core saturation with brine). For each individual experiment, after core was fully saturated with brine, absolute brine permeability was measured by the standard method (Christiansen & Howarth, 1995). For the experiments in the absence of oil, the core was pre-flushed with a surfactant prior to foam flooding. Surfactant pre-flush was executed to satisfy the adsorption capacity of the rock surface and, thus, to shorten the delay in foam generation. A different injection sequence was undertaken for the experiments mimicking foam EOR: after the core was fully saturated with brine, first, oil was injected into the core till connate water saturation was reached (primary drainage). Then, the core was water-flooded till residual oil was reached (imbibition). Next, similar to the experiments without oil, the core was pre-flushed with a surfactant solution and then subjected to foam flooding.

Table 2.3: Overview of the experimental procedure used for the foam flooding experiments with and without oil

Injection step sequence	Flowrate (cm ³ /min)	Back pressure (bar)	Injection direction
Foam flooding without oil			
CO ₂ flushing to remove air	>20	5	Downward
Core saturation with brine	1.0-6.0	25	Upward
Surfactant preflush	1	20	Upward
Foam flooding (co-injection)	1.1	20	Upward
Foam flooding with oil			
CO ₂ flushing to remove air	>20	5	Downwar
Core saturation with brine	1.0-6.0	25	Upward
Oil injection (drainage)	0.5	5	Downwar
Water flooding (imbibition)	0.5	5	Upward
Surfactant pre-flush	1	20	Upward
Foam flooding (co-injection)	1.1	20	Downwar

Nitrogen gas (N₂) and surfactant solution were co-injected at a fixed superficial velocity of 4.58 ft/day and foam quality 91%, to generate foam *in-situ* at a back-pressure of 20 bar at ambient temperature (21 ± 1°C). Foam quality, f_g , is given by $f_g = q_g / (q_g + q_l) \times 100$, where q_l is flowrate of the liquid phase (surfactant solution), and q_g is flowrate of the gas phase (nitrogen). Gas superficial velocity was determined from its nominal value by applying two corrections: (1) with respect to the calibration factor for the mass flow controller (MFC) towards an adjustment of the pressure before the MFC and injection pressure after the MFC, (2) with respect to the adjustment of the effect of gas compressibility of N₂ due to 30 bar back-pressure. For the foam-quality scan experiments at the low and high-quality regimes, the foam quality was controlled by varying the relative rates of injection of N₂ gas and AOS solution, at a constant nominal total superficial velocity. The steady-state pressure drop was measured when the recorded pressure drop reached a relatively constant value (variations less 0.3 Bar) at a new foam quality.

2.5 Results and Discussion

2.5.1 Numerical Modelling of Foam Flooding in Absence of Oil

The objective of this section is to model the dynamic of foam generation and propagation in porous media in the absence of oil at the transient and steady-state flow conditions. We then model the effect of surfactant concentration on the pressure-gradient build-up during the foam flow. We illustrated the dynamics of foam generation and propagation in the porous media by the mobility reduction of full-strength foam, surfactant concentration effect, the limiting water saturation at which foam collapses, and the parameters governing foam destruction at limiting capillary pressure. To this end, we demonstrated the determination of dedicated parameters to the aforementioned characteristics of foam flow for the LE-IT foam model. First, parameters of the water saturation dependent function (F_I), and the parameters of capillary number dependent function (F_4) were obtained by modelling the pressure gradient core-flood data of one scan of N₂-foam quality at a fixed superficial velocity. In the absence of oil at a fixed surfactant concentration and total velocity, the LE-IT foam model related the foam mobility reduction factor, FM , presented in Eq. (2-2), only to two functions of water saturation and capillary number as follows:

$$FM = \frac{1}{1 + (M_{ref} - 1) \times \left(0.5 + \frac{\tan^{-1}[f_w(S_w - S_w^*)]}{\pi}\right) \times \left(\frac{N_c^{ref}}{\max(N_c, N_c^{ref})}\right)^{e_c}} \quad (2-8)$$

In the absence of foam, Corey-type relative permeability for the water and gas phases were used as follows:

$$k_{rw}(S_w) = k_{rw}^0 \left(\frac{S_w - S_{wc}}{1 - S_{wc} - S_{gr}}\right)^{n_w} \quad (2-9)$$

$$k_{rg}(S_w) = k_{rg}^0 \left(1 - \frac{S_w - S_{wc}}{1 - S_{wc} - S_{gr}}\right)^{n_g} \quad (2-10)$$

where k_{rw}^0 and k_{rg}^0 are the endpoint relative permeabilities for water and gas, respectively,

n_w and n_g are the corresponding exponents, S_{wc} is connate water saturation and S_{gr} is residual gas saturation. The LE-IT foam model captures the value of each function to a maximum of unity. Thus, the value of the reference capillary number (N_c^{ref}) was set equal to the lowest capillary number expected in the simulations, where below this value (N_c^{ref}), shear-thinning behaviour in the low-quality regime does not exist (Kapetas et al., 2015). This implies that N_c^{ref} was not considered a foam matching parameter, while four other independent parameters, M_{ref} , S_w^* , f_w , and e_c , were considered fitting parameters in the low and high-quality regimes of foam flooding in porous media. To determine the parameters, a non-linear least-square optimization was used, in which all the four foam parameters were computed simultaneously. For this, an initial guess and an allowed range were considered for each parameter. Table 2.4 presents the input parameters of rock-fluid properties, the relative permeability parameters of the gas and liquid phases (Eqs. (2–9) and (2–10)), and the conditions of the foam flooding experiment that were implemented in the numerical simulation.

Table 2.4: Input values of rock, fluids and relative permeability parameters in the simulation

Input parameters	Values
Number of grid blocks	1×1×100
Grid block size (m×m×m)	0.0367× 0.0367 ×0.0017
Brine permeability	2.30 (Darcy)
Porosity	0.25
Temperature	21°C
Brine viscosity	1.0 (cP)
Brine density	1.0 (gr/cm ³)
Water compressibility factor	5.0E ⁻⁵
Gas viscosity	0.01744- 0.01832 (cP)
Surfactant concentration	1.0, 0.5, wt%
Salinity (water flooding)	3.0 wt% (NaCl)
Injection flowrate	1.1 (cm ³ /min)
Producer bottom hole pressure	20 bar
Foam injection time	20 (PV)
Connate (irreducible) water saturation	0.15
Residual gas saturation	0
Water relative permeability endpoint	0.25
Gas relative permeability endpoint	0.76
Exponent of water relative permeability	2
Exponent of gas relative permeability	1.3

In order to compute the capillary number, a function describing the dependence of the gas-water surface tension versus the surfactant concentration was implemented. The stabilizing effect of the surfactant concentration on the generated foam was modelled, using the dependence of the capillary number due to the variation of the gas-water surface tension. The values of the foam matching parameters obtained by the least-square optimization method are summarized in Table 2.5. A very good fit of the numerical simulations to the experimental data of steady-state pressure drop of foam flooding was obtained as shown in Fig. 2.2.

Table 2.5: Foam model parameters for the numerical modelling of foam flooding pressure drop at low/high-quality regimes in the absence of an oil phase

Parameters	Values
Reference mobility reduction factor, M_{Ref}	48500
Reference surfactant concentration, $\bar{C}_{f,W}^{ref}$	6 (g/L)
Exponent of surfactant-dependent function, e_s	1.5
Reference capillary number, N_c^{ref}	$9.76E^{-6}$
Critical water saturation, S_w^*	0.16
Constant of driving foam evolution, f_w	1000

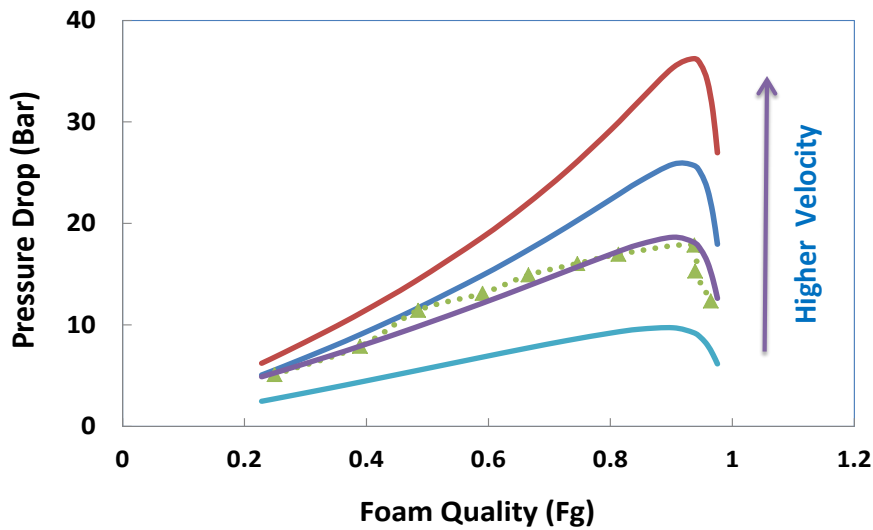


Fig. 2.2: History match of the pressure drop of foam-quality scan experiment without oil at fixed total superficial velocity ($U_g + U_w$) in Bentheimer core by the LE-IT foam model and the simulation parameters presented in Table 2.5., Numerically simulated behaviour of foam-quality scans at a fixed superficial velocity that are higher and lower superficial velocities than the experimental condition are also shown in this figure.

Calculated pressure drops, from the numerical simulation for higher and lower total superficial velocity than the experimental results, are also presented in Fig. 2.2. It illustrates

that the rheological characteristics and foam-flow regimes in a foam quality-scan experiment with the different velocities can also be captured by the numerical results, where the pressure gradient first increased with increasing foam quality, and then, the pressure gradient decreased due to the foam dry-out. The constant of driving foam evolution (f_w) was not considered a large value for the set of data examined in this work, because the transition from low-quality to high-quality regime is not abrupt and the generated foam does not collapse at a constant water saturation as shown in Fig. 2.2.

In order to test the capability of the LE-IT foam model to describe the effect of the surfactant concentration, a numerical simulation of the pressure drop for foam flooding at two different concentrations was performed. Five foam model parameters of dry-out function (F_2) and gas velocity effect (F_4), determined from the previous simulation of foam flood at low/high-quality regimes, were used. Then, the reference surfactant concentration and the exponent of the surfactant-effect function (F_1) of the foam model, by fitting to the experimental data of pressure drop of foam flow at two different concentrations, were estimated as earlier presented in Table 2.5. The foam existence was considered to be a function of the surfactant (foaming agent) concentration and the water saturation. Fig. 2.3 shows numerically calculated pressure drop versus experimental data at transient and steady-state regimes for 0.5 wt% and 1.0 wt% surfactant concentrations.

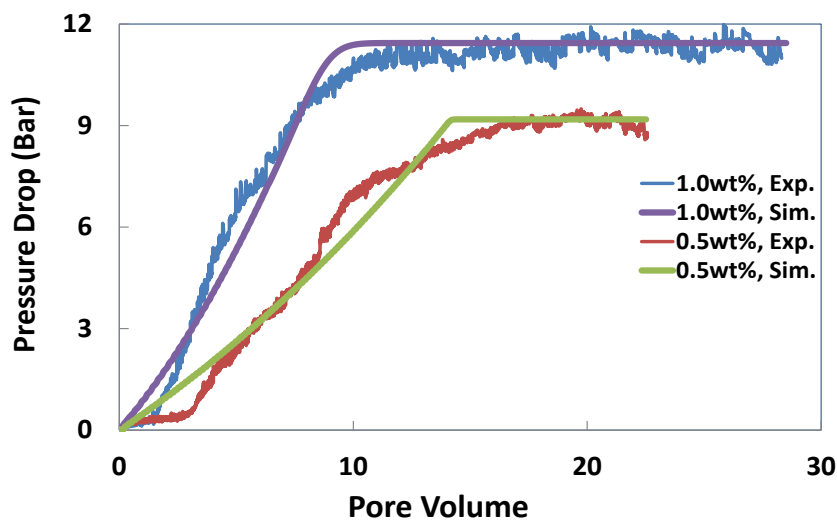


Fig. 2.3: Comparison of numerically calculated and measurement pressure drops of foam flooding in the absence of oil at two different surfactant concentrations. Total superficial velocity and foam quality at injection side of the core was fixed at 4.58 ft/day and 91%, respectively.

The results describe mobilities at a fixed total superficial velocity for the two different surfactant concentrations. The LE-IT foam model successfully captured the experimental fronts and provided a good match for the foam propagation rate at the transient and steady-state conditions. However, initiation of foam generation and propagation by the model are slightly higher than those obtained experimentally. The simulated pressure drop profile in the case of the lower surfactant concentration (0.5 wt%) at the earlier time of the transient state mimics less features of the experimental results, due to the delayed foam generation.

2.5.2 Simulation of Foam Flooding in the Presence of Oil

The objective of this section is the numerical simulation of the core-flood experimental data of immiscible foam flooding during the displacement of the water-flooded remaining oil. Modelling foam propagation through the porous media in the presence of oil is essential to predict the performance of the immiscible foam EOR process. In this section, we assumed that the destabilizing effect of oil on the foam is a function of oil and water saturations. The total foam coalescence rate is the summation of the coalescence rate due to the water dry-out near the limiting water saturation (Eq. (2-4)), and also due to the presence of oil (Eq. (2-5)). Table 2.6 summarizes the input parameters and other conditions of the foam flooding experiment that were implemented in the numerical simulation. The reservoir model, used for the vertical one-dimensional simulation of the core-flow system, had dimensions $1 \times 1 \times 100$ grid blocks. No-flow boundaries were imposed on the lateral sides of the core sample, along with in- and out-flow conditions. Reservoir model was isothermal, with the temperature constant at 22°C , the initial pressure of 20 bar, the porosity of 23% and the permeability was 2.1 Darcy.

Table 2.6: Input values of the parameters of the reservoir model in the simulation

Input parameters	Values
Number of grid blocks	1×1×100
Gris block size (m×m×m)	0.0367 × 0.0367 × 0.0017
Brine permeability	2.1 (Darcy)
Porosity	0.21
Oil viscosity	3.2±0.2 (cP)
Oil density	0.79 (g/cm ³)
Connate (irreducible) water saturation	0.15
Residual oil saturation after water flooding	0.43
Residual oil saturation after foam flooding	0.19
Salinity (water flooding)	3 wt% (NaCl)
Producer bottom hole pressure	20 bar
Injection flowrate	1.1 (cm ³ /min)
Surfactant concentration	1.0 wt%
Foam injection time	18 (PV)
Residual gas saturation	0
Endpoint of water for water/oil relative permeability	0.26
Endpoint of oil for water/oil relative permeability	0.75
Exponent of water for water/oil relative permeability	2.50
Exponent of oil for water/oil relative permeability	1.80
Endpoint of gas for gas/oil relative permeability	0.55
Endpoint of oil for gas/oil relative permeability	0.51
Exponent of gas for gas/oil relative permeability	1.50
Exponent of oil for gas/oil relative permeability	3.10

Immediately before foam flooding, the reservoir model was at the water-flooded residual oil saturation ($S_{or} = 0.44$), with no gas initially present in the core. The injector and producer were placed at opposite ends of the reservoir model, and injection was performed at a rate of 4.2 ft/day. The maximum Bottom-Hole Pressure (BHP) in the injector and producer was set at 50 bar and 30 bar, respectively. N₂ gas and surfactant solution were co-injected at a fixed gas fraction into the flow system of the reservoir model with a uniform water fraction of $f_{wJ}=0.09$ (foam quality of 91%). The binary relative permeability curves between gas/oil and water/oil were used for the 1D displacement simulation. A Corey-type equation was used to describe the relative permeabilities. The binary relative permeability curves were combined into a ternary relative permeability function using the modified ‘Stone I’ three-phase model (Fayers, 1989; Stone, 1973). The three-phase oil relative permeability was computed with the Stone I model and applied to calculate the residual oil saturation parameter. The effects of oil saturation on foam were incorporated by implementing the parameters of F_3 function (Eq. (2–5)) as

presented in Table 2.7. It is essential to note, that the F_i in the FM function were multiplied together. Then, if several parameters are not favorable, then the foam stability will be strongly impacted.

Table 2.7: Foam model parameters for numerical simulation of the pressure drop and oil recovery by foam flooding in the presence of oil

Parameters	Values
Reference mobility reduction factor, M_{Ref}	45000
Critical oil saturation, S_O^*	0.5
Exponent of oil effect function, e_o	0.2
Reference surfactant concentration, $\bar{C}_{f,W}^{ref}$	0.35 wt%
Exponent of surfactant-dependent function, e_s	0.5
Reference capillary number, N_c^{ref}	$9.78E^{-6}$
Exponent of capillary number dependent function, e_c	0.2
Critical water saturation, S_w^*	0.15
Constant driving of foam evolution, (f_w)	100

Fig. 2.4 compares the pressure drop and oil recovery factor (with respect to OIIP) obtained from numerical simulation and the corresponding experiments. The results show a good qualitative agreement between the simulated and measured pressure drop data. The simulated pressure drop increased until reaching a minimum-pressure gradient to generate strong foam in the transient state, and after pressure drop raised, then levelled off to a plateau value during the steady-state condition of foam flow regime. One can see small fluctuations in the pressure drop after the chemical breakthrough for the experimental data and modelling results. Fig. 2.4 shows a good match of the simulated and measured oil recovery by immiscible foam flooding. However, there is a small discrepancy between the simulated and measured oil recovery data between 1.5 and 3.0 PV, most likely due to the lower oil relative permeability during experiment. Thus, this plot (Fig. 2.4) demonstrates an acceptable fit to the series of pressure drops and oil recover factor at both the transient and steady-state conditions of foam generation and propagation through the porous media.

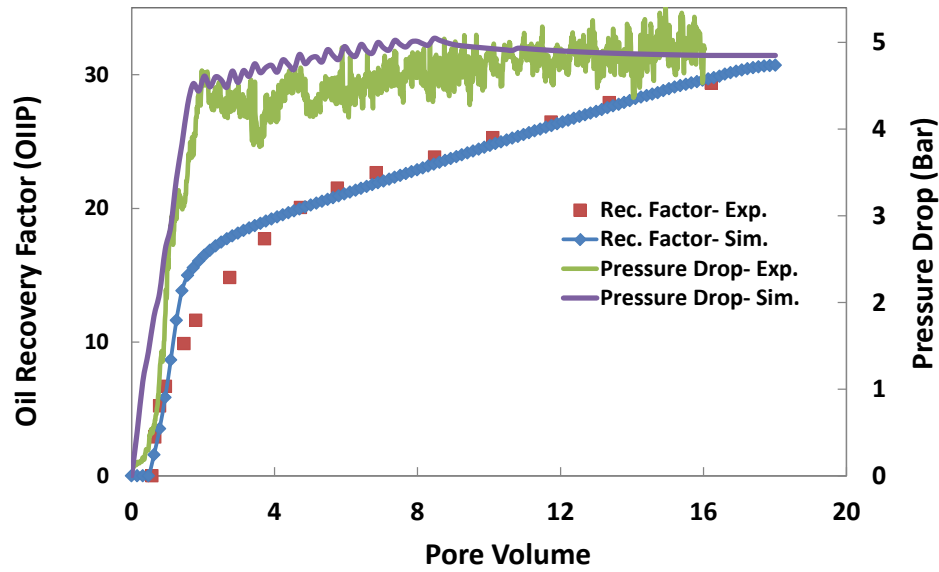


Fig. 2.4: Comparison of numerically calculated and measured pressure drops and oil recovery factor (OIIP) during oil displacement by foam flooding.

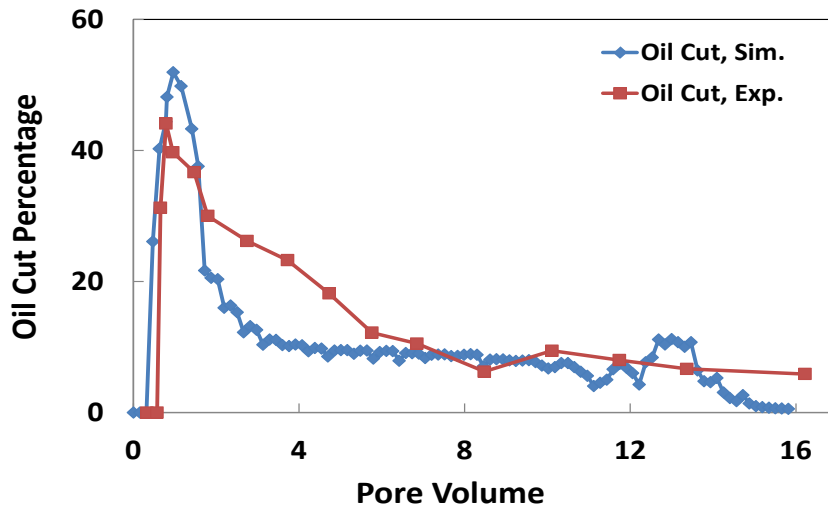


Fig. 2.5: Comparison of numerically calculated and measured oil-cut by foam flooding.

Fig. 2.5 compares the oil-cut (normalized oil production rate) profile obtained from numerical simulation with those obtained from the experiments. The numerically predicted oil-cut profile is in a good agreement with the one obtained from the experiment. In the first 1.2 pore volumes, the oil-cut increases until it reaches a peak value of 54 % and, then, decreases towards 5.8% over more than 15 pore volumes. Visual inspection of the effluents showed that in the first 1.8 PV clean oil was produced, while after oil was produced as an oil-in-water emulsion (Simjoo & Zitha, 2013). This means that foam flooding first induces the formation of

an oil bank and then, after the breakthrough of the trailing edge of the oil bank, the diffuse oil is obtained as a dispersed phase. The above oil production features, due to foam flooding, i.e. oil bank followed by a long tailing oil recovery, were captured remarkably well by the numerical simulations. The tailing oil production occurred during the highest capillary number (or pressure build-up, see Fig. 2.5), and the produced oil was attributed to the emulsified oil. The desaturation of the oleic phase from the core can also be elaborated from the series of CT scan images obtained during foam flooding as presented in Fig. 2.6. The red color corresponds to the liquid phase consisting of residual oil plus surfactant solution. As gas and surfactant solution were co-injected from the top of the core, the intensity of the orange colour diminishes from the left to right progressively in favour of more blue, corresponding the three-phase flow. This gives a qualitative impression of the change in fluid saturations including oil saturation in the core.

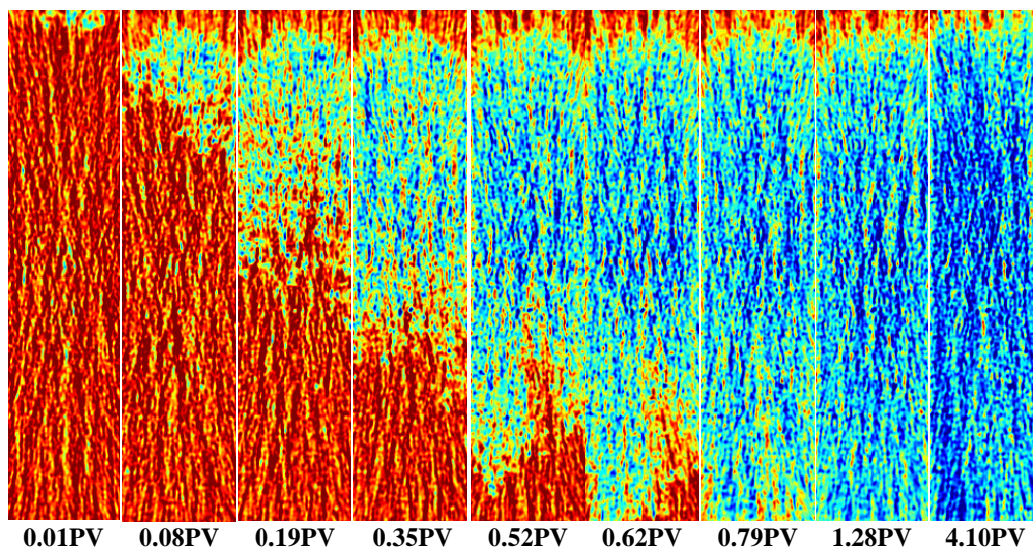


Fig. 2.6: CT images obtained during foam flooding in a core containing water-flooded residual oil (Simjoo & Zitha, 2013). The red colour stands for the water-flooded core including residual oil saturation, and the blue colour indicates the presence of the foam phase. Foam was injected from top to bottom to ensure gravity stable conditions. Foam breakthrough occurred at 0.63 ± 0.02 PV.

2.6 Conclusions

The study presented in this chapter demonstrated an integrated approach for the numerical simulation of foam transport in porous media with and without the oleic phase. First, the LE-IT foam model was matched to the foam core-flood experiments in the absence of the oleic phase

by taking into account the foam dry-out phenomena, rheological characteristics along with shear thinning properties and foam-quality regimes. The parameters of the water-saturation and the shear-rate dependent functions (F_2 and F_4) were determined by history-matching the foam quality-scan data at the steady-state condition in the low/high quality regimes. The corresponding parameters of F_2 and F_4 functions were then used to model the effect of the surfactant concentration on the pressure build-up induced by foam. The parameters of the surfactant-concentration dependent function (F_1) were obtained by matching the numerical and experimental pressure drop data for the transient and steady-state conditions.

The numerical simulation of foam flooding in the presence of water-flooding residual oil was performed by estimating the oil-saturation dependent function of the foam mobility interpolation factor. The numerically calculated pressure drop fitted well the experimental lab data of the transient and steady-state foam generation and propagation in the presence of oil. Two distinct regimes of incremental oil production were captured by the numerical simulation, first by the formation of an oil bank and, then, followed by a long tail production. The results of this study showed that the developed numerical model reproduced the main feature of the transient and steady-state foam flow regimes in the presence of the oleic phase. This was supported by a good match between pressure and oil recovery profiles obtained numerically with those obtained from the foam flooding EOR experiment in the Bentheimer sandstone core samples.

Chapter 3

Mechanistic Modelling of Alkali/Surfactant/Polymer Flooding Process at Under-Optimum Salinity Condition for EOR

3.1 Abstract

Alkaline-Surfactant-Polymer (ASP) flooding is potentially the most efficient chemical EOR method. It yields extremely high incremental recovery factors, in excess of 95% of the residual oil for water flooding, under controlled laboratory conditions. However, current opinion is that such extremely high recoveries can only be achieved at optimum salinity conditions, i.e. for the Winsor Type III micro-emulsion phase, characterized by an ultralow interfacial tension (IFT). This represents a serious limitation since various factors, such as alkali-rock interaction, the initial state of the reservoir water and the salinity of injected water, may shift the ASP flooding design to either under or over-optimum conditions. A recent experimental study of ASP flooding by Battistutta et al. (2015), based on a single internal olefin sulfonate (IOS) in natural sandstone cores with varying salinity from under-optimum to optimum conditions, indicated that high recovery factors can also be obtained in under-

The content described in this chapter is published in: Hosseini-Nasab et al. "Mechanist Modelling of Alkaline/Surfactant/Polymer Flooding Process at Sub-Optimum Salinity Condition for Enhanced Oil Recovery", *Journal of Industrial & Engineering Chemistry Research*, 2016, 55, pp 6875–6888.

optimum salinity conditions.

In this chapter, a mechanistic model was developed to explore the causes behind the observed phenomena. The numerical simulations were carried out using the UTCHEM research reservoir simulator, together with the geochemical module EQBATCH. UTCHEM combines multiphase, multicomponent simulation with robust phase behaviour modelling. An excellent match of the numerical simulations with the experiments was obtained for oil cut, pressure drop, cumulative oil recovery, pH profile, surfactant, and carbonate concentration in the effluents. The simulations gave additional insight into the propagation of alkali consumption, salinity and surfactant profiles within the core. The study showed that the initial condition of the core is important in designing an ASP flooding. Because of uncertainties in the various chemical reactions taking place in the formation, an accurate geochemical model is essential for operating an ASP flooding in a particular salinity region. The simulation results also demonstrate that, for crude oil with a very low total acid number (TAN), ultralow IFT and low surfactant adsorption can be achieved over a wide range of salinities that are less than optimal. The results provide a basis to perform improved modelling of the under-optimum salinity series of experiments and thus optimizing the design of ASP flooding methods for the field scale with more-complicated geochemical conditions.

3.2 Introduction

Early research showed that, to recover water-flooded residual oil, it is vital to increase the capillary number as the capillary forces have the main responsibility for oil entrapment after water flooding during immiscible displacement inside porous media (Lake et al., 2014). Capillary numbers are dimensionless values defined by the ratio of viscous and capillary forces. ASP flooding is an emerging technology to increase production from oil reservoirs and is potentially the most efficient chemically-Enhanced Oil Recovery (cEOR) technique (Sheng, 2014). In this method, a combination of alkali, surfactants and polymer is used to mobilize capillary-trapped oil and to improve volumetric sweep efficiency. The surfactant reduces the IFT between the displacing phase and crude oil to an ultralow value ($< 10^{-3}$ mN/m). Alkalis induce the formation of soaps by interaction with a crude oil that exhibits a high Total Acid

Number (TAN), and as well reduce surfactant adsorption on the rock by increasing the pH of the injection solution. The generated *in-situ* soap in combination with surfactants allows ultralow IFTs to be reached, which results in the mobilization of considerable quantities of the trapped oil (Sheng, 2011). Polymers increase the viscosity of the drive water in order to give stable displacement of crude oil and to considerably improve the volumetric sweep efficiency of the reservoirs.

As global oil prices increased from the early 2000s, research into polymer and ASP flooding resulted in a number of successful field applications. Incremental oil recoveries of 20%, 24.0%, and 26.8% were reported for the Daqing oil field (Demin et al., 1999; Sheng, 2014), the Karamay oil field (Qi et al., 2000) and the Tanner field (Pitts et al., 2006). ASP flooding provides a distinctly higher recovery factor than polymer flooding on the reservoir scale (5%-10%). Every oil field typically requires its own combination of chemicals in order to maximize oil recovery. Several authors have investigated ASP flooding, focusing on the composition of surfactants or the design of ASP slugs (Levitt et al., 2011; Ogolo et al., 2012; Young, 2011). Their work relied on core-flood experiments to determine the optimum parameters for achieving a maximum oil recovery. A generally successful laboratory approach to chemical EOR has shown that, when ASP chemical formulation (i.e., surfactants, co-solvent, alkali, polymer, and electrolytes) in contact with crude oil creates the micro-emulsion at optimum salinity, ASP flooding results in significantly high (> 95%) recovery of water-flooded residual oil from the sample reservoir cores. Characterization of oil/water/surfactant phase behaviour has been described by Winsor (Winsor, 1954). He indicated that the phases change from Type II- (oil in the excess water phase), Type II+ (water in the excess oil phase), and Type III (the bi-continuous oil/water phase) as the salinity increases. Based on the salinity limits, Type II- (or under-optimum) is below the lower salinity limit of Type III and Type II+ (or over-optimum) is above the upper salinity limit of Type III. Several studies indicate that ultralow IFTs are observed with Type III, which consists of excess oil and excess water phases separated by a micro-emulsion phase. The salinity concentration at which equal amounts of oil and water are solubilized in this (middle phase) micro-emulsion, is referred to as optimal salinity (Sheng, 2011). Conventionally it has been assumed that in order for ASP flooding to

achieve maximum oil recovery, chemicals must be injected at optimum salinity under Type III phase behavior conditions (Healy et al., 1976; Nelson, Lawson et al., 1984). However, several factors, including alkali-rock reactions, the initial salinity state of the reservoir water and the salinity of the injected water, may shift the ASP flooding design to either under or over-optimum conditions.

Several researchers have indicated that the different phenomena involved in the ASP flooding mechanism are not that simply correlated. They have found that (equilibrium) IFT is not the dominant factor controlling oil recovery, but instead other factors, such as the mobility ratio and surfactant retention, are crucial. Thus, the equilibrium IFT between the injected surfactant fluid and crude oil, as present in a phase behaviour experiment, could be a representation of the phases in contact within a particular porous medium, but this may not be true for all systems (Gerbacia & McMillen, 1982). Recent studies have shown that high oil recovery is also possible under non-optimum salinity conditions (Alagic & Skauge, 2010; Levitt et al., 2011; Sheng, 2013). This was the case in the series of experiments conducted in which the highest oil recovery was observed in Type II-, i.e. under-optimum salinity conditions, in the work by Battistutta et al (2015). Thus, new studies have challenged the conventional wisdom about ASP EOR. Hence, the current strategy is based on the incorrect assumption that ASP flooding should only operate at the optimum salinity condition (i.e. Winsor type III). Each phase type has advantages and disadvantages associated with oil recovery, depending on the relative permeabilities and other parameters (see Table 3.1). Arhore (2012) has found experimentally that an under-optimum flooding recovered more oil than an optimum-salinity flooding (80% vs 68% of residual oil after a water-flood). At the time, it was thought that the *in-situ* salinity being slightly higher than the ASP salinity, was due to *in-situ* mixing with the initial and injected (water-flooding) brine.

Table 3.1: Advantages and disadvantages of three types of micro-emulsion systems for surfactant-based flooding EOR

Winsor phase types	Advantages	Disadvantages
Type II- (under-optimum)	low surfactant trapping and adsorption(Sheng, 2011), benefit of the low salinity flood	bypassing of remaining oil due to capillary diffusion and high mobility
Type III (optimum salinity range)	lowest interfacial tension (IFT), emulsification and high miscibility	formation of second liquid phase, coalescence and liquid crystal
Type II+ (over-optimum)	higher oil relative permeability than Type III, high miscibility of oil and ASP	surfactant entrapment in oil phase, oil-wet behaviour in relative permeability

Opposite salinity gradients are also applied to maximize oil recovery, i.e. injecting an ASP at higher salinity, i.e. Type II+, in combination with a low-salinity formation brine or polymer drive to move the system towards Type II- through Type III (Liyanage et al., 2012). The salinity requirement of a chemical flooding system usually varies during a process, because of various phenomena such as adsorption, dispersion and mixing of fluids. Thus, it is physically possible for two mechanisms (for instance, Type III and Type II-) to be operative for similar conditions in the ASP EOR process. This could result in losing the optimal salinity during the floods, but oil recovery might not decline when other mechanisms, such as low surfactant adsorption on the rock and less surfactant trapping in the oil phase in under-optimum salinity conditions, are functioning.

Lastly, several researchers reported the use of Low Salinity Surfactant (LSS) flooding as an EOR technique (Alagic & Skauge, 2010; Johannessen & Spildo, 2013; Spildo et al., 2012). The addition of a surfactant to a low salinity brine resulted in additional oil recovery in core-flooding experiments, even though IFT was not ultralow ($< 10^{-2}$ mN/m). The amount of additional oil recovered with this system was comparable to the amount of oil recovered when the salinity of the system is increased to the optimal salinity (and ultralow IFT), but surfactant retention was much lower, possibly due to better solubility of the Internal Olefin Sulphonate (IOS) surfactant at lower salt concentrations. The implication is a possibility for potentially better and more successful surfactant flooding in the Type II- region if a significantly lower retention outweighs the disadvantage of interfacial tensions being higher (Spildo et al., 2012). However, LSS flooding suffers from the limitation that it requires a significant salinity

reduction in the available water in most cases.

A series of ASP core-flooding experiments, performed at different salinities in the Type II- (under-optimum) vs. Type III (optimum salinity) phase behaviours, have been presented in a companion study (Battistutta et al., 2015). The aim of this experimental program was to determine the dependence of oil recovery and surfactant retention on salinity and IFT variations. This core-flood study reported higher recovery factors during under-optimum conditions (2.5 wt% NaCl) than in optimum conditions. Therefore, the question arises as to how this under-optimum condition will affect the incremental oil recovery factor. To further understand this outcome, this study aimed to investigate the salinity condition by developing a numerical model in a chemical flooding simulator.

The optimization, interpretation, and integrated design of this EOR method are essential when considering the complex phase behaviour and the complexity of physics and crucial parameters involved in the ASP EOR process. This requires a predictive model with appropriate physics to fully capture the underlying mechanisms driving the ASP EOR performance. The objective in this chapter is the modelling of a laboratory ASP core-flood experiment performed at under-optimum salinity to get a better understanding of the process for these under-optimum salinity conditions and its effectiveness over other optimum salinity techniques. The reason for this choice is that, in spite of the fact that ASP flooding had the lowest salinity, it produced the highest incremental oil recovery. The UTCHEM simulator, as the most practical tool for the mechanistic simulation of ASP flooding, is a research three-dimensional (3D) chemical flooding reservoir simulator for multiphase and multicomponent systems (Sheng, 2013). This simulator was used to interpret the ASP core-flood experiments in under-optimum salinity conditions by the simulation of various parameters. In this study the ASP flooding process was modelled by including the surfactant phase behaviour as a function of salinity, temperature and co-solvent concentration, fluid rheology, oil desaturation, rock fluid interaction (such as cation exchange), and geochemical reactions. To take into account the effect of geochemical reactions occurring in the core, EQBATCH, the built-in geochemical module of UTCHEM, was used to calculate the initial equilibrium ionic compositions, the CEC (cation exchange capacity) and HEC (hydrogen exchange capacity) (UTCHEM technical

documentation, 2011). EQBATCH takes into account the geochemical reactions existing in the ASP flooding, such as alkali precipitation with divalent cation, *in-situ* soap generation, and alkaline consumption by ion exchange reactions. The numerical simulation also attempted to uncover the sensitivities of oil recovery to the amount of injected surfactant, effective salinity profiles in the core and the uncertainties in developing a reliable model.

3.3 Experiment Materials and Methods

The alkali used in this study was sodium carbonate (Na₂CO₃, Merck, 99% pure); the co-solvent is a sec-butyl alcohol (SBA, Merck, 99% pure); the polymer is Hydrolysed Polyacrylamide, (Flopaam™ 3330S), and the surfactant is a C20-24 internal olefin sulphonate, ENORDET™ O242 (Barnes, 2010). The salt used for the brine preparation consists of sodium chloride (NaCl, >99% pure). The crude oil had the following properties (at 52 °C): density 0.856 g/cm³, viscosity 3.4 ± 0.7 cP, TAN 0.05 mg KOH/g oil. The Bentheimer core was used to perform the experiments. Their mineralogy and physical properties were measured and are described in Table 3.2.

Table 3.2: Physical properties and mineralogical composition of Bentheimer sandstone core

Mineralogy				Physical Properties				
Quartz	Clay	Feldspar	Carbonate Minerals	Porosity	Permeability	Diameter	Length	Pore Volume
weight %	weight %	weight %	weight %	%	Darcy	cm	cm	cm ³
94.40	2.70	2.4±0.1	0.5±0.1	25±0.1	3.50±0.2	3.8±0.1	38.35±	93±0.2

The setup used for the core-flood experiments is shown in Fig. 3.1. The core holder was placed vertically in an oven operated at 52 ± 1° C. A back pressure regulator and collector of produced fluids was located at the end. Differential pressure transducers were placed near the inlet of the ISCO pump, near the inlet of the piston pump line, and just before the core holder to measure the pressure drop over the core for different injection profiles. The core used was cut from Bernheimer-type sandstone and examined in a CT scan to detect the presence of any anomalies, such as cracks or uncharted elements, as shown in Fig. 3.2. The core-flood

procedure is shown in Table 3.3. The core was flushed with CO_2 at the start of the experiments in order to remove the air and ensure that a 100% brine saturation was reached. More information about all the series of ASP core-flood experiments in under-optimum and optimum salinity conditions in the Bentheimer and Berea sandstone rocks can be found elsewhere (Battistutta et al., 2015).

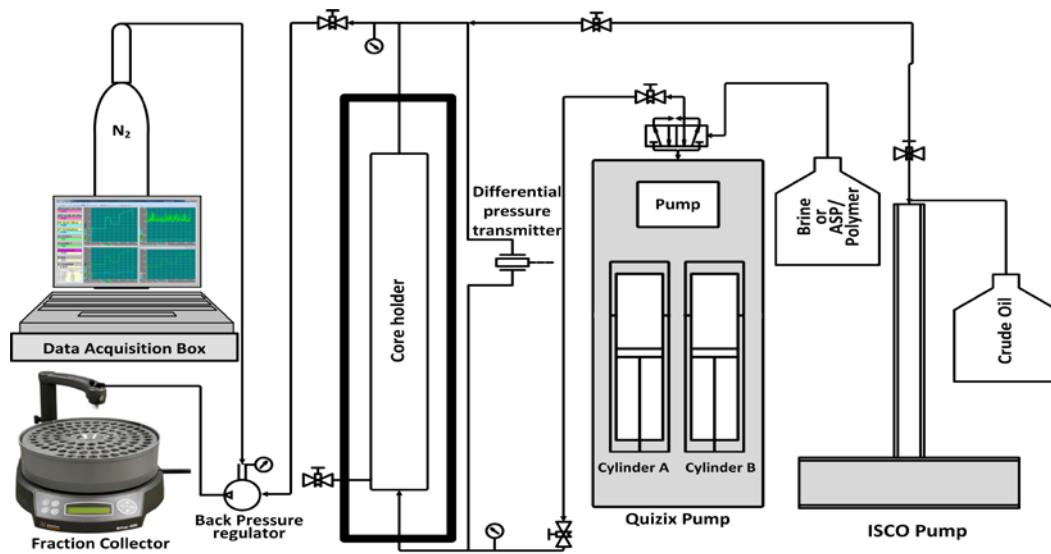


Fig. 3.1: Schematic of the experimental setup used to perform ASP core-flood experiments.

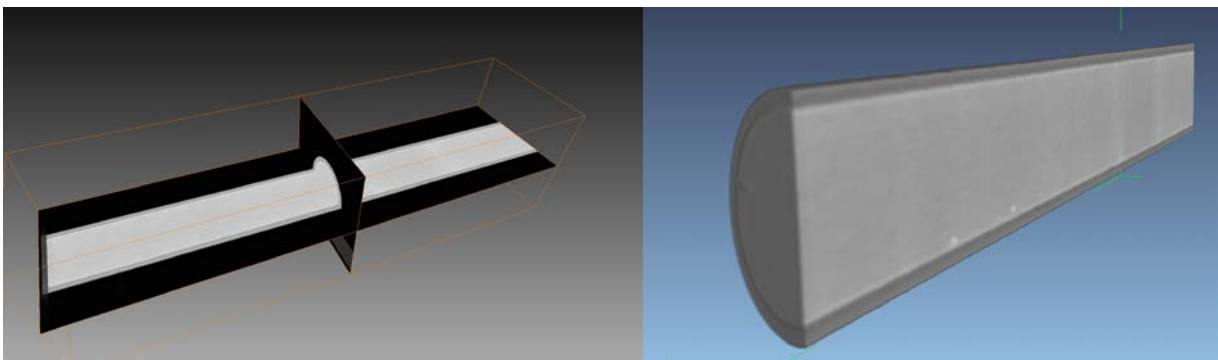


Fig. 3.2: Three-dimensional (3D) image from the cross section of core obtained by the medical computed tomography (CT) scan apparatus.

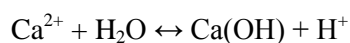
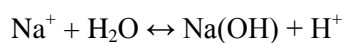
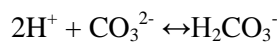
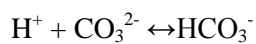
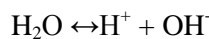
Table 3.3: Summary of injection profile and basic properties for ASP core-flood experiments

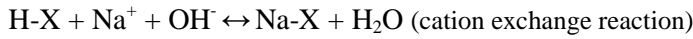
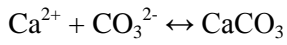
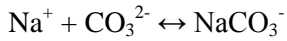
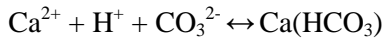
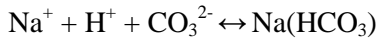
Injection Step	Pore volume (PV)	Flow-rate (cm ³ /min)	Back-pressure (Bar)	Temperature (°C)	Injection direction
CO ₂ flushing	-	-	0	21	Bottom to top
Brine saturation	10	1	25	52	Bottom to top
Permeability test	-	1-5	5	52	Bottom to top
Oil injection	2.5	1	5	52	Top to bottom
Water flooding	7	0.25	5	52	Bottom to top
ASP injection	0.48	0.25	5	52	Bottom to top
Polymer injection	2.58	0.25	5	52	Bottom to top

3.4 Results and Discussion

3.4.1 Geochemical Model

EQBATCH, the geochemical module of UTCHEM was used to describe the effect of geochemical reactions that occur during ASP flooding. The mineralogical composition of the rock used in core-flood experiments, was considered to develop the geochemical model. Dissolution–precipitation reactions, homogeneous aqueous reactions, soap generation, and ion exchange reactions with rock minerals and micelles are the key features of the ASP flooding geochemical interaction for numerical simulation of the process. However, in this study, the precipitation of divalent cations was ignored because of their low concentrations. The dissolution of quartz was negligible since at the low pH observed in the experiments, quartz dissolution is rather slow. *In-situ* soap generation of soap was also ignored due to the low acid number of the crude oil (<0.05 TAN). Thus, the model includes ion exchange reactions and the aqueous reactions with alkali. One of the main reactions between rock and the ASP flooding concerned cation exchange between sodium and hydrogen. This was the major cause of the consumption of alkali, and it had the ability to shift the pH front (Delshad et al., 2013). Key ion exchange reactions include the exchange of hydrogen and sodium, which is a main reaction for alkali loss during the process. The main reactions considered in the model are given below.





The exchange capacity of the rock was estimated by comparing the laboratory result with the pH profile and was found to be 0.047 ± 0.002 mequiv/mL. The cation exchange capacity determines the amount of positively charged ions that are absorbed into the rock. The initial pH in the system before the chemical breakthrough was calculated, based on the presence of concentrations in the aqueous phase, especially that of H^+ in the geochemical model.

3.4.2 Surfactant Phase Behaviour Simulation

Experimental surfactant phase behavior data, which are volumetric components of three pseudo-phases (aqueous, oleic, and micro-emulsion), were modeled. Oil and water surfactant solubilization ratio data could be fitted with model parameters specifying tielines (distribution curves) and binodal curve heights of the ternaries. The solubilization ratio in the surfactant phase behaviour experiment is the relation of concentration of oil and water compared with the concentration of the surfactant, described in the relation,

$$R_{l3} = \frac{C_{l3}}{C_{33}} \quad \text{for } l = 1,2 \quad (3-1)$$

where R_{l3} is the solubilization ratio, C_{l3} is the concentration of phase l solubilized in micro-emulsion, and C_{33} is the concentration of surfactant solubilized in micro-emulsion.

In order to investigate the phase behaviour under static (no flow) conditions, a simulation was conducted in batch mode using the sample values for the reservoir, as given in Table 3.4. A core plug with porosity 1.0 and a very high value permeability were chosen to replicate the use of a test tube when the tests were conducted in the laboratory. The phase behaviour tests conducted in the laboratory show that the optimum salinity is 4 wt% TDS (2 wt% NaCl and 2 wt% Na_2CO_3). To determine the phase behaviour model parameters from the laboratory phase behaviour study, the heights of the binodal curve and the lower and upper effective salinity are

used as input parameters in UTCHEM to solve Hand’s model (Delshad et al., 2013). The lower (C_{sel}) and upper (C_{seu}) limits of effective salinity are the effective salinity in which three phases form or disappear. Since the water-oil ratio (WOR) was equal to 1, the phase behaviour simulation was carried out using 50/50 (vol%) water and oil concentrations. Thus, the initial water saturation was 0.50. The viscosity of oil and water was kept as 1.0 cP.

Table 3.4: Representative reservoir properties and values of modelling parameters for surfactant phase behaviour simulation based on laboratory measurements

Simulation Parameters	Values
Simulation Time (Days)	250
Permeability (mD)	1000000
Porosity	1
Optimum Salinity	25000 ppm NaCl
Height of binodal curve at zero salinity (HBNC70)	0.040
Height of binodal curve at optimal salinity (HBNC71)	0.037
Height of binodal curve at twice optimal salinity (HBNC72)	0.040
Lower effective salinity (CSEL7)	0.466 mequiv/mL
Upper effective salinity (CSEU7)	0.586 mequiv/mL
Oil concentration at the left plait point, volume fraction (C_{2PL})	0
Oil concentration at the right plait point volume fraction (C_{2PR})	1

To model the phase behaviour as the batch mode, it was considered that many pore volumes of water, oil, surfactant, co-solvent and polymer, whose compositions and concentrations were the same as those used in the tube tests, were injected. This resulted in the flow becoming a steady state. In the simulation, the salinity range of Type III was required to be extended in order to match the high solubilization ratio of Type II- (Levitt et al., 2011; Veedu et al., 2010). Fig. 3.3 shows the comparison of the laboratory phase behaviour results and the numerical simulation match for the effect of the surfactant on the optimal salinity and solubilization ratio.

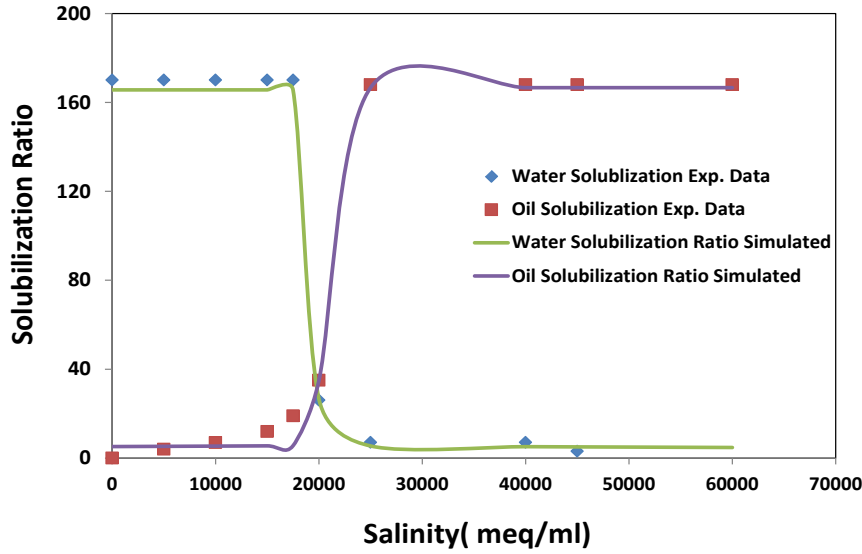


Fig. 3.3: Simulated and measured solubilization ratio of oil and water versus salinity for surfactant phase behaviour tests.

3.4.3 Bulk Polymer and Surfactant Simulation

Before developing the model for ASP flooding, in order to attain the required viscosity for the ASP and polymer drive solutions, it was necessary to obtain the related viscosity parameters of the model. Although the polymer viscosity was obtained from laboratory tests, a simulator does not have the ability to directly input these values, therefore, it calculates them numerically according to the Flory-Huggins equation. The dependency of the polymer solution viscosity at a zero-shear rate on the polymer concentration and on salinity was obtained in this work as shown by the relation below:

$$\mu_p^0 = \mu_w \left[1 + (A_{p1}C_{4l} + A_{p2}C_{4l}^2 + A_{p3}C_{4l}^3)C_{SEP}^{S_p} \right] \quad (3-2)$$

where μ_w is the viscosity of water, C_{4l} is the concentration of polymer in water, μ_p^0 the polymer viscosity at a zero-shear rate, and $C_{SEP}^{S_p}$ the effective salinity (with S_p an input parameter to determine polymer viscosity as a function of salinity). S_p is the slope of the $(\mu_p - \mu_w)/\mu_w$ vs C_{SEP} on the log-log plot. A_{p1} , A_{p2} , and A_{p3} are the three polymer viscosity parameters that are unknown. The factor $C_{SEP}^{S_p}$ accounts for the dependence of polymer viscosity on salinity and hardness. The effective salinity (C_{sep}) combines the effects of monovalents and divalents for polymer, as calculated by

$$C_{SEP} = \frac{C_{51} + (\beta_p - 1)C_{61}}{C_{11}} \quad (3-3)$$

where C_{51} , C_{61} , and C_{11} are the anion, divalent, and water concentrations in the aqueous phase, and β_p , whose typical value is ~ 10 , is measured in the laboratory as an input parameter for simulation. First, the input parameter Sp is determined to be 0.151; thus, for different values of A_{p1} , A_{p2} , and A_{p3} , the calculated polymer viscosity from the numerical simulation was matched with the laboratory data. Polymer adsorption and surfactant adsorption are modeled by a Langmuir-type isotherm, and are a function of concentration of polymer or surfactant, salinity, and permeability. Both adsorptions are modeled as irreversible, with respect to both concentration and effective salinity. The adsorbed concentration of polymer and surfactant are given by

$$\hat{C}_i = \frac{a_i(C_i)}{1 + b_i C_i}, \quad a_i = (a_{i1} + a_{i2} C_{SEP}) \left(\frac{k_{ref}}{k} \right)^{0.5} \quad (3-4)$$

\hat{C}_i is the Langmuir isotherm for surfactant or polymer, i represents either the surfactant or polymer component. The adsorption model parameters a_{i1} , a_{i2} and b_i are found by matching laboratory data of polymer and surfactant adsorption data, as given in Table 3.6. The reference permeability (k_{ref}) is the permeability at which the input adsorption parameters are specified.

3.4.4 ASP Flooding Model

a) Bulk simulation model and parameters. A simulation model for ASP flooding, respecting the geometry, rock/fluid properties, geochemical reaction, and surfactant phase behaviour conditions, was employed to mimic the bulk experiments. Each simulation of the ASP flooding started with the integration of the geochemical model, phase behaviour model, and bulk polymer parameters into UTCHEM. ASP flooding was conducted in a previously water-flooded Bentheimer core with a high initial oil saturation of $S_{oi} = 0.43$. The ASP flooding consisted of: (1) an ASP slug of 0.48 PV and (2) a polymer drive of 2.58 PV. The ASP slug contained 0.6 wt% surfactant, 1.0 wt% co-solvent, and 1450 ppm polymer in under-

optimum salinity conditions including 2 wt% Na_2CO_3 , and 0.5 wt% NaCl . The total salinity of the ASP slug was 1.98 ± 0.01 wt% NaCl , so that the chemical was at under-optimum salinity conditions. The ASP slug was then pushed with the same type of polymer dissolved in brine of 1.98 wt% NaCl . Fig. 3.4 shows the viscosity of the ASP slug and polymer drive versus the shear rate for the polymer concentration of 1450 ppm at salinity of 1.98 wt% NaCl at two different temperatures. The ASP core-flood was conducted at an interstitial velocity of 4.22 ft/day which corresponds to a shear rate of 22.45 s^{-1} , and polymer viscosity was 5.1 ± 0.4 cP at this shear rate. Table 3.5 and Table 3.6 summarize the rock/fluid properties and conditions of the experiment that were implemented in the ASP flooding simulation.

Table 3.5: Input parameters of rock and fluid properties for numerical simulation

Brine permeability	3.51(Darcy)
Porosity	0.25
Core weight	755.15 (g)
Pore volume	93 (cm^3)
Temperature	52 ($^{\circ}\text{C}$)
Brine viscosity at core condition	0.54 (cP)
Brine density at core condition	0.987 (g/cm^3)
Oil viscosity at core condition	3.7 ± 0.07 (cP)
Oil density at core condition	0.855 (g/cm^3)
Total acid number (TAN)	<0.05 (mg KOH/g oil)

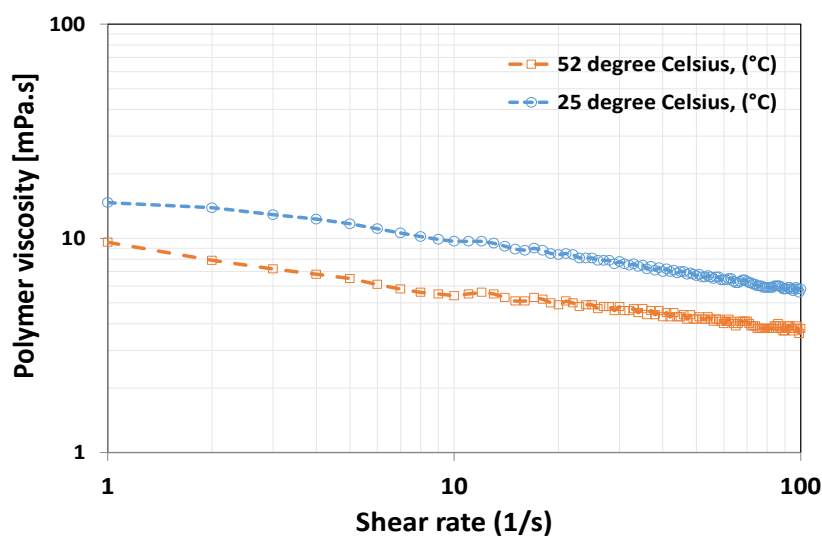


Fig. 3.4: Viscosity of polymer of ASP slug and polymer drive for the 1450 ppm polymer concentration at salinity of 1.98 wt% NaCl , for two different temperatures.

Table 3.6 Simulation parameters and physical properties from the ASP flooding experiment for simulation input

Parameters	Value
Number of grid blocks	1×1×100
Core grid block size (m×m×m)	0.032× 0.032 ×0.0048
Initial oil saturation	0.812
Residual (irreducible) water saturation	0.17
Remaining oil saturation (water flooding)	0.43
Residual oil saturation (chemical flooding)	0.147
Total dissolved salinity (water flooding)	1.98 wt% (NaCl)
Producer bottom hole pressure	5 bar
Polymer viscosity parameter $A_{p1}, A_{p2}, A_{p3}, S_p$	50, 100, 200, 0.151
Polymer adsorption parameter a_{41}, a_{42}, b_4	4.3, 0.6, 100
Surfactant adsorption parameter a_{31}, a_{32}, b_3	3.2, 0.55, 1000
ASP slug properties	
Slug size	0.48 (PV)
Injection flow rate	0.25 (cm ³ /min)
Surfactant concentration	0.6 wt%
Co-solvent concentration	1.0 wt%
Polymer concentration	1450 ppm
Salinity	0.5 wt% (NaCl)
Alkali concentration	2.0 wt%
Polymer drive properties	
Polymer concentration	1450 ppm
Drive size	2.58 PV
Injection flow rate	0.25 cm ³ /min
Salinity	1.98 wt% (NaCl)

For the history matching of the pressure drop and oil recovery, the relative permeability of the water/oleic phase and their ratio in under-optimum conditions for an ASP flooding at a high capillary number are illustrated, in Fig. 3.5 and Fig. 3.6 respectively, against the relative permeability of the ASP flooding at optimum salinity at a high capillary number, and relative permeability of water flooding. Corey-type equations were used to model the relative permeabilities. The assumptions are that, (i) an ASP flooding for optimal salinity with ultralow IFT reaches miscible conditions, (ii) the end point of relative permeabilities are unity, and (iii) the residual saturations are zero at high capillary numbers in the formulation. The relative permeability in under-optimum salinity conditions is the interpolation between the water

flooding and the miscible relative permeabilities. IFT between the aqueous and oleic phases in under-optimum conditions is much less than water flooding and is relatively higher than optimum salinity conditions of an ASP flooding. By reducing water/oil IFT, the capillary number is increased, which leads to a lowering of the residual saturation, resulting in a change of the relative permeabilities.

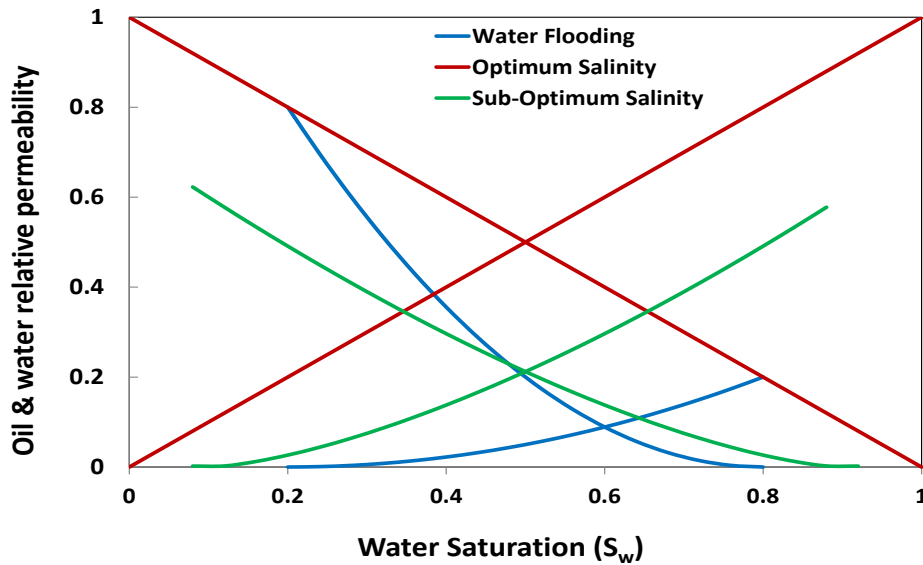


Fig. 3.5: Relative permeability of the water and oil phases for ASP flooding in under-optimum conditions, in comparison to relative permeabilities of water flooding and optimum salinity (Type III) ASP flooding.

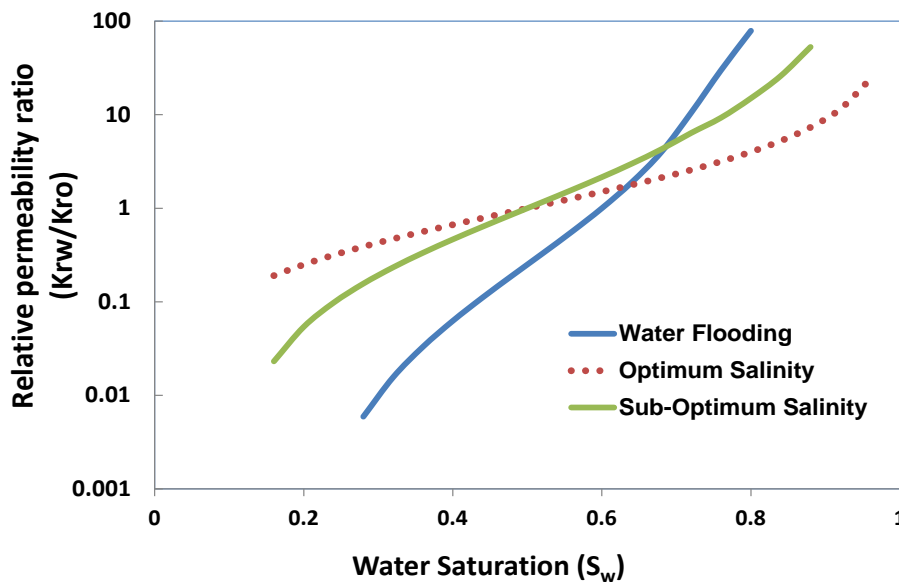


Fig. 3.6: Oil and water relative permeability ratio for under-optimum (Type II-) ASP flooding against water flooding and optimum condition (Type III) of ASP flooding

Fig. 3.5 shows that the relative permeabilities have a tendency to increase and to become more linear as the IFT decreases or the capillary number increases. Fig. 3.6 demonstrates the k_r ratio of a Type II- system (ME/O) with the k_r ratio of the corresponding water/oil system (W/O) and an ASP flooding of Type III. In the Type II- system, the ratio is the k_r of the water-continuous (oil in water) micro-emulsion phase to the k_r of the excess oil phase. Fig. 3.6 shows that, at a higher saturation, the k_{rw}/k_{ro} ratio becomes lower in the Type II- system than in water-flooding. This, according to the fractional flow equation, leads to the water-cut becoming lower, thus increasing the displacement efficiency. Table 3.7 summarizes the relative permeability and trapping parameters used in the simulation. Fig. 3.7 shows the relationship between residual oil, connate water saturations and trapping number, referring to them as Capillary Desaturation Curves (CDCs). The dependence of residual saturations is modeled in UTCHEM as a function of the trapping number, which is a formulation to model the combined effect of viscous and buoyancy forces compared to capillary forces (Mohammadi et al., 2009).

Table 3.7: Relative permeability and capillary desaturation parameters

Simulation Parameters	at low TrappingNo.	at high Trapping No.
Residual water saturation	0.17	0.05
Residual oil saturation	0.42	0.07
Water end point relative permeability	0.2	0.58
Oil end point relative permeability	0.8	0.62
Water exponent relative permeability	2	1.5
Oil exponent relative permeability	2.5	1.5
Water trapping parameter	1865	
Oil trapping parameter	59074	

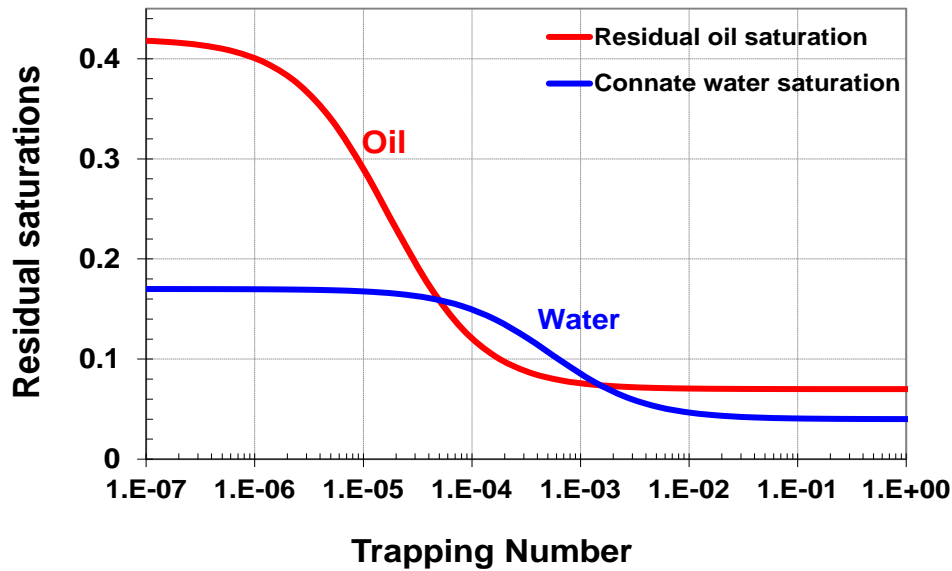


Fig. 3.7: Residual oil saturation (S_{or}) and connate water saturation (S_{wc}), as a function of trapping number at high and low capillary numbers. Capillary desaturation curves (CDCs) used in the simulations are shown.

b) Pressure drops and recovery factors. Once the concentrations and the parameters were implemented in the model, the simulated pressure drop and oil-cut results obtained from numerical simulation were compared with their corresponding laboratory results. Fig. 3.8 shows a good agreement between the simulated and the measured pressure drops. The pressure drop increased during the ASP injection and decreased to a plateau value during the polymer drive. Small fluctuations in the pressure drop after the start of the polymer injection and before the chemical breakthrough were observed.

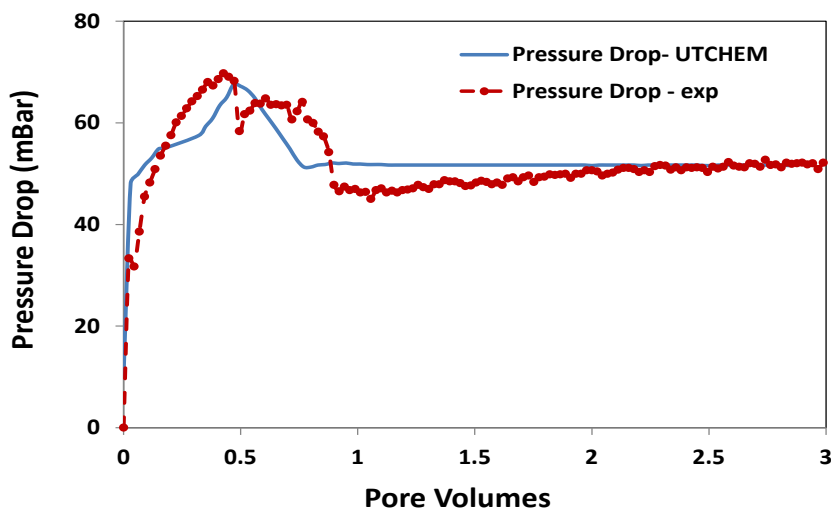


Fig. 3.8: Comparison of the pressure drop between the simulation results and the laboratory data. Injection of 0.48 PV ASP slug, followed by 2.58 PV of polymer injection as drive. Breakthrough of the chemical occurred at 0.8 PV.

Fig. 3.9 shows an excellent match of the simulated effluent oil-cut with the corresponding measured values, except for the fact that in the simulations oil production starts later than in the physical experiments. This can be attributed to the formation of a thick oil bank in the simulation when ASP flooding ends, rather than a gradual increase in production as seen in the laboratory data. The increase in oil production with the amount of polymer injected could also be due to an increase in the viscosity of the displacement fluids, for instance, the increase in the concentration of micro-emulsions.

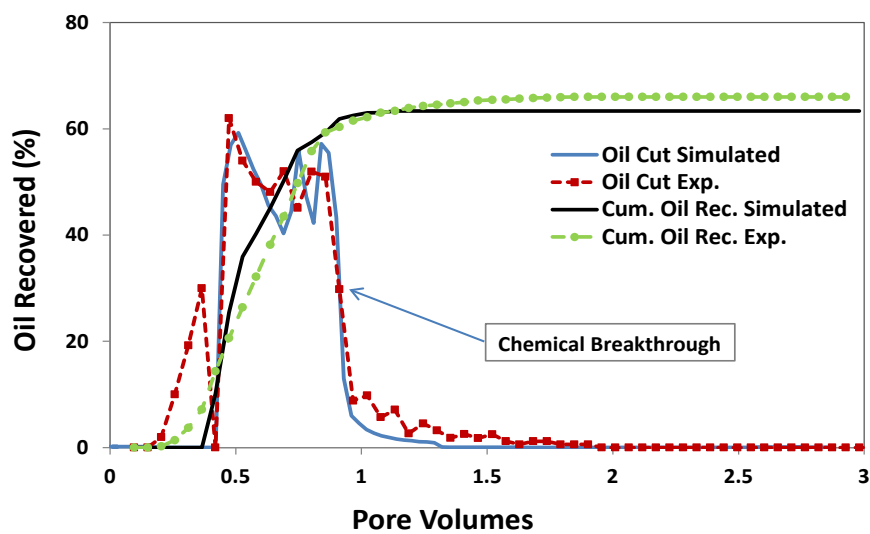


Fig. 3.9: Recovery history obtained from simulation and experimental data for oil cut production and cumulative oil. Chemical breakthrough occurred at 0.8 PV.

Fig. 3.9 shows that the cumulative oil production profiles between the simulation and measured data do not start at the same Pore Volumes (PV). Due to the sharp edge of the oil bank, there is a steep rise in the cumulative oil profile. The fluctuation in oil recovery in the oil bank shows an unsteady cumulative oil production. The breakthrough of the chemical occurs at 0.8 PV when oil production diminishes rapidly, which coincides with the decrease in the pressure drop. After the chemical breakthrough, oil production continues as a tail-end production of oil-in-water micro-emulsions. The oil recovered from the simulation started at a later 0.35 PV and less oil was produced after the chemical breakthrough, thus this was nearly 2% less than the recovery achieved in the laboratory. If we remove the first bump of oil production, a much better match between simulations and experiments is obtained.

Nevertheless, we cannot be sure about the cause of the first oil bump. The flow rate used for chemical injection is lower than that used for water flooding. Therefore, even though the chemical is roughly 10 times more viscous than water, the capillary number does not increase sufficiently to mobilize oil.

c) Analysis and simulation of effluents. Normalized concentrations, defined as a ratio of the chemical detected at the effluents divided by its initial concentration, were used for the simulation of the effluent chemical compositions. Fig. 3.10 shows the modelled and measured carbonate concentration, surfactant concentration, and pH in the effluents. The surfactant production started at 0.8 PV, coinciding with the appearance of the pH in the effluent at the occurrence of the chemical breakthrough. Fig. 3.10 shows that the amount of produced carbonate obtained from the simulations was smaller than the corresponding measured data. This suggests that in the simulations, carbonate is retained in the reservoir rock. Moreover, ion exchange with clays in the rock caused a delay in the chemical breakthrough of carbonate, similar to the effect of adsorption.

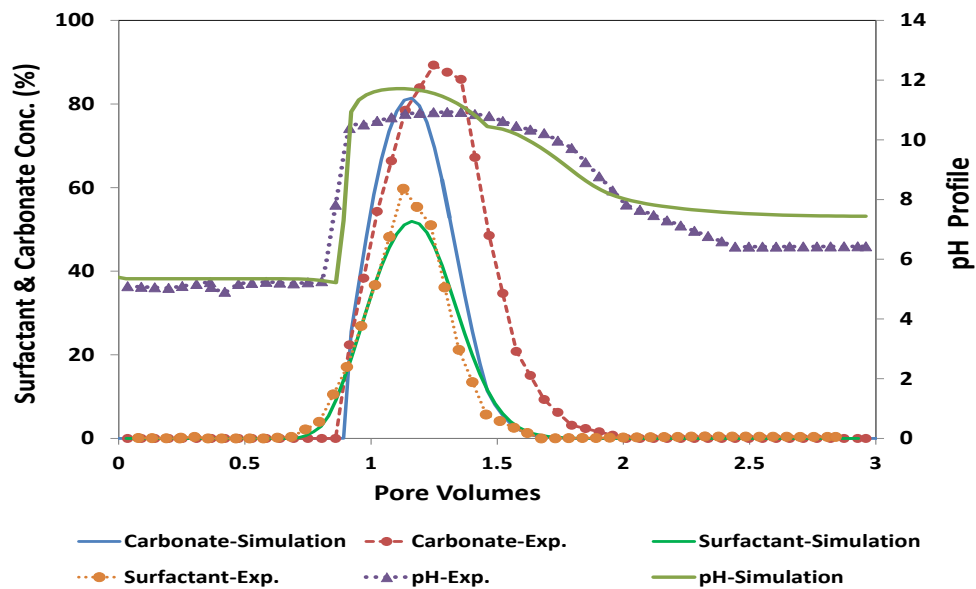


Fig. 3.10: Comparison of calculated carbonate, surfactant concentration and pH profiles at effluents with laboratory data.

At 1.6 PV, the carbonate concentration decreased to zero, causing the pH profile in Fig. 3.10 to decrease much faster rate than the experimental result. This could be attributed to the geochemical model, which influences the high carbonate consumption in the rock, because

of the presence of divalent calcium (Ca^{+2}) cations. Prior to the alkali breakthrough, no chemical appears at the effluents, thus carbonate and surfactant concentration were recorded as zero and the pH kept its initial value. After the alkali breakthrough, the carbonate concentration as well as the pH increased and, when no more alkali or surfactant appeared in the effluent, the oil production ceased and the pressure drop stabilized.

Initially, the core was saturated with brine that did not contain any alkali; therefore, the rock/brine interactions (i.e. H^+ cation exchange) are responsible for the initial pH values (pH~5.4). However, at the end of the process, the pH profile did not reach the initial values, which could be due to alkali desorption after the ASP slug injection. Desorption might occur with a slow and constant rate during the polymer injection. Fig. 3.11 shows that the alkali (or pH), polymer, carbonate, and surfactant fronts move together after the chemical breakthrough (at 0.8 PV). Thus, the breakthrough of chemicals in the ASP slug occurred at the same time without fingering effects. The oil saturation reduces to a low value of ~5% after the chemical breakthrough, showing the efficiency of the ASP slug in recovering most of the water-flooding residual oil.

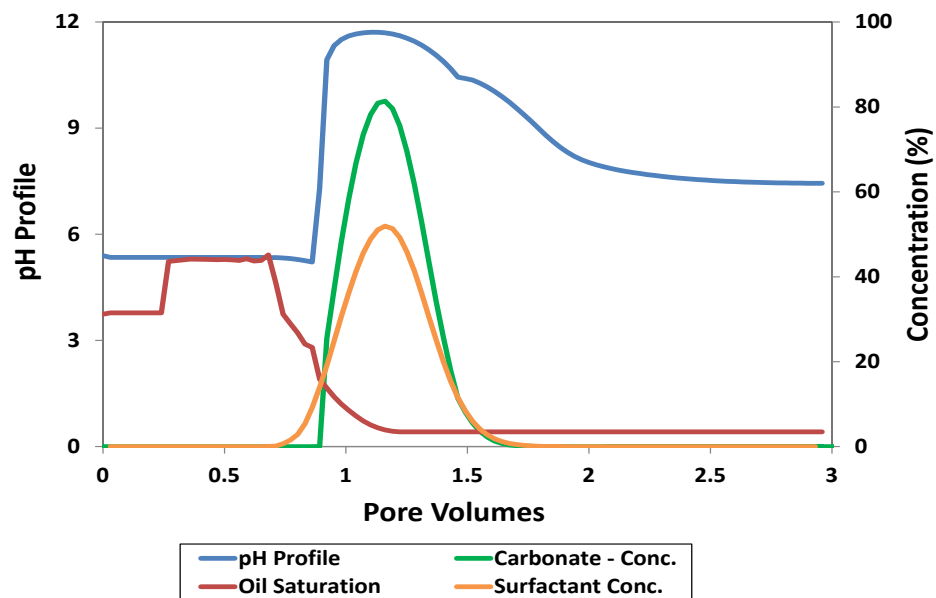


Fig. 3.11: Comparison of history plots of simulated pH, carbonate concentration, oil saturation and surfactant concentration comparable at effluents. Concentration normalized at a factor of 100%.

Fig. 3.12 shows that the effective salinity at the effluent was below the lower salinity limit of 0.466 mequiv/mL (2.5 wt% NaCl). However, the effective salinity of the ASP slug was influenced due to the geochemical reaction between the rock and the composition of the slug. As can be seen, the effective salinity of the ASP slug was increased and approached the lower salinity limit of optimum salinity. Consequently, low values of IFT were seen after the chemical breakthrough, when the effective salinity was close to optimal conditions.

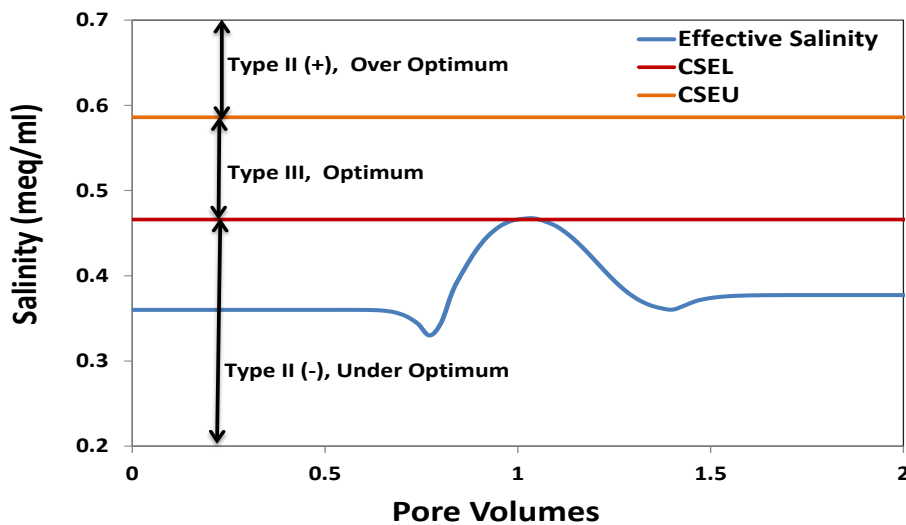


Fig. 3.12: Calculated effective salinity and surfactant concentration over pore volumes (PV) at effluent.

Fig. 3.13 displays the effective salinity profiles at 0.1 PV, 0.48 PV and 1 PV. At 0.1 PV, when just after the injection of the ASP slug, the effective salinity was near the lower salinity limit. Similarly, at 0.48 PV from the effective salinity profile, the ASP slug was seen to progress further. After the chemical breakthrough at 1 PV, the influence of salinity from the ASP slug and the polymer drive ensures that the effective salinity of the core remains below the lower salinity limit (i.e. under the Type II- or under-optimum conditions). To further understand the effective salinity profiles, IFTs were plotted during ASP flooding at 0.1 PV and 0.48 PV in Fig. 3.14. This figure shows that, as the ASP slug progresses, low IFTs were seen when the effective salinities were close to the lower salinity limit.

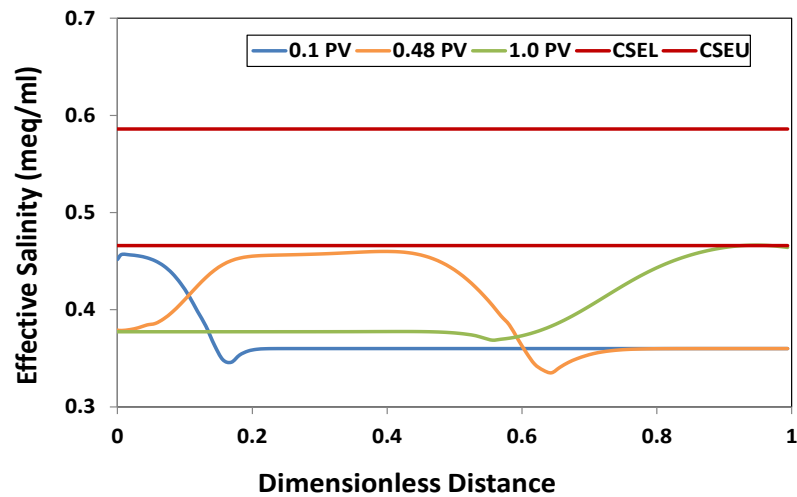


Fig. 3.13: Progression of effective salinities at 0.1 PV, 0.48 PV, and 1 PV along the core.

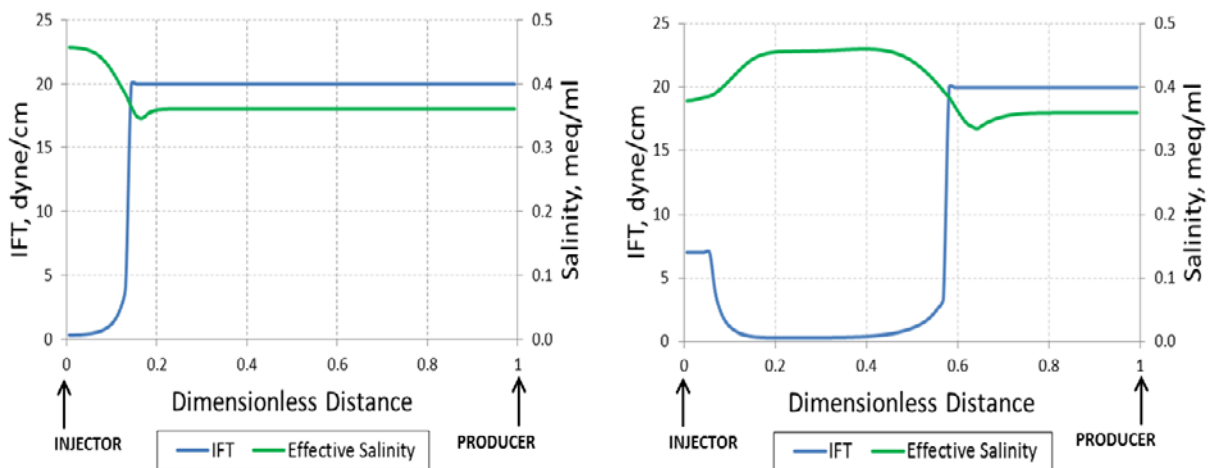


Fig. 3.14: Interfacial tension and effective salinity profiles at 0.1 PV (left image) 0.48 PV (right image) during ASP flooding.

3.5 Sensitivity Analysis

The model developed in this study has additionally been tested by considering two cases of sensitivity analysis. This test was performed to determine if better oil recovery is achieved by changing the key design parameters, including: (1) the ASP slug size and surfactant concentration, and (2) the combined effect of highly concentrated or diluted injected surfactant together with the ASP slug size. These parameters are investigated in terms of a cumulative recovery of Oil Initial In Place (OIIP), solely by ASP flooding, without taking into account oil recovered by water flooding. These case studies helped optimizing ASP flooding design in

terms of high oil recoveries.

3.5.1 Effect of ASP slug size and surfactant concentration.

The first case was performed by varying the ASP slug size from 0.2 to 0.6, while keeping the rest of the parameters in the model constant, as shown in Table 3.8. The table gives the corresponding cumulative oil recoveries based on OIIP.

Table 3.8: Effect of the ASP slug size and surfactant slug concentration

	case1A	case 1B	case 1C
ASP Slug	0.20 PV	0.48 PV	0.60 PV
Oil recovery (% of OIIP),	20.76	23.78	23.98
	case 1D	case 1E	case 1F
Surfactant concentration	0.2 wt%	0.6 wt%	1.0 wt%
Oil recovery (% of OIIP),	10.87	23.78	23.78

Fig. 3.15 shows that oil recovery from the ASP slug of 0.2 PV was 3% lower at 20.76% than the ASP slug of 0.48 PV at 23.78%. The reason for this is that a smaller amount of oil was produced in the micro-emulsion phase, compared to the original case (1B). The small slug size ensures that the polymer drive starts earlier than the original case and, thus, the size of the oil bank was small. For the largest ASP slug size (0.60 PV), the incremental oil recovery is 23.98%, which is approximately the same as the designed ASP slug of 0.48 PV. This large slug size failed to produce major additional incremental oil recovery due to the presence of a diluted and dispersed surfactant concentration (Mohammadi et al., 2009). Thus, for an optimized ASP slug size, decreasing the slug size from 0.48 PV, would negatively affect the final oil recovery, whereas increasing the slug size would not produce a major change in the final incremental oil recovery.

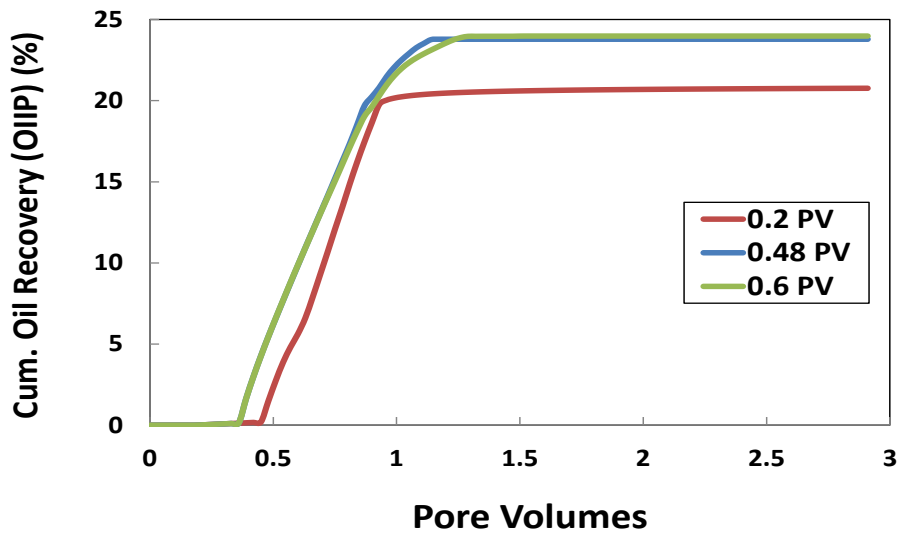


Fig. 3.15: Effect of the ASP slug size on cumulative oil recovery (% of OIRP).

From the results in Fig. 3.16, it is seen that a surfactant concentration of 0.6 wt% was the optimum design. A lower surfactant concentration at 0.2 wt% had an oil recovery of 10.87%, which was significantly lower than the other results. An increase in the surfactant concentration up to 1.0 wt% failed to bring any substantial improvement in incremental oil recovery. The reason was that because of an increase in the surfactant concentration, the micro-emulsion phase volume increased and the flow was dominated by the micro-emulsion phase (Sheng, 2011). Since maximum oil was produced before the chemical breakthrough in the oil bank, the effect of an incremental oil recovery from a large micro-emulsion phase will be low. This indicates that a high surfactant concentration does not bring any advantage in terms of compensation for surfactant adsorption on rock, since the capacity of adsorption can be satisfied with a surfactant concentration lower than 1.0 wt%.

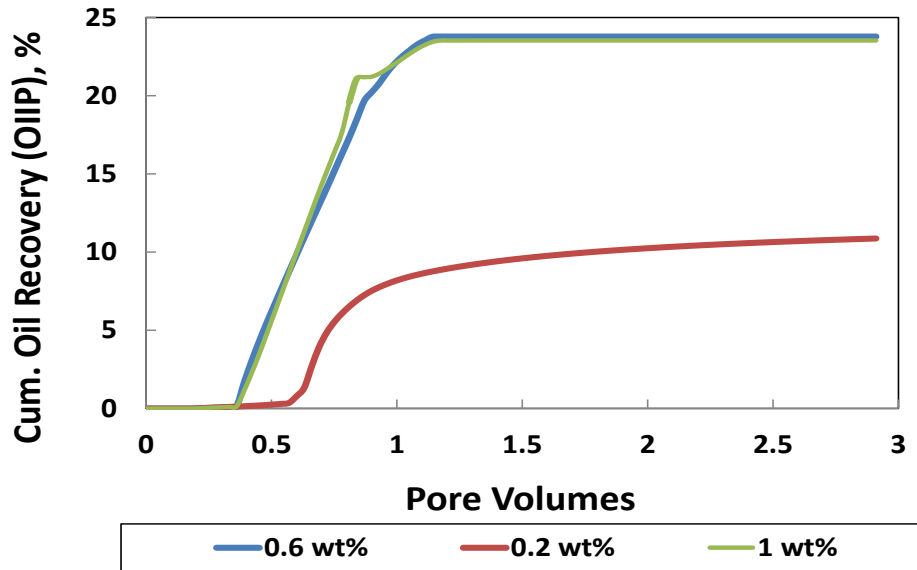


Fig. 3.16: Effect of surfactant concentration on cumulative oil recovery factor (% of OILP)

3.5.2 The combination effect of surfactant concentration and ASP slug size

In Case 2, the ASP slug design parameters were varied to check if a highly concentrated ASP surfactant slug was more desirable than a large ASP slug size with diluted surfactant concentrations. Five different ASP slugs were simulated to test this premise are given in Table 3.9, and the results are shown in Fig. 3.17 and Fig. 3.18.

Table 3.9: ASP slug injection design with sensitivity on the combined effect of slug size and surfactant concentration

Case	ASP slug size, (PV)	Surfactant concentration, (wt%)	Oil recovery, (% of OILP)
2A	0.80	0.3	23.55
2B	0.48	0.6	23.98
2C	0.40	1.0	24.01
2D	0.15	2.0	20.01
2E	0.10	3.0	14.14

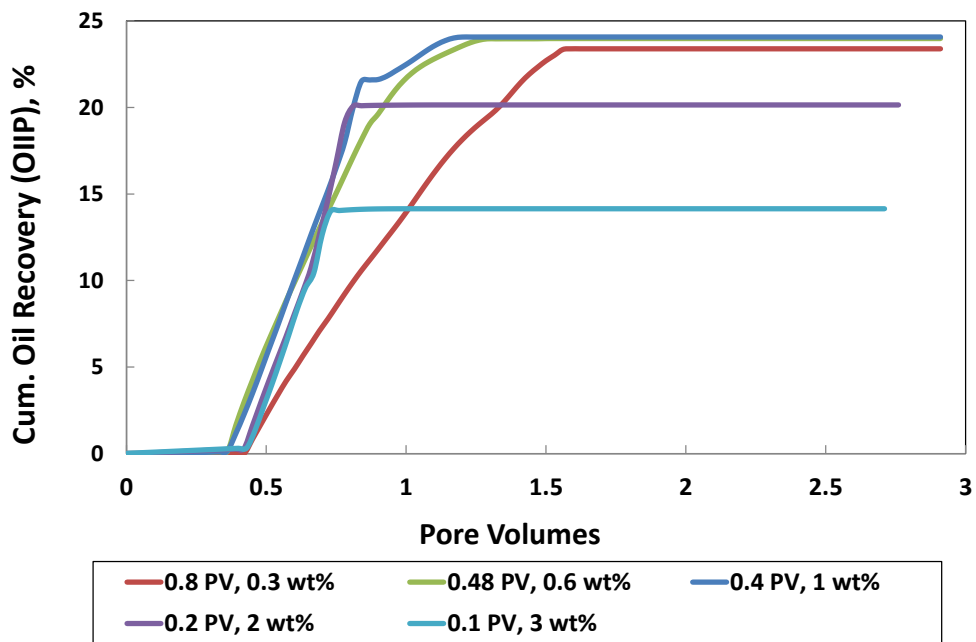


Fig. 3.17: Cumulative oil recovery at different ASP slug sizes and surfactant concentrations

From the results, it was immediately noticeable that for highly concentrated surfactant slugs and low ASP slug size (case 2D; 2E), the oil recovery was low compared to the diluted cases i.e. a large ASP slug size and low surfactant concentration (case 2A; 2B; 2C). Fig. 3.18 shows a large difference in the oil cut production profiles for the two extreme cases (case 2A; 2E). In case 2A, a prominent oil bank was not visible, but a continuous prolonged production was seen. This can be due to the highly dispersed nature of the surfactant particles throughout the system, which lengthen the production life. However, this prolonged oil production fails to bring about any increment in oil recovery, as the oil recovered was similar to the original simulation (case 2A: 23.55%; original simulation: 23.78%). For case 2E, a sharp production profile with a high peak just before the point of the chemical breakthrough at 0.65 PV, due to the highly concentrated nature of the surfactant, was noticed. The highest oil recovery obtained is from case 2C with 24.07%, which was 0.3% higher than the originally designed ASP flooding.

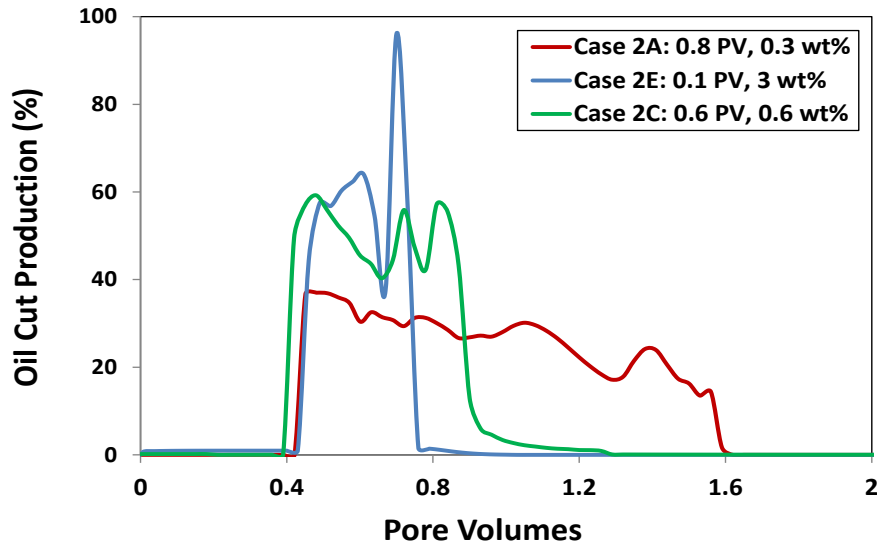


Fig. 3.18: Comparison of the profile of the oil-cut recovered for cases 2A and 2E with the original simulation (Case 2C)

According to the sensitivity studies of the variation in the ASP slug design, an optimum ASP design would be close to Case 2C. However, this design is similar to the originally designed ASP slug, which can be called the optimum design for this study. Simulation results from cases 1 and 2 also confirm the above conclusion. Thus, the original ASP slug is the most favorable design. Nevertheless, only after an extensive economic analysis, other cases can show that in a which extent the increments in oil recovery could be ignored.

3.6 Conclusion

- A numerical simulator coupled with a geochemical module was used to model ASP flooding at the under-optimum salinity condition. A good match of the numerical simulations with the experiments was obtained for the oil-cut, pressure drop, cumulative oil recovery, pH profile, surfactant, and carbonate concentration in the effluents. The simulations gave additional insight into the propagation of alkali consumption, effective salinity, surfactant profiles within the core.
- Based on the ASP flooding design, the effective salinity was perpetually under-optimum below the lower salinity limit. The high oil recovery factors are independent of ultralow IFT values (less than 10^{-2} mN/m) and low residual saturation values are

obtained at the lower optimum salinity limit. The ASP simulation also shows a similar result, in which the effective salinity was close to the lower salinity limit.

- After the chemical breakthrough, higher values of effective salinity for the ASP slug (0.466 mequiv/mL, 2.5 wt% NaCl) were noticed than the designed salinity for the experiment (0.34 mequiv/mL). This variation in salinity is attributed to the geochemical reactions, including a desorption of ions such as Na^+ from the rock through a cation exchange, which influences the alkali consumption as well.
- The divalent cations form complexes with the surfactants that influence the salinities. Furthermore, the alcohol co-solvent in the ASP slug also influences the optimal salinities of the micro-emulsion. Thus, the presence of surfactants and alcohol in the ASP slug causes higher effective salinities than the polymer drive through the divalent cations complexes included in the geochemical reaction model.
- The pH profile of the simulation shows a higher value for the alkali front than the measured data, even though less carbonate was recovered in the simulation than in the measured data. The alkali consumption after the chemical breakthrough in the simulation was lower than in the experiment. This could be improved by taking into account (1) the dissolution of minerals such as quartz even at a pH below 10, and (2) the dissolution and precipitation of clays, such as kaolinite ($\text{Al}_2\text{Si}_2\text{O}_5(\text{OH})_4$), in the geochemical model.
- The main source of alkali consumption was found in the exchange reactions between H^+ and Na^+ . This exchange capacity was seen to shift the point of the chemical breakthrough and the corresponding pH and carbonate fronts.
- A reduction in the ASP slug size from 0.6 PV to 0.48 PV did not affect oil recovery adversely, but a further reduction to ≤ 0.2 PV ASP slug size would likely result in insufficient surfactant propagation and a decrease in oil recovery.
- From the study, it was noticed that there are other factors influencing the injected ASP slug salinity that affect the surfactant phase behaviour of the process. These factors were identified as: alkali-rock reactions, initial salinity state of the reservoir, the

influence of brine in water flooding and the chemicals in the ASP slug, causing a shift in the ASP slug salinity.

- According to the effective salinity calculated during the ASP EOR process, the numerical simulation developed in this work can be used to reject the ASP flooding systems which could lead to the over-optimum salinity condition. This reduces the risk of a surfactant trapping and losses, due to a migration of surfactant into the oil-rich phase in over-optimum salinity conditions in the field.

Chapter 4

Investigation of Certain Physical-Chemical Features of Oil Recovery by an Optimized Alkali-Surfactant-Foam System

4.1 Abstract

This chapter presents a laboratory study of the Alkali-Surfactant-Foam (ASF) EOR method to better understand its mechanisms under bulk conditions. The focus is on the interaction of ASF chemical agents with oil in the presence and absence of a naphthenic acid component and *in-situ* soap generation. To do so, the impact of alkalinity, salinity, IFT reduction and *in-situ* soap generation were systematically studied by a comprehensive measurement of 1) micro-emulsion phase behaviour using a glass tube test method, 2) interfacial tension, and 3) foam stability analysis. This approach aims to discover a synergistic effect between micro-emulsion phase behaviour and foam stability in bulk and to design a high-performance chemical system for an optimal ASF EOR process. In this study, the presented alkali-surfactant (AS) formulation lowered the IFT between the oil and aqueous phase from nearly 30 mN/m to 10^{-1} - 10^{-3} mN/m. This allows the chemical formulation to create a considerably low IFT-foam

The content described in this chapter is published in: Hosseini-Nasab et al. (2017). "Investigation of Certain Physical-Chemical Features of Oil Recovery by an Optimized Alkali-Surfactant-Foam (ASF) System", Just accepted in the Journal of Colloid and Polymer Science, Springer.

flooding, with a higher capillary number than conventional foam, for displacing trapped oil from porous media. In the foam stability analysis of different ASF agents in the absence and presence of an oil phase, several characteristics, such as foam volume evolution, foam half-decay time and a liquid fraction of foam, were measured over a wide range of surfactant, alkali and electrolyte concentrations, and oil saturations. Bulk foam stability tests demonstrated that the stability of foam diminishes in the presence of oil with large volumes of *in-situ* soap generation. Furthermore, the results, obtained for foam stability in the presence of oil, were interpreted in terms of phenomenological theories of Entering/Spreading/Bridging coefficients and the Lamella Number.

4.2 Introduction

Foam has shown promise as a drive fluid for IOR and EOR, particularly for shutting off unwanted gas production in production wells in the field applications of carbon dioxide (CO₂) and nitrogen (N₂) foam flooding, and steam flooding (Holm, 2013; Mohammadi et al., 1989; Sohrabi & Farzaneh, 2013). Foam can have a greater apparent viscosity than displaced fluids by drastically lowering gas mobility, which is essential to improve volumetric sweep efficiency of the gas flooding EOR process (Mannhardt et al., 2000; Sagar & Castanier, 1997). Foam improves volumetric sweep efficiency, especially in heterogeneous reservoirs, but its microscopic displacement efficiency is low (Hirasaki et al., 2004; Li et al., 2010). In reservoirs with a high variation of permeability, strong foam will form in higher permeability zones, leading to the diversion of the flow from high to low permeability zones (Cottin et al., 2012; Li et al., 2010).

Foam has also been identified as an attractive alternative to polymer in ASP flooding for either low permeability reservoir formations or for reservoirs with high salinity formation water (Lawson & Reisberg, 1980; Srivastava et al., 2009). Foam offers better properties than polymers for conformance control issues, due to the fact that foam can divert flow from high permeable regions to low permeable regions (Srivastava et al., 2010). ASF flooding has been developed as a new technique, which uses foam as a mobility control agent instead of polymer, and provides a low IFT to increase the capillary number (Guo et al., 2012; Li et al., 2012).

Others have proposed similar processes under the name of Alkali-Surfactant Gas (ASG) or Low Tension Gas (LTG) flooding (Szlendak et al., 2013; Tang et al., 2014; Wu et al., 2010). Alkali-Surfactant (AS) formulations reduce IFT, leading to an increase in the capillary number, in order to mobilize the residual oil, which is trapped by capillary forces (Yuqiang et al., 2008; Kang et al., 2010; Hosseini-Nasab et al., 2016). A process, based on the relationship between micro-emulsion phase behaviour screening and IFT variation, has been described for evaluating potential EOR surfactants (Iglauer et al., 2010; Levitt et al., 2009).

Surface-active molecules, such as surfactant and soap molecules, adsorb onto the gas-liquid interfaces. They stabilize foam by inducing repulsive forces in the lamellae, modifying the viscoelasticity of gas-liquid interfaces and reducing the gas-liquid surface tension (Gauchet et al., 2014; Karakashev et al., 2012; Stubenrauch & Klitzing, 2003). The surface behaviour of the systems containing surface-active agents depends significantly on the temperature, salinity, the charge density of electrolyte and the length of the hydrocarbon chain in the surfactants (Campbell et al., 2011; Petkova et al., 2012; Worthen et al., 2013). Recently it was shown that the surface tension behaviour in foam structures can also be influenced by mechanical agitation of the solutions (Campbell et al., 2011). Bulk foam tests can be used to investigate foam stability with respect to various parameters, such as type, composition, and the concentration of surfactant, oleic phase, gas and electrolyte (Jones et al., 2016; Lavergne et al., 2011).

During field applications, foam may encounter varying conditions, such as a range of oil saturations and different salinities. Therefore, foam should be designed to be stable for varying oil saturations and salinity. Because of a varying residual oil saturation in the reservoir, strong foam could create a large pressure gradient which may cause a fracture in the reservoir. In cases where foam is injected into swept zones with a low oil saturation, intermediate or low stability foam in the presence of oil may be adequate. Moreover, although foam improves volumetric sweep efficiency, its microscopic displacement efficiency is low. Therefore, an understanding of how foam behaves physico-chemically under bulk conditions in an oil recovery process is of great importance.

Thus, this paper aims to discover a synergistic effect between micro-emulsion phase behaviour and foam stability in bulk, and to design a high-performance chemical system for an

optimized ASF EOR process. The study of micro-emulsion phase behaviour and of the foaming stability of selected chemicals in the absence and in the presence of model oil, with and without naphthenic acid, was first undertaken. The focus on the foam stability screening test was to specifically address the impact of the surfactant concentration, salinity, alkalinity, oil saturation, IFT and *in-situ* soap generation. To this end, the obtained results for foam stability in the presence of oil are discussed in terms of the classical entering/spreading coefficient, the Lamellae number and the stability of pseudo-emulsion film. Finally, the main conclusions of this study are drawn.

4.3 Theoretical Background

4.3.1 Entering, Spreading & Bridging Coefficients, Lamella Number

Several mechanisms of foam/oil interaction have been suggested in the literature. Four main parameters have emerged as predictors of foam stability in the presence of oil: spreading and entering coefficients, the lamella number and pseudo-emulsion film models (Koczo and Lobo, 1988; Koczo et al., 1992; Nikolov et al., 2013). Foam may become unstable when an oil droplet enters the gas-water interface under favourable thermodynamic conditions, leading to the rupture of the foam lamellae. The ability of an oil droplet to enter the gas–water interface is expressed by the entry coefficient (E) defined as follows (Robinson & Woods, 1948),

$$E = \sigma_{gw} + \sigma_{ow} - \sigma_{og} \quad (4-1)$$

where σ_{gw} , σ_{ow} , and σ_{og} are the foaming solution surface tension, the interfacial tension (IFT) between the initial foaming solution/oil, and the surface tension of the oil phase, respectively. If E is negative, then the oil droplet cannot enter the foam interface, the oil droplet remains in the liquid phase, and there is no detrimental effect of the oil on the foam film. If $E > 0$, then it is thermodynamically favourable for oil to enter the gas-water interface. If the entry condition is favourable, then oil might spread on the gas/water interface. Attempts to correlate the spreading behaviour of oil droplets to foam destruction by oil, form the basis for most of the work performed on oil destabilization mechanisms (Schramm & Smith, 1996). The spreading

coefficient (S) for an oil-foam system is given by:

$$S = \sigma_{gw} - \sigma_{ow} - \sigma_{og} \tag{4-2}$$

when S is negative, oil does not spread and, instead, oil droplets form lenses at the gas–water interface. For a positive spreading coefficient (S), oil spreads over the liquid-gas interfaces and the resulting foam film may rupture once the oil drop enters both surfaces of the lamella (Vikingstad et al., 2005). Under this condition, an oil droplet can span through the film lamella by making a meta-stable bridge (i.e. B is positive). Bridging coefficient B is defined as an indication of the mechanical stability of oil bridging on foam destabilization (Harkins, 1941),

$$B = \sigma_{gw}^2 + \sigma_{ow}^2 - \sigma_{og}^2 \tag{4-3}$$

When the B coefficient is positive, then the film lamella is unstable, while negative values of B lead to a stable film. Table 4.1 gives a summary of the foam stability prediction by the negative/positive signs of the E , S and B coefficients.

Table 4.1: Foam stability prediction by the negative/positive signs of the E , S and B coefficients

Entry coefficient E	Spreading coefficient S	Bridging coefficient B	Foam stability condition
negative	negative	not defined	stable foam
positive	negative	negative	stable foam
positive	negative	positive	unstable foam
positive	positive	negative	moderate stable foam
positive	positive	positive	unstable foam
negative	positive	negative	stable foam
negative	positive	positive	unstable foam

Schramm and Novosad (1990, 1992) proposed the use of another dimensionless parameter called the Lamella number (L) to investigate foam stability in the presence of oil. This parameter describes foam stability based on oil emulsification in the foam structure and the movement of oil droplets into the foam lamellae. Lamella number (L) is defined as a ratio of

the capillary pressure at Plateau borders to the pressure difference across the oil–water interface:

$$L = \frac{\Delta P_C}{\Delta P_R} = \frac{r_o}{r_p} \frac{\sigma_{gw}}{\sigma\theta_{ow}} \quad (4-4)$$

where r_o is the radius of an oil droplet and r_p is the radius of the Plateau border. They defined three types of foam depending on the value of the lamella number (L): type *A* foam for $L < 1$, type *B* foam for $1 < L < 7$, and type *C* foam for $L > 7$ (Schramm & Novosad, 1990, 1992). Table 4.2 presents a summary of the foam stability prediction by the lamella number theory.

Table 4.2: Foam stability prediction by the lamella number theory

Type of Foam	Foam stability to oil	E	S	Lamella number (L)
<i>A</i>	quite stable foam	negative	negative	$L < 1$
<i>B</i>	moderately stable foam	positive	negative	$1 < L < 7$
<i>C</i>	quite unstable foam	positive	positive	$L > 7$

4.3.2 Surfactant Phase Behaviour

The main objective of micro-emulsion phase behaviour is a selection of chemical formulations for a specific chemical EOR application. The thermodynamically stable micellar phase, which is clear and composed of surfactant, brine, and oil, is called ‘micro-emulsion’ (Bourrel & Schechter, 1988; Quintero et al., 2011). Micro-emulsion phase behaviour tests commonly include the salinity scan, an aqueous-phase stability measurement, and an oil scan. The micro-emulsion phase changes from type I (oil in excess water phase) to type III (a bi-continuous oil/water phase), and then to type II (water in excess oleic phase) as the salinity increases (Winsor, 1954). The characteristic transition of micro-emulsion from type I to type III to type II by increasing the salinity can be represented by a volume fraction diagram, which indicates the sensitivity of the surfactant solution behaviour to additional electrolytes (Sheng, 2011). Healy et al. (1976) first introduced the concept of ‘optimum salinity’ and proposed an empirical correlation between water/oil solubilization ratios and the IFT between the micro-emulsion and each excess phase. Optimum salinity corresponds to the salinity where equal

volumes of water and oil are solubilized in the middle phase in Winsor type III of micro-emulsion phase behaviour. The intersection of the plots of V_o/V_s and V_w/V_s as a function of salinity, gives the optimum salinity and the optimum solubilization ratio. Huh (1979) developed a theoretical relationship between IFT and the oil/water solubilization ratio as follows:

$$\gamma = \frac{C}{\sigma^2} \quad (4-5)$$

where C is approximately 0.3 dynes/cm for typical oils and surfactants, and σ is the solubilization ratio. When the optimum solubilization ratio is equal to or larger than 10, then IFT at optimum salinity is in the order of 10^{-3} mN/m or less (Zhao et al., 2008). This IFT reduction is sufficiently low to mobilize the trapped residual oil by capillary forces. Therefore, in this work, we targeted the optimum solubilization ratio of 10 or higher for the micro-emulsion phase behaviour study.

In this chapter, IOS surfactant was used for all the experimental investigations, as this type of surfactant has been shown to have a low IFT and to be a relatively stable foam (Guo et al., 2012; Hosseini-Nasab et al., 2016). In oil/brine/surfactant mixtures, IOS surfactants usually do not exhibit a tendency to form liquid crystals, gels or ordered structures in spite of lacking branches (Barnes et al., 2010; Zhao et al., 2008). It was found that high molecular weight Internal Olefin Sulfonate (IOS) surfactants perform remarkably well with difficult oils in terms of providing an efficient micro-emulsion in comparison to many other types of surfactants (Zhao et al., 2008).

4.3.3 Role of Alkalinity in ASF EOR

Alkalis used in the chemical flooding EOR interact with carboxylic acids of the crude oil, where they generate *in-situ* surfactant (soap) and which reduces interfacial tension (Ojukwu et al., 2013). The alkali-oil chemistry is described by a partitioning of the naphthenic acid between the oleic and aqueous phases and subsequent hydrolysis in the presence of alkali to produce an anionic surfactant A^- . DeZabala et al. (1982) suggested a chemical model definition for the alkali-oil saponification. Acid, that existed in the oil phase by interaction with alkali,

will have some aqueous solubility and will distribute itself between the oleic and aqueous phases represented by Eq. 6:



where HA_o is the oleic phase acid, and HA_w is the aqueous phase acid. Water-soluble anionic surfactant (A^-) can be generated from oleic phase acid HA_o by the following extraction and hydrolysis equation:



The generated A^- ion will adsorb at oil-water interfaces and lower the IFT. The acid dissociation constant (K_A) for Eq. 6, the partition coefficient of the molecular acid K_D and the dissociation constant of water (K_w) are as follows:

$$K_A = \frac{[H^+][A^-]}{[HA_w]} \quad (4-9)$$

$$K_D = \frac{[HA_w]}{[HA_o]} \quad (4-10)$$



$$K_w = [H^+][OH^-] \quad (4-12)$$

An increase in $[OH^-]$ results in a decrease in $[H^+]$. p_H is defined as $-\log[H^+]$. At high pH, the concentration of soap in the aqueous phase is (Sheng, 2011):

$$[A^-] = \frac{K_A K_D [HA_o]}{[H^+]} = \frac{K_A K_D [HA_o][OH^-]}{K_w} \quad (4-13)$$

4.4 Experimental Materials and Methods

4.4.1 Materials

Brine containing sodium chloride (NaCl, Fisher Scientific) in deionized water ($\text{pH} = 6.8 \pm 0.1$) was used to prepare the surfactant solution. The alkaline solutions were a mixture of sodium carbonate (Na_2CO_3) and sodium chloride that were obtained from Fisher Scientific Company with ACS purity. Nitrogen gas with a purity of 99.98% was used to generate foam. Normal hexadecane (n-C16, Sigma) as the model oil was used to represent the oleic phase. Hexadecane as the model oil was used with and without a naphthenic acid, which was Decanoic Acid (99% pure, Sigma) in this study. 0.25 wt% of Decanoic acid dissolved in n-hexadecane was used, giving a Total Acid Number (TAN) of 2.2 (mg KOH/g oil) determined by the ASTM method D664. A commercial IOS with a high number of carbon chains, prepared by the Shell Chemical Company, was selected. The synthesis steps and the chemical structures of IOS surfactant were reported by Barnes et al. (2008, 2012). The surfactant solution was prepared using brine containing NaCl or a blend of NaCl and Na_2CO_3 .

4.4.2 Micro-emulsion Phase Behaviour Tests

Samples for phase behaviour studies were prepared in test tubes by adding equal amounts of aqueous chemical formulation and oleic phase (i.e. Hexadecane). The samples were thoroughly mixed and were allowed to equilibrate in atmospheric pressure at temperature $T = 60$ °C. They were several times briefly removed from the oven during equilibration, to be shaken by hand a few times and were replaced. This procedure was continued until the phase volumes remained unchanged. The phase characteristics of each system were recorded as the relative volumes of the aqueous and oleic phases, and, if present, the middle phase (Wu et al., 2010). The test tubes are shown in Fig. 4.1.



Fig. 4.1: Phase behaviour of IOS and n-hexadecane with the glass tube salinity scan method. Salinity (NaCl) varies from left to right 1.0 to 6.0 weight per cent in the surfactant solution.

4.4.3 Surface and Interfacial Tension Measurements

The ST and IFT were measured using a KSV Sigma tensiometer by the DuNouy ring method. The gas above the oil and water was air for the ST measurements. The measurements, at ambient temperature (21 ± 1 °C) under atmospheric pressure, were conducted for a sufficiently long time until constant values were obtained. The low IFT between the oil phase and water phase was measured using a SITE100 spinning drop tensiometer (Kruss). The apparatus used in this study is displayed in Fig. 4.2.

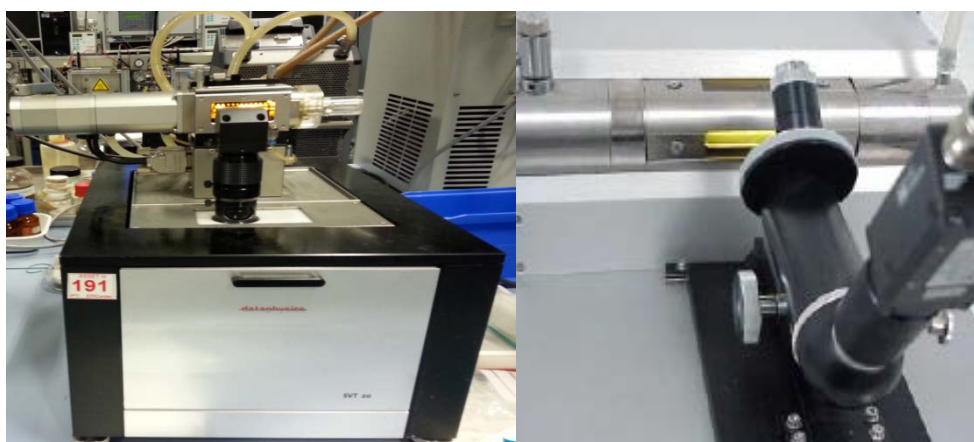


Fig. 4.2: Photograph of the spinning drop tensiometer with temperature controller of the cell with capillary diameter 2.5 mm. Measuring range in IFT measurement is from 10^{-5} mN/m. Rotational speed up to 15,000 rpm (optionally up to 20,000).

For the measurement, a capillary tube was horizontally placed and filled with a heavy bulk phase and with a distinctly light drop phase, as shown in Fig. 4.3. The capillary tube was rotated to induce the action of centrifugal force. To measure an ultra-low IFT, the original balance between gravity and IFT should be artificially altered to enable the shape of the balanced droplet to be easily measured.



Fig. 4.3: Schematic representation of the spinning drop method

The capillary tube rotates at a certain angular velocity so that the light drop phase, surrounded by the heavier phase, is located in the middle of the tube. At equilibrium, the drop radius, perpendicular to the axis of rotation, depends on the IFT between the phases, the angular frequency, and the density differences. The IFT σ (dyne/cm) is given by the Vonnegut’s equation (Su, 2012):

$$\sigma = 3.42694 \times 10^{-7} (\rho_w - \rho_o) \omega^2 D^3 \tag{4-14}$$

where ρ_w and ρ_o is the density of water (out) and oil (drop) phase in g/cm^3 , respectively, ω is the rotational velocity in RPM, D is the measured drop width (diameter) in mm, and L is the length of the oil drop in mm. The drop diameter is calculated from video images of the drop by means of drop shape analysis. In order to minimize the error due to the curvature of the interface, in the cases where alkaline or/and surfactants were added to the water phase, the speed of rotation was sufficiently high to ensure that the length of the oil drop is at least four times larger than its diameter.

4.4.4 Bulk Foam Stability

The foaming properties of the selected chemicals used in the micro-emulsion phase

behaviour study were tested by using the Foam Scan apparatus (IT Concept, France). Foam was generated in the apparatus by sparging nitrogen gas at a fixed gas flow rate of 16 ± 1 cm^3/min through a porous glass plate into a certain volume of surfactant solution (50 ± 1 cm^3). The gas flow stopped automatically when the foam volume reached a pre-set value of 150 cm^3 . The foam volumes were monitored with real-time images of the foam column during the generation of foam and the subsequent foam drainage, which were recorded by a CCD camera. Several electrodes were attached to the foam column at different heights, which enabled the amount of liquid volume in the foam to be measured by conductivity measurements. A pair of electrodes was applied at the bottom of the column to record the amount of liquid which was outside of the foam structure. The Foam Scan instrument used in this study is displayed in Fig. 4.4 along with a snapshot of a foam column.

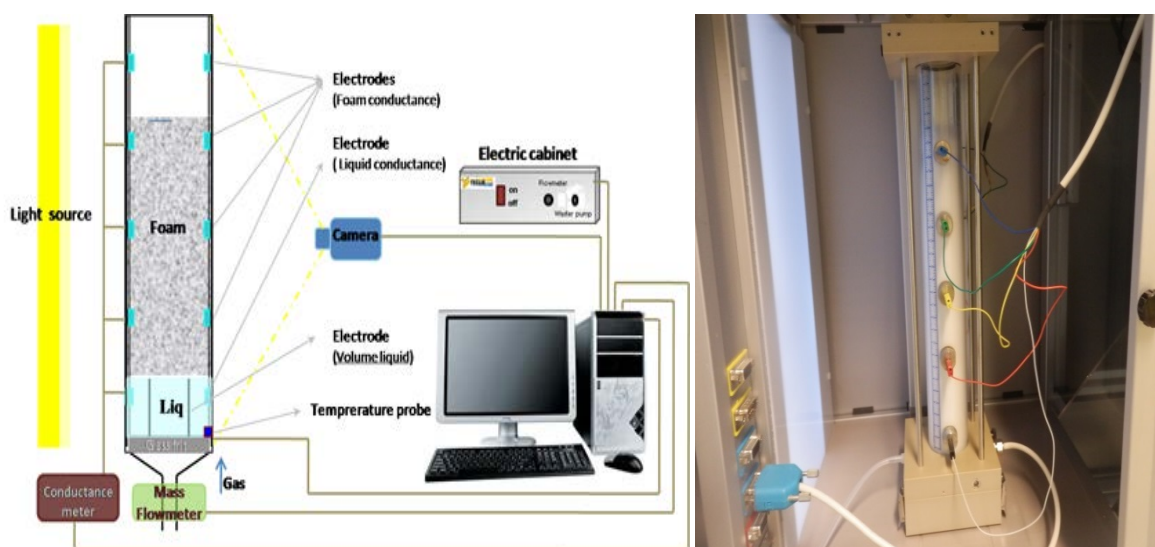


Fig. 4.4: Schematic representation and snapshot of the Foam Scan set-up showing the mass flowmeter to control the air flow, and the optical camera for monitoring the height of foam column to determine the foam volume. Liquid volume in the foam structure was obtained by the conductivity measurement along the glass column.

The following parameters were measured in experiments with the Foam Scan: the foam volume and the liquid volume content of foam versus time during gas sparging (foamability), and the decay of the foam volume and liquid volume content of foam after stopping gas sparging (foam stability). Foam stability was assessed by measuring the half-decay time $t_{1/2}$, i.e. the time required to collapse the foam volume by one-half ($1/2$) of the initial height of the foam column. The Foam Scan apparatus can determine simultaneously the liquid volume in the

foam structure, the measurement of other parameters such as Foaming Capacity (*FC*) and foam Maximum Density (*MD*). These data are used to analyse foam stability. The foamability of the surfactant solutions was described by the *FC* and *MD* coefficients.

$$\text{Foam capacity (FC)} = \frac{\text{final foam volume}}{\sum \text{gas volume injected during sparging phase}} \quad (4-15)$$

$$\text{Maximum density (MD)} = \frac{\text{maximum liquid volume in the foam}}{\text{final foam volume}} \quad (4-16)$$

The *FC* coefficient is the ratio of foam volume at the end of gas sparging to the total gas volume injected. The *FC* coefficient is higher than the unity for stable foam. When part of the injected gas does not reside in foam, the *FC* value of the experiment will be smaller than one (1), which could be an indication of un-stability during the foam process. The *MD* coefficient was defined as a ratio of the liquid volume in the foam to the final foam volume. The maximum density provides insight in the liquid hold-up of the generated foam, the wetter the foam is, the higher the *MD* value will be (Simjoo et al., 2013).

4.4.5 Experiments Overview

a) Salinity scan. Firstly, chemical systems containing surfactant, electrolyte and model oil, either with or without alkali and organic acid, were tested in the micro-emulsion phase behaviour experiment to identify the composition of the chemical slug and the drive for ASF flooding. In order to identify the micro-emulsion phase boundary, Winsor phase behaviour experiments of brine-surfactant-oil systems were performed under the specific conditions of salinity, surfactant concentration and oil type, as demonstrated in Table 4.3. Two types of micro-emulsion were generated: one is from a surfactant, alkaline/surfactant (AS) solution with *n*-hexadecane, and the other type is an alkaline/surfactant (AS) solution with an organic acidic mixture of *n*-hexadecane. For the salinity scan test in the phase behaviour study, the water/oil ratio was equal to one. Information relevant to the observed type of various phase behaviours (such as Winsor I, Winsor II or Winsor III) was visually observed at equilibrium conditions.

Table 4.3: Overview of the all surfactant phase behaviour experiments by the salinity scan method

System	Surfactant Conc. (wt%)	Electrolyte Type	Oil Type
1	0.5	NaCl	<i>n</i> -Hexadecane
2	0.5	Na ₂ CO ₃ /NaCl	<i>n</i> -Hexadecane
3	0.5	Na ₂ CO ₃ /NaCl	<i>n</i> -Hexadecane+ naphthenic acid
4	1.0	NaCl	<i>n</i> -Hexadecane
5	1.0	Na ₂ CO ₃ /NaCl	<i>n</i> -Hexadecane
6	1.0	Na ₂ CO ₃ /NaCl	<i>n</i> -Hexadecane+ naphthenic acid

b) Foamability and foam stability. The foamability and foam stability of the different systems considered in the micro-emulsion phase behaviour study were examined by investigating the effect of several parameters. First, the effect of surfactant concentration on the stability of IOS foam in the absence and presence of the oil was investigated, where oil saturation was 5.0 % by volume. Then, in order to understand the impact of oil saturation on foam stability, the generated foam containing 1.0 wt% IOS was exposed to the different volume concentrations of *n*-hexadecane. The amounts of liquid volume until the maximum value was reached were measured; these were obtained at different times depending on the surfactant concentration and oil saturation. In the next step, to demonstrate the effect of salt and alkalinity on the foam stability, the decay time of the foam column was halved, using the 1.0 wt% IOS surfactant throughout the range of salt and alkaline concentration. Finally, the effects of *in-situ* soap generation and IFT on the stability of foam were investigated. All of the foamability and foam stability experiments performed in this study are listed Table 4.4.

Table 4.4: Overview of all the foamability and foam stability experiments by the foam scan method

Experiment	Changing Parameters	Surfactant Conc. (wt%)	Electrolyte Type	Oil Type
1	Surfactant concentration	0.1 up to 2.0	NaCl	Without oil
2	Surfactant concentration	0.1 up to 2.0	NaCl	<i>n</i> -Hexadecane
3	Oil saturation	1.0	NaCl	<i>n</i> -Hexadecane
4	NaCl concentration	1.0	NaCl	Without oil
5	Na ₂ CO ₃	1.0	Na ₂ CO ₃	Without oil
6	Na ₂ CO ₃ concentration	1.0	NaCl/ Na ₂ CO ₃	<i>n</i> -Hexadecane with naphthenic acid

4.5 Results and Discussion

4.5.1 Surfactant Phase Behaviour Investigation

Fig. 4.5 and Fig. 4.6 show solubilization parameters (V_o/V_s) and (V_w/V_s) for the systems presented in Table 4.3. The oil, brine, and surfactant solubilisation volumes, V_o , V_w , and V_s , in the micro-emulsion phase, were estimated from the phase volumes. The figures present the solubilization parameters on the total salinity of two systems, containing 0.5 and 1.0 active weight percentage of IOS surfactant, and how it equilibrate with the model oil. In these two plots, the data points of the oil solubilization ratio are connected with the dashed line, while the water solubilization ratio is shown by the dotted line. The intersection of the plots of V_o/V_s and V_w/V_s as a function of salinity gives the optimum salinity and the optimum solubilization ratio. Optimum salinity corresponds to the salinity that equal volumes of water and oil are solubilized in the middle phase in Winsor type III of micro-emulsion phase behaviour.

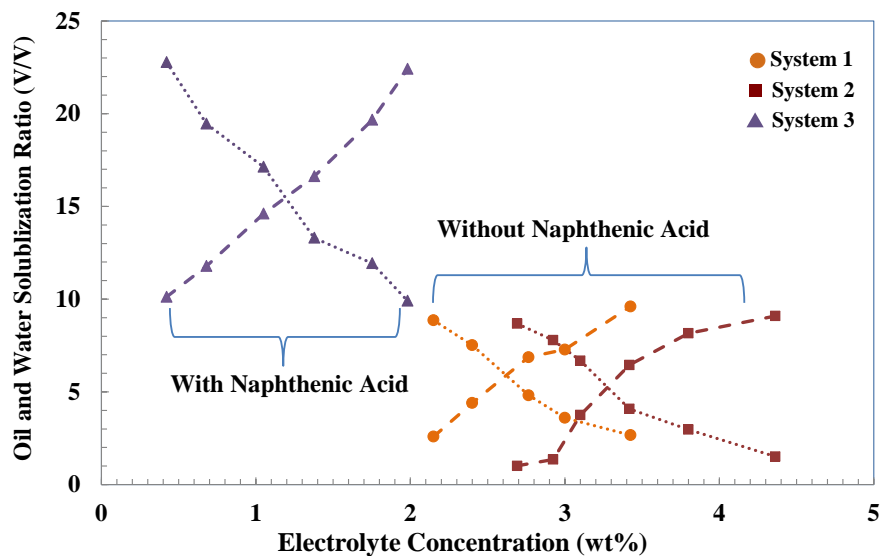


Fig. 4.5: Solubilization ratio of oil and water for systems containing 0.5 wt% IOS surfactant solution contacting hexadecane model oil with a variation of NaCl concentration. Dotted line: connecting water phase solubilization ratio; dashed line: connecting oil phase solubilization ratio.

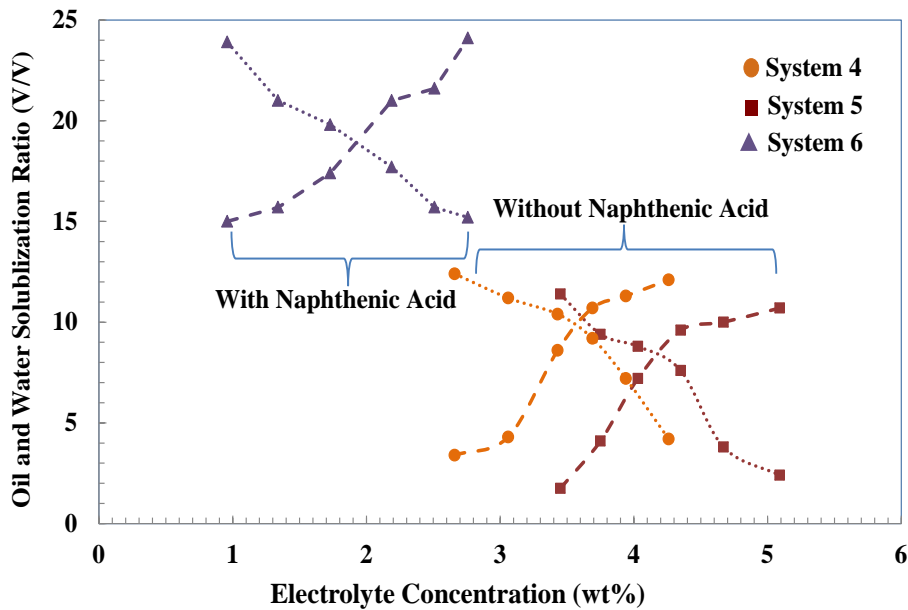


Fig. 4.6: Solubilization ratio of oil and water for systems containing 1.0 wt% IOS surfactant solution contacting hexadecane model oil with a variation of NaCl concentration. Dotted line: connecting water phase solubilization ratio; dashed line: connecting oil phase solubilization ratio.

Optimum salinities, where the two solubilization parameters have equal values (V/Vs) according to Fig. 4.5 and Fig. 4.6; solubilization parameters (measured at optimum salinities) and optimal IFT for all the examined systems are summarized in Table 4.5. IFTs at optimum salinity were obtained by a spinning drop tensiometer through the drop shape analysis; Fig. 4.7 shows the example of images used for drop shape analysis for the range of IFT values.

Table 4.5: Experimental data of the surfactant phase behaviour study for three types of chemical systems containing 0.5wt% and 1.0wt% IOS surfactant at optimal conditions

Systems	Electrolyte	Oil Phase	Optimum Salinity (wt% NaCl)	Optimum Solubilization Ratio	IFT at Optimum Salinity (mN/m)
1	NaCl	Hexadecane	3.2	5.90	9.19 E -2
2	NaCl- Na ₂ CO ₃	Hexadecane	2.6	7.10	6.35 E -2
3	NaCl- Na ₂ CO ₃	Acidic Hexadecane	1.1	15.95	1.19 E -3
4	NaCl	Hexadecane	4.1	9.75	3.37 E -2
5	NaCl- Na ₂ CO ₃	Hexadecane	3.5	10.50	2.9 E -2
6	NaCl- Na ₂ CO ₃	Acidic Hexadecane	1.9	19.90	6.86 E -4

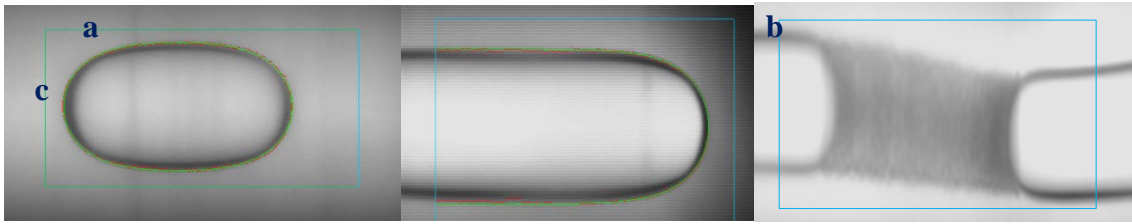


Fig. 4.7: Oil droplet shapes in the range of IFT values with the aqueous solution of IOS surfactant with salinity and alkali in the capillary tube of a spinning drop tensiometer: (a) relatively low IFT (1 to 5 mN/m) (b) low IFT (1 to 10^{-2} mN/m) (c) ultralow IFT (less than 10^{-2} mN/m).

Table 4.5 shows the phase behaviour results comparing the optimum salinity, solubilization ratio and IFT values of systems with and without alkali, contacting with and without acidic model oil. The measured data indicate that the addition of both alkalis and surfactant to the water phase does not reduce the IFT substantially, as shown in Fig. 4.5, according to the water and oil solubilization ratio values. A much greater reduction can be obtained by the generation of *in-situ* soap in the system. As a rule of thumb, systems that give larger oil recovery factors in porous media exhibit an IFT of nearly 10^{-3} dyne/cm. Indeed, values of solubilization ratios (V/V_s) exceeding 10 should lead to sufficiently low IFT to mobilize the residual trapped oil by capillary forces, as this criterion was met by all systems containing 1.0 wt% surfactant. However, for an aqueous solution containing 0.5 wt% of IOS surfactant, we can only see where soap generation-assisting IFT reduction exists in a system with organic acidic oil.

The data suggests that this particular model oil with 1.0 wt% IOS surfactant lowers IFT more than 0.5 wt%, and, therefore, oil can be mobilized more easily in the displacement experiments in porous media. As it was our goal to design a chemical formulation for ASF flooding, this data indicates the impact of the presence of alkalinity, soap generation and surfactant concentration on a range of optimum salinity, solubilization parameters and IFT values. The series of experiments shows the importance of high values of the oil/water solubilization ratio and, consequently, the effect of the amount of IFT reduction in the displacement of oil in ASF flooding in the latter porous media experiment for our future work. This shows that the used type of IOS surfactant can be applied over a range of salinities with a high solubilization of oil at optimum salinities. Moreover, the results indicate that use of suitable IOS surfactants is a promising approach for designing a chemical formulation for ASF

flooding EOR processes.

4.5.2 Bulk Foam Stability

4.5.2.1 Effect of Surfactant Concentration and Oil Saturation

In this section, we investigate the effect of the surfactant concentration with and without the contacting oil phase, as well as the effect of oil saturation on foamability and foam stability. Firstly, to investigate the effect of the IOS surfactant concentration on the stability of foam, the concentration was varied from 0.1 to 2.0 wt%, but in all the other experiments the IOS concentration was kept constant at 1.0 wt%. Foam drainage, i.e. the decay of liquid volume in the foam as a function of time, is depicted in Fig. 4.8 and Fig. 4.9 in the absence and presence of an oleic phase, respectively. Fig. 4.8 shows the evolution of liquid volume hold-up in the foam structure for the different surfactant concentrations as a function of time during foam generation and drainage after switching off the air sparging.

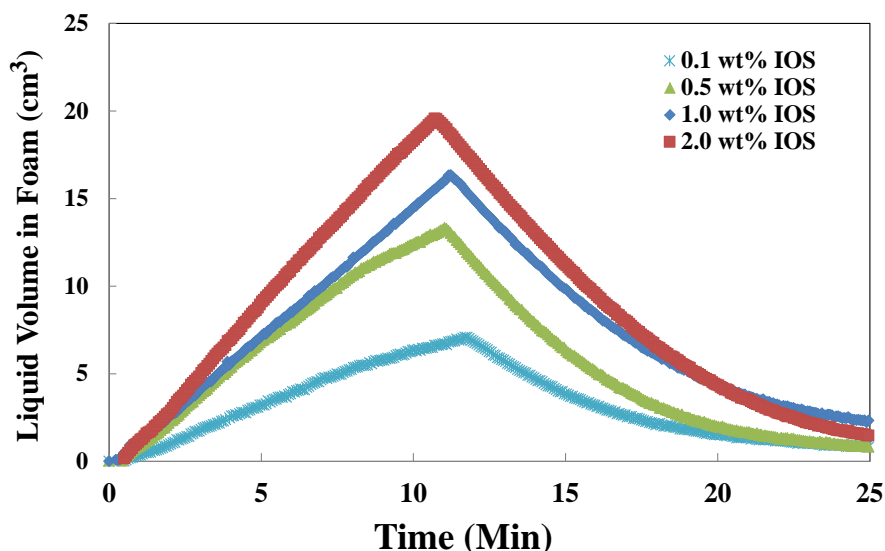


Fig. 4.8: Effect of IOS surfactant concentration in the absence of an oil phase illustrated by a change in the liquid volume of foam during foam generation and after termination of gas sparging as a function of time. The initial liquid volume of the generated foam is 50 cm^3 and the maximum volume of generated foam are illustrated.

Data in Fig. 4.8 show that IOS foam grows linearly with time during foam generation. The straight line in the foam liquid-volume profile indicates a stable build-up of foam volume, and, thus, a IOS foam evolution is not affected by the destruction processes, such as coalescence and Ostwald ripening during foam generation (Carey & Stubenrauch, 2009). Fig. 4.8 also

shows that liquid hold-up increases with surfactant concentrations, which can be explained that with increasing surfactant concentration, the bubble size decreased, which results in the intense fine foam texture, as visually observed during the experiments. Within longer periods of foam stability, it was observed that the average bubble size increases with a decreasing surfactant concentration due to bubble coalescence. Though the maximum amount of liquid ($V_{L,max}$) in the foam for the higher surfactant is larger, the time taken to reach the $V_{L,max}$ is correspondingly shorter. This implies a larger foamability for the higher surfactant concentration is due to the higher amount of adsorbed surfactant, and the larger transport rate of surfactant to the aqueous phase/gas phase interface. This leads to the strength of a electrostatic double layer effect as well as the Gibbs-Marangoni effect, which both result in a more stable foam at the higher surfactant concentration (Myers, 2005). Fig. 4.9 shows similar experiments in the presence of oil with various levels of oil saturation in the foam column 1.0 wt% IOS surfactant. To gain further insight into the effect of oil saturation on foam properties, the foam capacity (FC) and the maximum density (MD) were measured as demonstrated in Fig. 4.10.

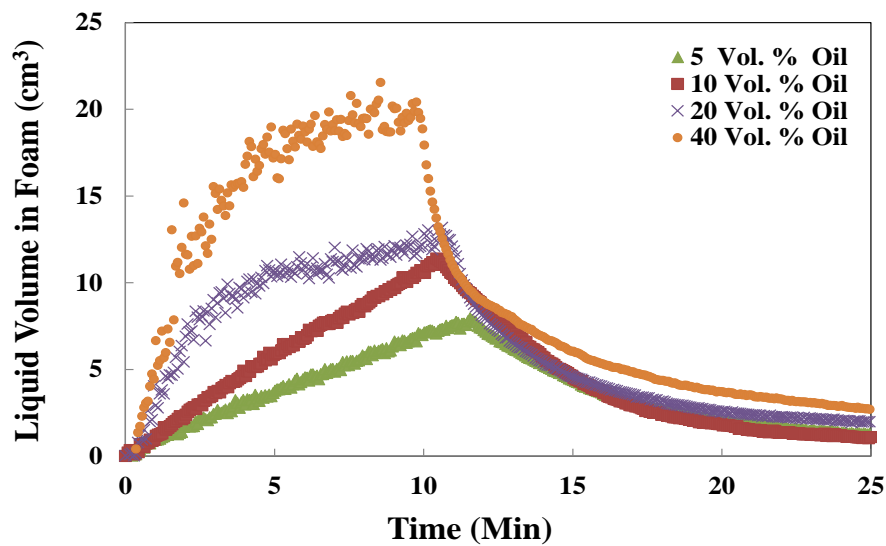


Fig. 4.9: The change in the liquid volume of foam during foam generation and after termination of gas sparging as a function of time for the various oil saturations (Volume per cent). The initial liquid volume of the generated foam is 50 cm³ and the maximum volume of generated foam from 1.0 wt% IOS surfactant in the presence of the oil phase using the foam scan is illustrated.

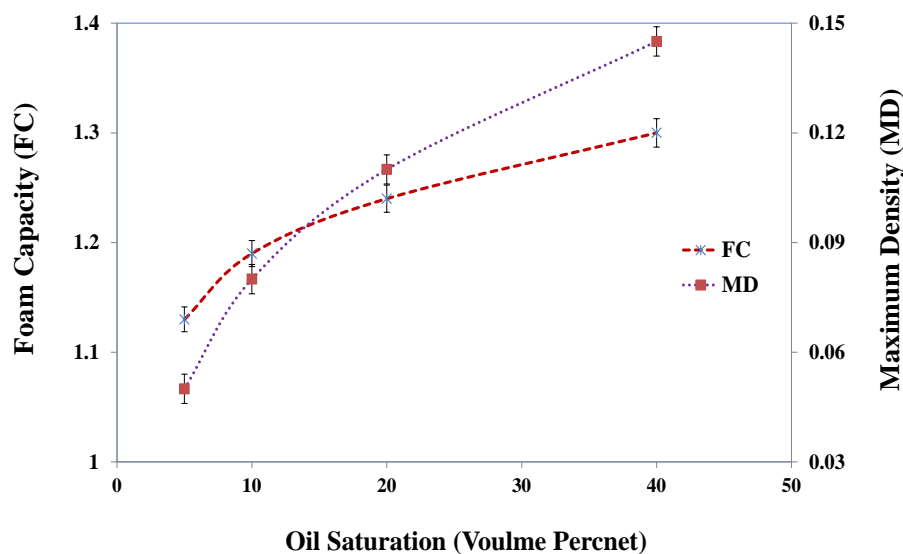


Fig. 4.10: Effect of the different oil saturations on the foam maximum density (MD) and foam capacity (FC) of 1 wt% IOS generated foam.

For the experiment in the presence of oil, the amount of liquid entrained inside the foam structure increased as the oil saturation added (Fig. 4.9). During the foam generation, part of the oil enters into foam lamellae and thickens the plateau borders leading to the transport of oil within foam. This observation can be supported by the variation of FC and MD as shown in Fig. 4.10. A higher liquid volume in the foam is expected to lead to a lower drainage rate for the same surfactant solution in similar experimental conditions. However, as Fig. 4.11 depicts the 1/2-decay time of 1.0 wt% IOS surfactant solution contacting with the range of oil saturation, the foam generated in the presence of a higher oil saturation has a lower half-decay time. Thus, the higher liquid volume in the foam structure in turn led to a larger drainage rate and a faster decline of foam volume compared to the generated foam interacting with the lower oil saturation. This could be due to the penetration of a portion of the oil present in the foam lamellae and plateau borders to the gas-surfactant interface, which leads to the rupture of the foam films. This mechanism may explain the fact that the destabilizing effect of oil increases with the increase of oil saturation under the static foam condition.

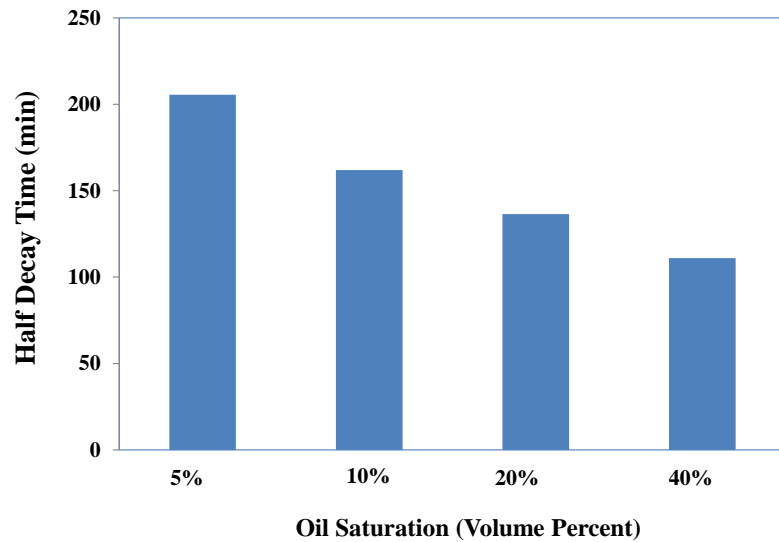


Fig. 4.11: Effect of different levels of oil saturations of n-Hexadecane on the foam half-decay time generated by 1.0 wt% IOS.

Fig. 4.12 displays snapshots of the foam columns generated by 1.0 wt% IOS in the presence of normal hexadecane. The oleic phase was coloured red for the visualization. The image on the left was taken at an early point in the foam decay and the image on the right-hand side was taken at a later point. As can be seen, the created foam can carry a large portion of the oil upward, which results in a relatively uniform distribution of oil in the body of foam. The decay of the foam was continued by a coalescence of bubbles in the middle of the column, causing a local change in the foam texture. The snapshot of the foam column clearly shows that, although foam texture in the latter point of the experiment is coarse, the foam is still stable by holding the oil in the body of foam. Thus, for the IOS foam (in the right-hand image), after gas sparging was terminated, the foam column remained stable for a relatively long time, as can also be inferred by the $t_{1/2}$ in Fig. 4.13.

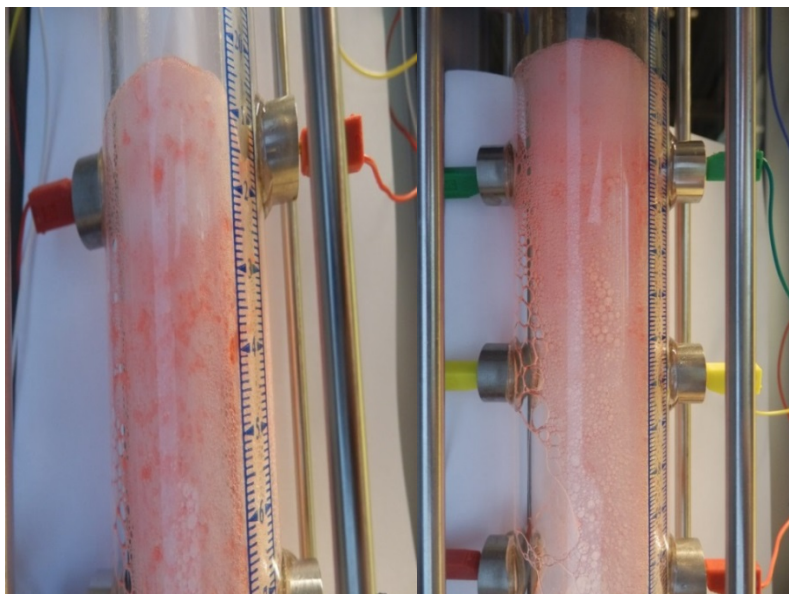


Fig. 4.12: Foam column stabilized by IOS surfactant in the presence of n-hexadecane. The oil phase was coloured red to visualize. The left-hand image was taken at an early time in the foam decay and the right-hand one was taken at a later time. The images confirm that the capability of the generated foam to be tolerant to the oleic phase while drained liquid stayed in the column.

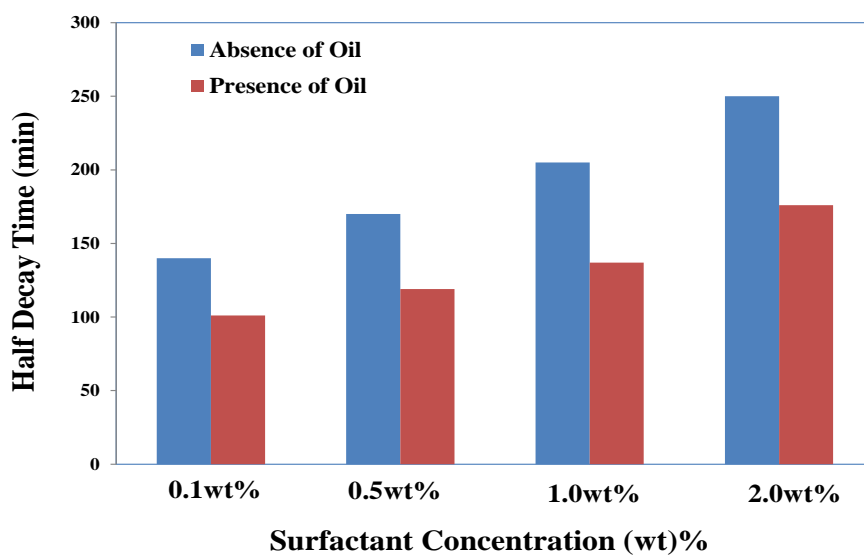


Fig. 4.13: Effect of IOS surfactant concentration on the foam half-decay time in the absence and presence of 5.0 volume per cent of n-Hexadecane.

Fig. 4.13 shows that half-decay time, $t_{1/2}$, in the presence of oil is systematically lower than in the absence of oil, and increases with surfactant concentration. The data in Fig. 4.14 also show the MD coefficient of freshly generated foams as function of surfactant concentration in the absence and presence of n-Hexadecane. As shown, the FC coefficient is larger than unity, even for foam stabilized by a low surfactant concentration of 0.1 wt% (Fig. 4.14). Hence, the

FC. coefficient for foam in the presence of oil is systematically lower than in the absence of oil. The difference in the *FC* coefficients can be attributed to the gas sparging time. Recall, that the *FC* coefficient was defined as a foam volume at the end of gas sparging, divided by the total volume of gas injected. This infers that injection of a larger volume of gas leads to a smaller value of the *FC* coefficient (Simjoo, et al., 2013). Therefore, both coefficients increased with surfactant concentration and oil saturation.

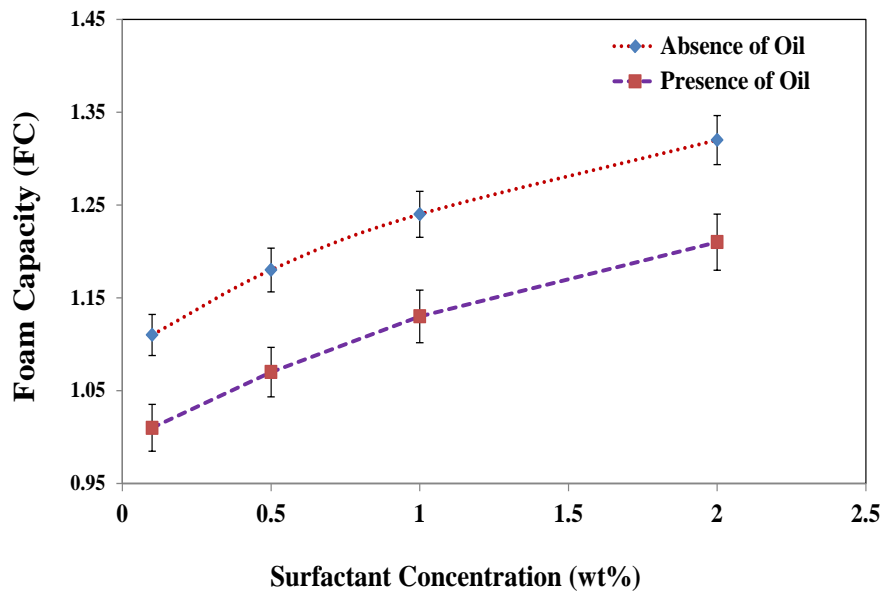


Fig. 4.14: Effect of the IOS surfactant concentration on the foaming capacity (*FC*) in the absence and presence of 5 volume per cent n-Hexadecane. The initial surfactant solution volume of the generated foam is 50 cc and in the case of the presence of n-Hexadecane, oil saturation is 5 volume per cent.

4.5.2.2 Effect of Salinity and Alkalinity

The effect of salinity and alkalinity on the foam stability in the absence of oleic phase is illustrated in Fig. 4.15. Concentrations of salt/alkaline increase up to 5.0 wt%, which is the range of electrolyte concentration obtained from the micro-emulsion phase behaviour study (see Section 4.5.1). From this figure, it can be seen that the addition of salt (NaCl) and alkali (Na₂CO₃) to the IOS foaming system can have an effect on the reduction of foamability and foam stability. Fig. 4.16 shows that the *MD* of the generated foam decreases, as such effects have been associated with the cationic-anionic-type interaction between the anionic moiety of the IOS surfactant and cation ion of the salt and alkali. This type of interaction causes the

screening of the repulsive forces between the ionic head group and a reduction of the surface potential on the gas-liquid interfaces. Consequently, this causes a reduction in the repulsion between the surfactant layers and between the opposing film interfaces, thus, decreasing the double layer repulsion, which, in turn, favours film drainage.

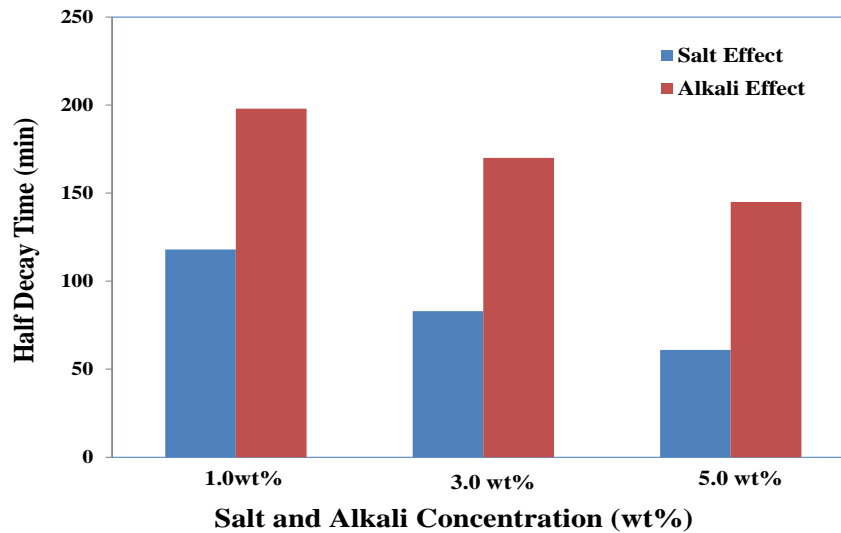


Fig. 4.15: Effect of salt (NaCl) and alkali (Na_2CO_3) concentration on the foam half-decay time of 1.0 wt% IOS surfactant.

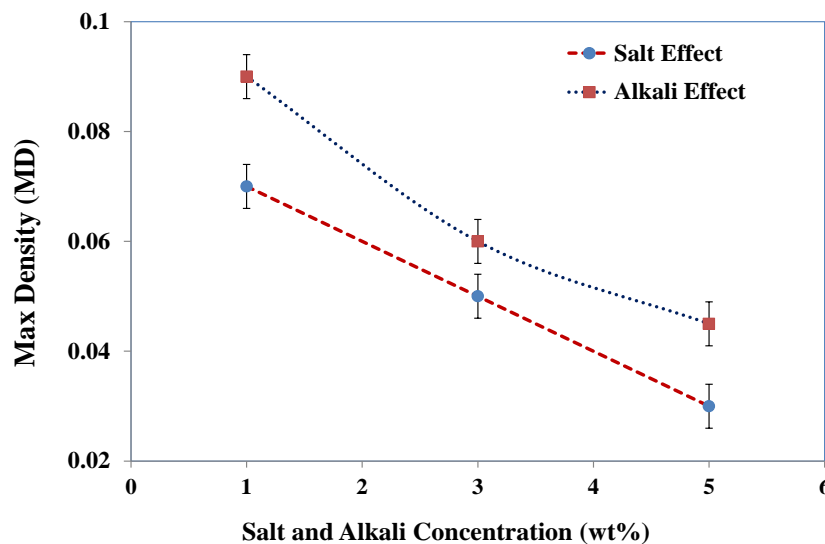


Fig. 4.16: Effect of salt (NaCl) and alkali (Na_2CO_3) concentration on the maximum density (MD) of generated foam with 1.0 wt% IOS surfactant.

4.5.2.3 Effect of *In-Situ* Soap Generation

A surfactant solution, containing 0.5 wt% IOS and 1.0 wt% NaCl with different

concentrations of Na_2CO_3 , was used to study the effect of *in-situ* soap generation on foam drainage. Fig. 4.17 shows the foam volumes versus time for the different alkali concentrations in the aqueous phase contacting with n-Hexadecane containing Decanoic acid. Increasing the alkali concentration from 0.5 wt% to 1.0 wt% resulted in an enhanced foam stability. This can be explained by the fact that a higher alkalinity means more natural surfactant in the system due to *in-situ* soap generation. However, for the surfactant solution containing 2.0 wt% alkali, the drainage rate is larger and the extent of stability is smaller than for a system containing 1.0 wt% alkali. This suggests that the effect of the alkali is reversed due to a large amount of *in-situ* soap generation. This could be due to the fact that the liquid-gas interface is more mobile at a lower surface tension (higher *in-situ* soap), which tends to increase the rate of liquid drained out of the plateau border. This reduction in liquid occurs during the initial liquid holdup as well as during drainage. At lower surface tensions, the capillary suction at the plateau border (which is against gravity) is smaller and, thus, the rate of foam drainage is greater. Thus, uneven thinning and instabilities of the foam film might happen, which will cause acceleration of the film drainage and rupture.

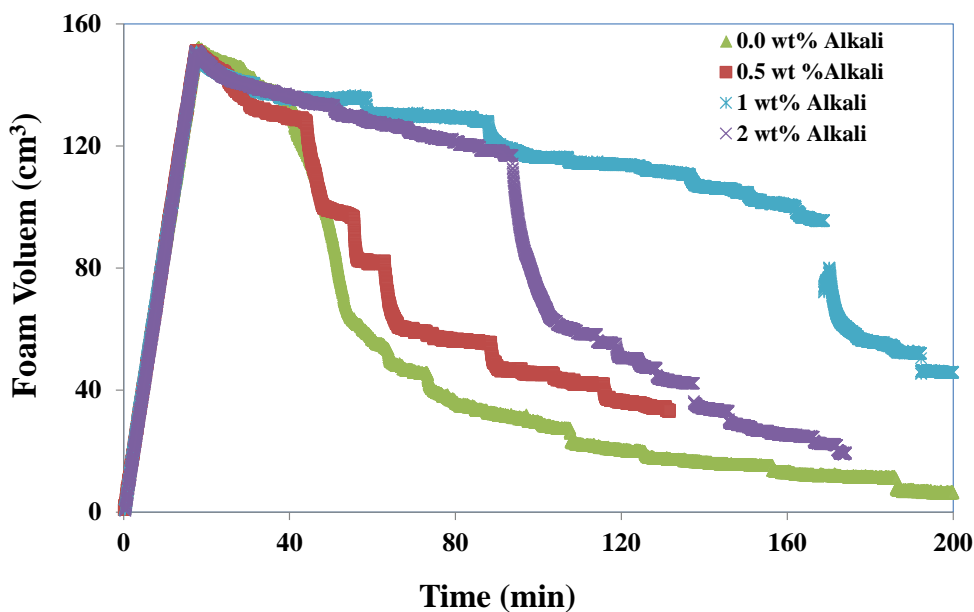


Fig. 4.17: The effect of *in-situ* soap generation and surface tension on the stability of foam is illustrated; as the foam volume change versus time for 0.5 wt% IOS foam contacting n-Hexadecane in the presence of naphthenic acid (Decanoic acid) and different alkali concentration.

The reason for the observed behaviour is not completely clear. This observation could be also interpreted by the rapid spreading of oil droplets that have a low surface tension over the lamella. The spreading oil, augmented the curvature radius of the bubbles and subsequently, lowers the surface elasticity and surface viscosity (Myers, 2005). This can subsequently cause a rupture in the foam structure by creating weak spots. Therefore, the interfacial film loses its foam-stabilizing capability and foam destruction occurs at a significantly low surface tension.

4.5.2.4 Interpretation by Phenomenological Theories

Table 4.6 displays the entering, spreading, and bridging coefficients and the lamella number obtained by combining the measured ST, IFT between, surfactant solution/air, model oil/air, and surfactant solution/model oil. The purpose of obtaining these phenomenological parameters was to gain insight into any correlation between the classical theory and the bulk foam stability in the presence of oil. All the surfactant solutions exhibited a positive entering coefficient ($E > 0$), indicating favourable conditions for n-hexadecane and acidic *n*-hexadecane to enter the gas–water interface. Thus, foam stability in the presence of oil will be determined by the magnitude and the sign of the spreading S and bridging B coefficients (see also Table 4.1). Among the systems studied, systems 1 and 2 provide negative spreading coefficients, but these systems showed the largest positive B coefficients. This indicates that the generated foam should be relatively stable in the presence of n-hexadecane, which is in a good agreement with the observed decay behaviour in Fig. 4.13.

Table 4.6: Entering, spreading, and bridging coefficients and lamella number for different studied systems in presence of n-hexadecane. Surfactant concentration was fixed at 1.0 wt%.

System	Composition	Entering coefficient (mN/m)	Spreading coefficient (mN/m)	Bridging coefficient (mN/m) ²	Lamella number
1	IOS/Hexadecane	22.85	-2.59	784.89	0.422
2	IOS-Alkali/Hexadecane	30.64	-6.48	1106.71	0.304
3	IOS/Acidic Hexadecane	13.62	13.62	440.59	0.812
4	IOS-Alkali/Acidic Hexadecane	10.74	10.74	468.23	4.172

Foam stability can be further examined by comparing the value of the lamella number.

Systems 1 and 2 exhibit a lamella number of smaller than one, which corresponds to type A foam. We recall that a type A foam is stable in the presence of oil with a negative S coefficient (see Table 4.2). However, this is not in line with the calculated E and S coefficients in Table 4.6. It is also not consistent with the observed foam stability in Fig. 4.13, particularly for the case of pure n-hexadecane (without naphthenic acid), which we found to be rather sensitive to the oleic phase. The spreading coefficients calculated for the acidic model oil were positive for systems 3 and 4 regardless of the presence of alkali and *in-situ* soap generation. In theory, in such a situation the oil could spread over the gas-liquid surface and break the foam film, however, according to measured half-decay time, the generated foam was fairly stable (see Fig. 4.13). We recall that, if the spreading coefficient was negative, oil would remain as droplets at the interfacial surfaces, and, thus, attained a necessary condition to stabilize foam.

Systems 3 and 4, in the presence of acidic oil, exhibited positive entering and spreading coefficients, which indicate type C foams. Therefore, for these two systems, foam stability does not seem to be governed by this type of classification. On the other hand, visual inspection of the foam-column experiments, indicated that a foam made using surfactant formulations can emulsify the acidic model oil into Plateau borders of the foam structure. Thus, system 4 exhibited type-B foam behaviour, which indicates that foam stability in the presence of soap generation could be attributed to transport properties of oil droplets within the foam. Type B foams have the capacity to carry more oil than type A or type C foams by transporting emulsified oil droplets inside the foam structure (Vikingstad et al., 2005).

For all IOS foams generated in the presence of oil, the bridging coefficient was high and positive, which implies that the bridging mechanism can trigger a film rupture. Lower magnitude of the entering and bridging coefficients for system 4 than system 3, as presented in Table 4.6, indicates that IOS foam can generate more stable foams when mixed with soap generated by the interaction of alkali and naphthenic acid present in the oleic phase. Thus, we could conclude that a negative spreading coefficient is not a necessary condition for stable foam, and the stability of foam in the presence of oil could be attributed to interfacial properties and oil transport characteristics of the foam plateau-borders and the foam lamellae.

4.6 Conclusions

- An extensive laboratory study of the micro-emulsion phase behaviour, interfacial properties and foam stability characterization was presented to evaluate the properties of chemical slug/drive for the ASF flooding EOR. A surfactant formulation, giving ultralow IFT at the optimum salinity and with fairly good foaming characteristics, was experimentally achieved.
- The micro-emulsion phase behaviour study of various systems in this research demonstrated the impact of the presence of alkalinity, soap generation and surfactant concentration on a range of optimum salinity, oil/water solubilization parameters and IFT values. A water and oil solubilization ratio of 10, as a criterion to get sufficiently low IFT for a high tertiary oil recovery, was met by all the systems containing 1.0 wt% surfactant. However, for the system of 0.5 wt% of surfactant, this criterion was only met for the system interacting with acidic oil, where there is *in-situ* soap generation assisting IFT reduction.
- Foam drainage with and without the presence of the oleic phase was influenced by the physio-chemical properties of surfactant solutions as well as by the tolerance of the generated foams to capillary suction pressure and bubble coalescence. Our results showed that although the amount of liquid entrained inside the foam structure raised as the oil saturation added, the presence of higher oil saturation increases the coarsening rate of foams.
- The effect of alkalinity on lowering foam stability could be attributed either to screening the repulsive forces between the ionic head group resulting from cationic-anionic-type interaction and decreasing double layer repulsion, or to the change in the micelle structure from spherical micelles to other more complex structures.
- A large amount of *in-situ* soap generation resulted in diminishing foam stability. This observation could be interpreted by the rapid spreading of oil droplets that have a low surface tension over the lamella. The spreading oil, by augmenting the curvature radius of the bubbles, diminishes the surface elasticity and surface viscosity. This

subsequently can cause a rupture in the foam structure by creating weak spots over the interfacial lamella film.

- Less foam stability at significantly low IFT between the aqueous phase and oleic phase can also be explained by the fact that the gas-liquid interface is more mobile at a lower surface tension, which tends to increase the rate of liquid drained out of the plateau border. At lower surface tensions, the capillary suction at the plateau border (which is against gravity) is smaller and, therefore, the rate of foam drainage is greater. Thus, uneven thinning and instabilities of the film might happen, which will cause acceleration of film drainage and lamellar rupture.
- The classical phenomenological parameters, such as spreading and entering coefficients, have been used with some success and similarities in the current trend of research; however, foam performance by these parameters does not correlate with the foam stability to oil for most of the experiments.

Chapter 5

Optimal Alkali/Surfactant/Foam Flooding Process for EOR:A CT Scan Study

5.1 Abstract

Strong foam can be generated in porous media containing oil, resulting in incremental oil recovery. A large fraction of oil recovered by foam flooding, forms an oil-in-water emulsion so that costly methods may need to be used to separate the oil. Moreover, strong foam could create a large pressure gradient, which could cause fractures in the reservoir. A novel Alkali-Surfactant-Foam (ASF) flooding process was recently introduced for EOR from water-flooded reservoirs. The ASF process involves the use of an Alkali-Surfactant (AS) solution as a slug to mobilize the remaining oil after water flooding, and foam as a drive to displace the mobilized oil to the production well.

In this study, a blend of two types of anionic surfactant formulations was formulated for slug and drive: (a) IOS, for achieving ultra-low IFT, and (b) AOS for generating a strong foam. Prior to the oil recovery experiments, foam mobility reduction behaviour in the absence of the oleic phase was investigated for both the transient and steady-state flow regimes. Experiments

The content described in this chapter is submitted as: Hosseini-Nasab et al. (2017) "Optimal Alkaline-Surfactant-Foam Flooding Process for Enhanced Oil Recovery: A CT Scan Study", Journal of Energy and Fuels, ACS.

were performed using Bentheimer sandstone cores, during which pressure drop measurements were carried out to determine the ability of foam to reduce the total mobility. X-ray CT images were taken during foam generation to find out the stability of the advancing front of foam propagation and to map the gas saturation. Then, the proposed ASF strategy for enhanced oil recovery was tested through the co-injection of immiscible nitrogen gas and slug/drive surfactant solutions with three different formulation properties in terms of IFT reduction and foaming strength capability. The performance of this ASF slug/drive chemical formulation was evaluated by a core-flood test on Bentheimer sandstone rock with the aid of X-ray computed tomography. The discovered optimal formulation contains a foaming agent surfactant, a low IFT surfactant, and a co-solvent, which has a high foam stability and a considerably low IFT (1.6×10^{-2} mN/m). Co-injection resulted in gave higher oil recovery and much less MRF than the same process with only using a foaming agent. The oil displacement experiment revealed that co-injection of gas with a blend of surfactants, containing a co-solvent, can recover a significant amount of oil (33% OIIP) over water-flooded residual oil, with larger amounts of clean oil and less emulsion.

5.2 Introduction

Gas injection EOR suffers from poor sweep efficiency due to three main reasons: 1) gas segregation and gravity override due to a lower density of gas than oil and water phases, 2) viscous fingering due to a high mobility ratio between gas and oil or water, 3) gas channelling through high-permeability zones in heterogeneous and layered reservoirs (Lake et al., 2014). Foam diminishes gas mobility leading to a substantial rise of the pressure gradient. Foam improves volumetric sweep efficiency by a significant reduction of gas mobility: it provides a favourable mobility ratio between drive (gas) and displaced (oil and water) fluids, and contacts a larger fraction of the reservoir to mitigate the effect of heterogeneity, gas segregation and viscous instability (Rossen, 1996; Schramm & Smith, 1996). Foam for EOR is implemented either by co-injection of gas and surfactant or by surfactant alternating gas (SAG) injection. Gas and surfactant co-injection leads to far larger mobility reduction than SAG injection (Huh & Handy, 1989).

Foam has also been identified as a suitable alternative to polymer in the ASP flooding EOR process for reservoir formation with a low permeability and a high heterogeneity. ASF flooding is a new EOR method, which applies foam as a mobility control agent instead of polymer (Guo et al., 2012; Li et al., 2012). Moreover, the presence of Alkaline-Surfactant (AS) slug creates a base (high pH) environment and *in-situ* soap generation, which enables a significant reduction of IFT and surfactant adsorption (Kang et al., 2010; Yuqiang et al., 2008). IFT reduction during foam floods leads to an increase of the capillary number, thus improving microscopic displacement of oil (Guo et al., 2012). Similar processes to ASF EOR have been reported by others under different terminology, for instance Low Tension Gas (LTG) and Alkali-Surfactant Gas (ASG) flooding (Wu et al., 2010, Szlendak et al., 2013; Tang et al., 2014). Advantages of foam over polymers include the fact that foam can divert flow from high permeable regions to low permeable zones, thus leading to improved sweep efficiency and higher oil recovery factors (Srivastava et al., 2010). This is due to the fact that foam is stronger in high permeability zones than in low permeability oil-bearing zones (Li et al., 2010; Ma et al., 2012). For ASF flooding in water-flooded reservoirs, foam can divert AS slug to low permeability layers, thus mobilizing trapped residual oil by lowering IFT, and by reducing capillary forces.

The efficiency of immiscible foam flooding as an EOR method is limited. Although strong foam can be generated in the presence of oil, incremental oil recovery by the foam flooding on a tertiary recovery mode does not exceed 30% of OIIP in a reasonable number of pore volume of foam injection. A large fraction of oil recovered by foam flooding forms a stable oil-in-water emulsion, so that separating the oil may require costly methods. This study investigates the impact of IFT reduction, foam mobility reduction and the synergetic effect of these two factors on the performance of foam flooding. Our aim is to shed more light into foam behaviour, especially in terms of microscopic displacement of trapped oil and volumetric sweep efficiency, which is of great importance. To achieve this, the formulation of a foaming agent capable of producing ultra-low IFT between oil and water, and simultaneously able to generate a stable foam, has been examined in detail.

The structure of this chapter is as follows. First, we present the experimental materials and

methods including the core-flooding procedure, CT scan setting and processing. The chapter proceeds with the results and the discussions of foam flooding for chemical formulations in sandstone porous media without the oleic phase. Next, the results of the core-flooding experiments for enhanced oil recovery (EOR) are presented and discussed. Finally, the main conclusions are drawn.

5.3 Experimental Description

5.3.1 Materials

Brine was prepared by adding sodium chloride (NaCl, Merck) and sodium carbonate (Na_2CO_3), both at a fixed concentration of 1.0 wt% to de-mineralized water. Density and viscosity of brine thus prepared at 25° C were $1.07 \pm 0.01 \text{ g/cm}^3$ and $1.10 \pm 0.01 \text{ cP}$, respectively. The used surfactants were AOS, and IOS with a long carbon chain. AOS and IOS surfactants were supplied as a liquid, with 40 wt% and 19 wt% active content respectively, and they were used as received without further treatment. The co-solvent was a sec-butyl alcohol (SBA, Merck, 99% pure). The CMC of the AOS and IOS solutions in the presence of 2.5 wt% NaCl were $3.5 \times 10^{-3} \text{ wt\%}$, and $5 \times 10^{-3} \text{ wt\%}$, respectively. Normal hexadecane (n-C16, Sigma-Aldrich) with a purity larger than 99 wt% was used as model oil. Viscosity and density of n-hexadecane at 25°C were found to be $3.2 \pm 0.01 \text{ cP}$ and $0.78 \pm 0.01 \text{ g/cm}^3$, respectively. Nitrogen gas used with a purity of 99.98% for foam generation. The surfactant viscosity was 1.08 mPa.s. The properties of Bentheimer core are summarized in Table 5.1.

Table 5.1: Physical properties of the core samples used for core-flood test

Core sample	Bentheimer sandstone
Porosity (%)	23.0 ± 0.1
Diameter (cm)	3.8 ± 0.1
Length (cm)	17.0 ± 0.1
Pore volume (cm^3)	46.5 ± 0.5
Brine permeability (Darcy)	2.5 ± 0.1
Quartz content of rock (wt%)	92.0 ± 1.0

5.3.2 Core-Flow Experimental Setup

The set-up used to conduct the core-flooding experiments is shown schematically in Fig. 5.1. It consisted of a core-holder made of polymer (PolyEther-Ether-Ketone), named PEEK, with an internal diameter of 5cm and a wall thickness of 2.0 cm. The core-holder was mounted vertically at the edge of the couch of the CT scanner. The cores, using a coring tool, were drilled from Bentheimer sandstone block and CT scanned to detect the presence of any anomalies, such as cracks or uncharted elements. Core samples with a diameter of 4.0 ± 0.1 cm were coated with a thin layer of epoxy resin and the resin was left to harden before the core was placed in the core-holder. Before hardening, the epoxy resin penetrating about 2.0 ± 0.5 mm into the pores of the rock surface, the effective diameter of the core from the CT scan image was estimated to be 3.8 ± 0.1 cm.

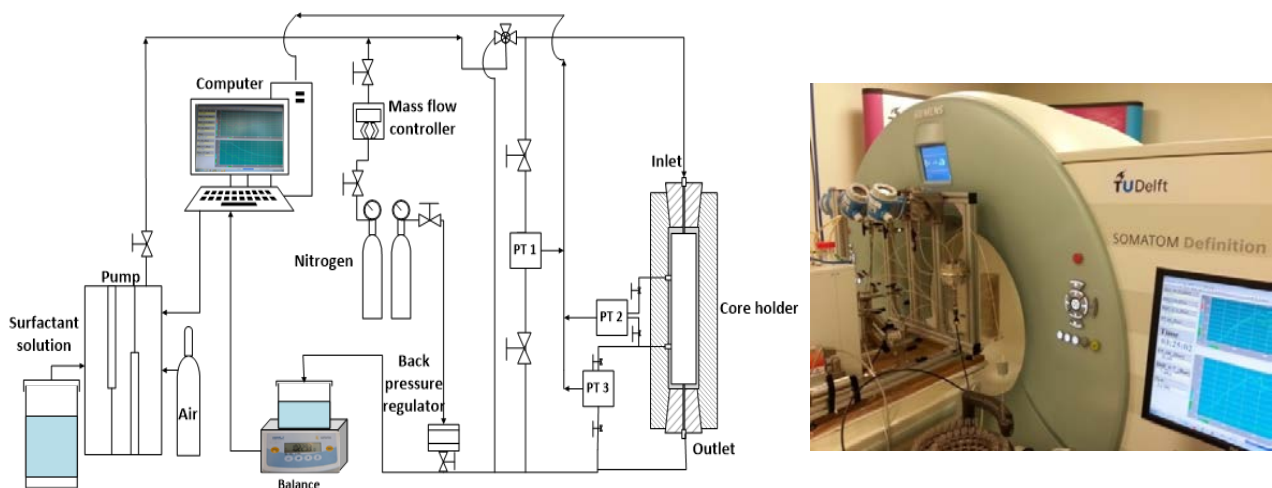


Fig. 5.1: Schematic overview of the core-flooding set-up for foam flow and oil displacement experiment used in CT scan visualization. The core-holder was placed vertically on the table of CT scanner.

Quizix QX-500 pumps were used to inject the water phase (i.e. brine and surfactant solution). A Teledyne ISCO pump, capable of injecting at low injection rates (as low as 0.001 cm^3/min), was used to inject oil. Nitrogen gas was supplied by a cylinder, connected to the inlet of core-holder, through a mass flow controller (MFC). At the core outlet, a Mite Mite back-pressure regulator (BPR) was used to keep pressure constant, and a fraction collector (Frac920AKTA) was used to monitor the volumes of the effluents. Three holes, drilled along the length of the core through the glue layer into the rock surface, were used for measuring

sectional pressure drops. Three differential pressure transducers were connected to record overall and sectional pressure drop over the core segments with increasing length from the core inlet (section 1: 11 cm, section 2: 4.3 cm). Two pressure transducers were used to monitor the inlet pressure and outlet (back) pressures.

5.3.3 CT Scan Setting and Processing

X-ray CT scans of the core were taken during cote-floods to evaluate the front stability of foam propagation, quantifying the gas saturation and the residual liquid saturation in the presence of foam. X-ray CT images presented in this study were obtained using the medical CT scanner, SOMATOM definition (see Fig. 5.1). The CT images were employed to determine the *in-situ* saturations of the aqueous, oleic and gas phases. CT scanning is based on the attenuation of X-ray beams through the object being scanned. The attenuation coefficient is different for the local physical properties and concentrations of the materials scanned. CT scanners provide image matrices where the attenuation coefficients are expressed in Hounsfield Units (CT numbers), defined as:

$$CT = 1000 \left(\frac{\mu}{\mu_w} - 1 \right) \quad (5-1)$$

where CT is the CT-number value in Hounsfield unit, μ_w is the X-ray attenuation coefficient of water in a unit of m^{-1} and μ is the X-ray linear attenuation coefficient of the sample in a unit of m^{-1} . The settings used for CT images in the experiments are listed in Table 5.2. The X-ray tube of the CT scanner operated at a current of 250 mA and a voltage of 140 kV. CT images were taken in the vertical direction parallel to the core axis. The CT scanner took 4 images at each scan vertically from top to bottom of the core with a slice thickness of 3 mm. The sequential scan mode was used for imaging acquisition, as it provides a low noise-to-signal ratio. The spatial resolution of CT was based on the voxel volume that was $0.195 \times 0.195 \times 0.6$ mm. The highest resolution of the image display was 512×512 pixels.

Table 5.2: Setting parameters for the CT Scan measurements

Parameter (units)	Value/Condition
Tube current (mA)	250
Tube voltage (kV)	140
Pixel(Voxel) size (mm×mm)	0.3×0.3
Slice thickness (mm)	3.0
Filter	B40-medium
Scan mode	Sequential

To calculate rock porosity and fluid saturations inside the rock, we used the method presented in the work of Rangel-German et al. (1999). The porosity ϕ of the core samples can be calculated by using CT images of dry core and fully brine saturated core and the CT number (Hounsfield Unit) values of brine and air,

$$\phi = \frac{CT_{wet} - CT_{dry}}{CT_w - CT_g} \quad (5-2)$$

where CT_{wet} , CT_{dry} , CT_w and CT_g are respectively the measured attenuation coefficients for fully water-saturated core, dry core, water and air. For the drainage process (oil injection) and the imbibition (water flooding) experiments, due to combined effects of rock, the water phase and the oleic phase, one can write for each voxel of rock sample as the following equation to describe the total X-ray attenuations:

$$CT_{wet} \times S_w + CT_{oil}S_o = CT_{wo} \quad (5-3)$$

$$(CT_{oil} - CT_{wet}) = (CT_{wet} - CT_{dry}) \left(\frac{CT_o - CT_g}{CT_w - CT_g} - 1 \right) \quad (5-4)$$

By combining the Eqs. of (5-3) and (5-4), oil *in-situ* saturation can be calculated as follow:

$$S_o = \frac{1}{\phi} \frac{CT - CT_{wet}}{CT_o - CT_w} \quad (5-5)$$

During foam flooding, the attenuation coefficient of the core plug is a combination of the gas phase and the liquid phase attenuation coefficients. To describe the *in-situ* distribution of

gas-liquid systems, the gas saturation inside the core can be calculated from the CT images by the following equation:

$$S_{gas} = \frac{CT_{pre-flush} - CT_{foam}}{CT_{pre-flush} - CT_{dry}} \quad (5-6)$$

where subscripts dry, pre-flush and foam stand respectively for the dry core, core at the end of surfactant pre-flush before foam injection, and the core with foam flow.

5.3.4 Experimental Procedure

Core-flooding was performed as follows. First, core was evacuated for roughly 2 hours and then flushed with CO₂ with 5.0 bar back-pressure to remove all air from the porous medium. Next, several pore volumes of brine were injected into the dry core while varying back pressure: the back of the core-outlet was first kept at 1.0 bar up to water break-through, and then it was increased to 25 bars to dissolve any CO₂ remaining in the core and to ensure 100% saturation of the core with brine. Absolute permeability of the sandstone core was then measured by the standard method. For the experiments in the absence of oil, a surfactant pre-flush was done prior to foam flooding. For experiments involving an EOR process, oil injection followed by water flooding and, subsequently, pre-flush of surfactant solution of the foaming agent were undertaken before foam flooding. Table 5.3 summarizes the procedures used for the experiments in the absence and presence of oil.

Table 5.3: Sequence and conditions of injection step used for the core-flooding experiment

Injection step sequence	FlowRate (cm ³ /min)	Back-Pressure (bar)	Injection Direction
To evaluate the foam strength			
CO ₂ flushing to remove air	>20	5	Downward
Core saturation with brine	1.0-6.0	25	Upward
Surfactant preflush	1	30	Upward
Foam flooding (co-injection)	0.55	30	Downward
For EOR process			
CO ₂ flushing to remove air	>20	5	Downward
Core saturation with brine	1.0-6.0	25	Upward
Oil injection (drainage)	0.5	5	Downward
Bump flood (Oil)	8.0		
Water flooding (imbibition)	0.5	5	Upward
Bump flood (Brine)	5.0		
Surfactant preflush	1	30	Upward
Foam flooding (co-injection)	0.6	30	Downward

The first objective of the series of experiments was to examine the capability of the three selected surfactant solution formulations (see Table 5.4) to generate a stable foam. The chemical formulations, used for the foam flooding experiment in absence of the oleic phase and for EOR experiments, are presented in Table 5.4. For each alkali-surfactant (AS) solution, core-flood experiments consisted of a co-injection of AS solution and N₂ in the absence of oil phase at room temperature. A surfactant solution was first pre-flushed to quench the surfactant adsorption of the core-plug to reduce the effect of surfactant adsorption during foam flooding.

Table 5.4: Surfactant formulations used in foam strength test and oil displacement experiments

Exp.	Type of Exp.	Surfactant Formulation	Electrolyte composition	Viscosity (cP)	Density (g/cm ³)	IFT with hexadecane (mN/m)
AS1	Foam flood	0.5 wt % AOS	2 wt% NaCl 1 wt % Na ₂ CO ₃	1.12	1.05	1.56 × 10 ⁰
AS2	ASF flood	0.2 wt% AOS + 0.6 wt% IOS	2 wt% NaCl 1 wt % Na ₂ CO ₃	1.22	1.08	3.42 × 10 ⁻¹
AS3	ASF flood	0.2 wt% AOS +0.6 wt% IOS +0.4 wt% Co-solvent	2 wt% NaCl 1 wt % Na ₂ CO ₃	1.18	1.10	1.17 × 10 ⁻²

In EOR processes, the produced oil was collected in the grade test tubes and oil recovery calculations were executed by a material balance of the fluids inside the core and the effluents at outlet tubes. Foam flooding experiments were carried out by a co-injecting nitrogen and surfactant solution, while keeping the back-pressure at 30 bars. N₂ was injected from a cylinder at 50 bar to the mass-flow controller. The experiment was conducted under a back-pressure of 30 bar to minimize gas compressibility effects. Foam was generated by co-injecting the N₂ and surfactant solution from the top of the sandstone core at a fixed total flow rate of 0.6 cm³/min. This flow rate is equivalent to a superficial velocity of 0.78 m/day [2.54 ft/day]. The resistance to gas flow during foam generation and coalescence in the transient and steady state conditions was evaluated macroscopically using the foam Mobility Reduction Factor (MRF). Pressures of the generated foam and reference condition were measured to define $MRF = \Delta P_{foam} / \Delta P_{ref}$ as the ratio of pressure drops for foam flooding to single phase water injection at the same flow-rate. Foam floods were all carried out at a foam quality (i.e. inlet gas fractional flow) of 80%.

5.4 Results and Discussion

5.4.1 Foam flow in porous media in absence of oil

a) **Mobility Reduction Factor (MRF)**. Fig. 5.2 to Fig. 5.4 show overall and sectional MRF vs. numbers of PV obtained from the co-injection of N₂ and three formulates AS solutions along the core as a function of a number of co-injected pore volumes. MRFs for three cases after approximately 2 PV injections reach the plateau after 894, 567 and 282 with only a slight increase in the continuation of the test.

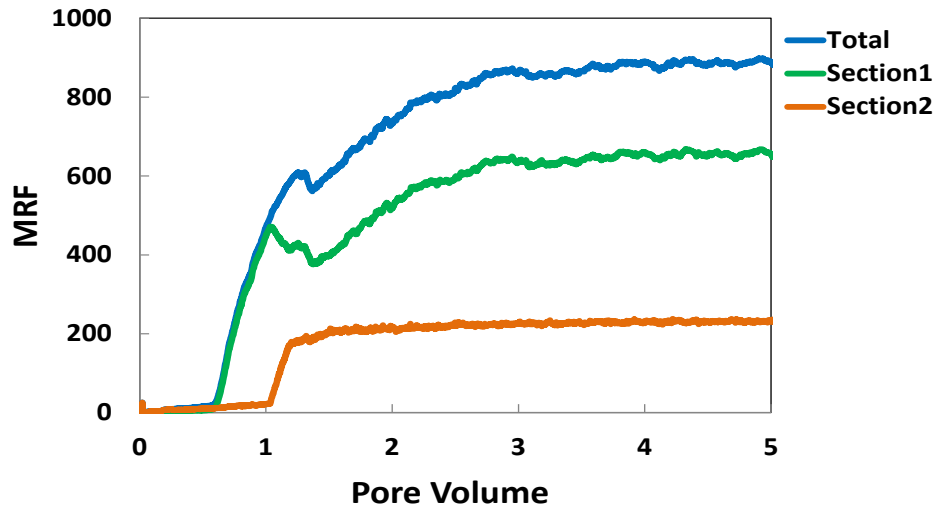


Fig. 5.2: Total and sectional MRF results along the core from the experiment of co-injection of N₂ and AS1 surfactant in the absence of oil phase. Foam quality 80% and total velocity of 2.54 ft/day. (section 1: 11cm, section 2: 4.3cm)

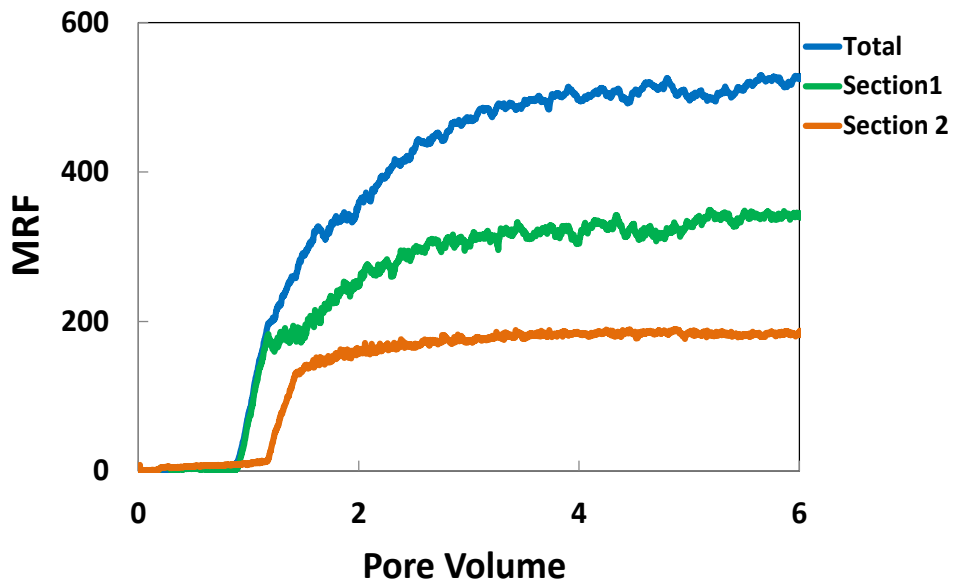


Fig. 5.3: Total and sectional MRF results along the core from the experiment of co-injection of N₂ and AS2 surfactant in the absence of oil phase. Foam quality 80% and total velocity of 2.54 ft/day. (section 1: 11cm, section 2: 4.3cm)

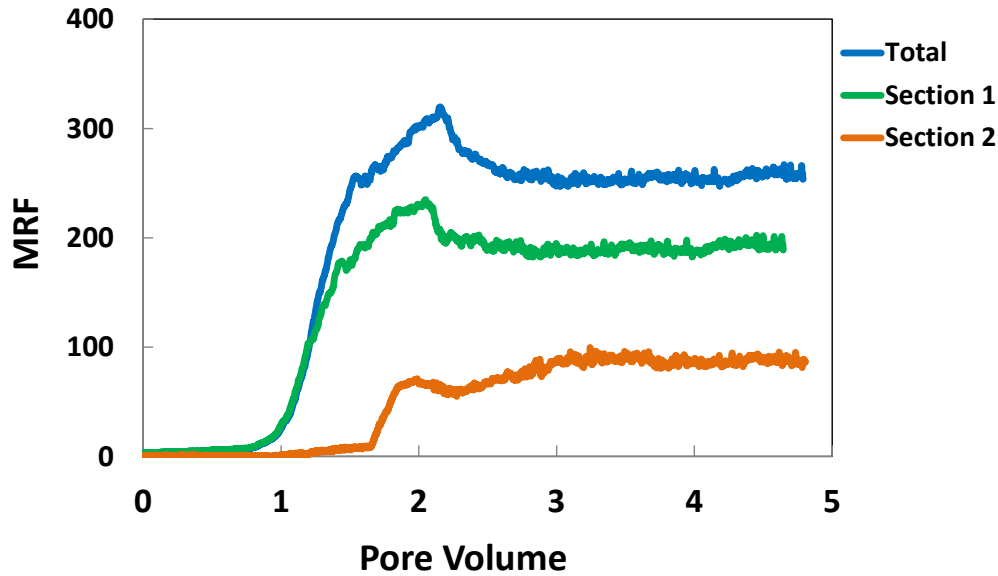


Fig. 5.4: Total and sectional MRF results along the core from the experiment of co-injection of N_2 and AS3 surfactant in the absence of oil phase. Foam quality 80% and total velocity of 2.54 ft/day. (section 1: 11cm, section 2: 4.3cm)

In all experiments it was found that about one pore volume in total was needed before strong foam was generated. At early injection times, coarse foam generation occurred, which provide only small pressure drops. Delay in foam generation and an increase of MRF can be attributed to competition between foam creation and destruction along the pores before reaching the minimum pressure gradient to create strong foam (Rossen & Gauglitz, 1990; Tanzil et al., 2002). Comparison of steady state MRFs in Fig. 5.2 and Fig. 5.3 indicates a much lower effect of IOS on the foam strength than AOS. Results also show that the lowest IFT formulation (AS3) enables foam generation with a moderately high strength. By having evidence of the lowest IFT formulation to create a fairly stable foam in the absence of oil, this formulation (AS3) was chosen for the CT scan analysis.

b) CT scans and saturation profiles. For the CT Scan study, the experiment with the AS3 chemical formulation with the smallest MRF and a moderate strength of foam was chosen to investigate the stability of foam front propagation and the evolution of gas saturation. Fig. 5.5 shows CT images taken during foam flooding in Bentheimer sandstone previously saturated with surfactant solution. The light blue colour indicates a core fully saturated with a surfactant solution, and the change to dark blue corresponds to the foam phase. Images clearly show the advancement of foam from the top to the bottom of the core. The number below each image

represents the number of foam pore volumes injected (elapsed time). Images show that foam displaces surfactant solution in a piston-like fashion, indicating that more viscous fluid (i.e. foam) is displacing less viscous fluid in a stable manner. Colour changes from light blue to dark blue from the left to right gives evidence of the increase of gas saturation behind the front. There is a small region near the inlet face with a relatively higher intensity of light blue colour, which remained for a while, indicating higher water saturation compared to the rest of the core. Discontinuity of capillary pressure at the inlet face results in the retention of the water phase, which is the wetting phase with respect to sandstone rock, at the core inlet.

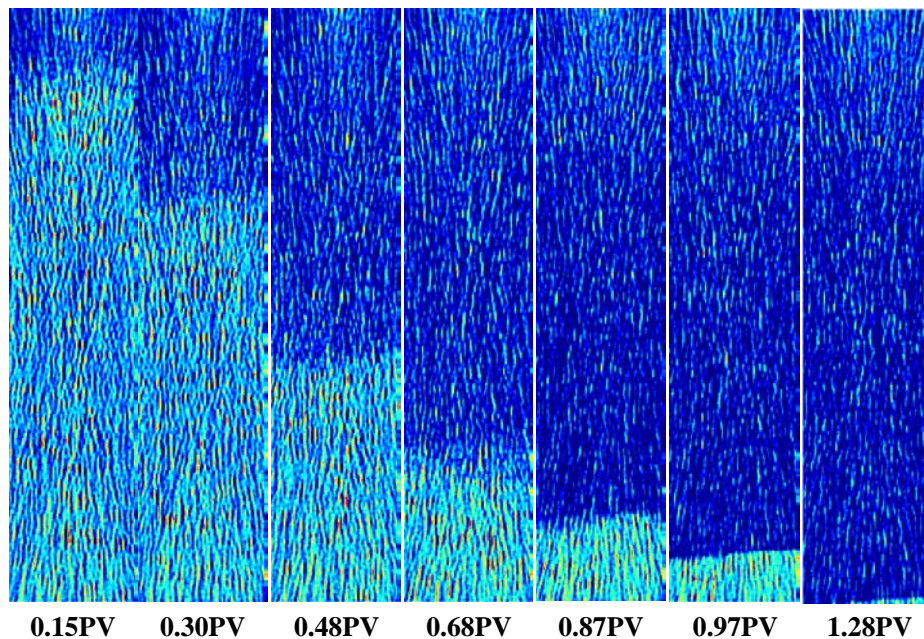


Fig. 5.5: CT images obtained during co-injection of N_2 and of ASF chemical agent (AS3). Foam flow was studied in a single core of Bentheimer sandstone. First sharp foam front advances through the core after about 0.8 PV injection. Sharp front of generated foam is evident of stable foam displacement in the core.

For further analysis, we plotted gas saturation profiles, obtained by the Eq. (5–6) by combining the CT scans for dry core, core fully saturated with surfactant solution and the core during foam injection. Gas saturation was obtained by the arithmetic average of every horizontal line of the saturation voxel throughout one CT image slice. Gas saturation for foam flooding with very low-IFT surfactant formulation (AS3) is plotted in Fig. 5.6 against different co-injection pore volumes.

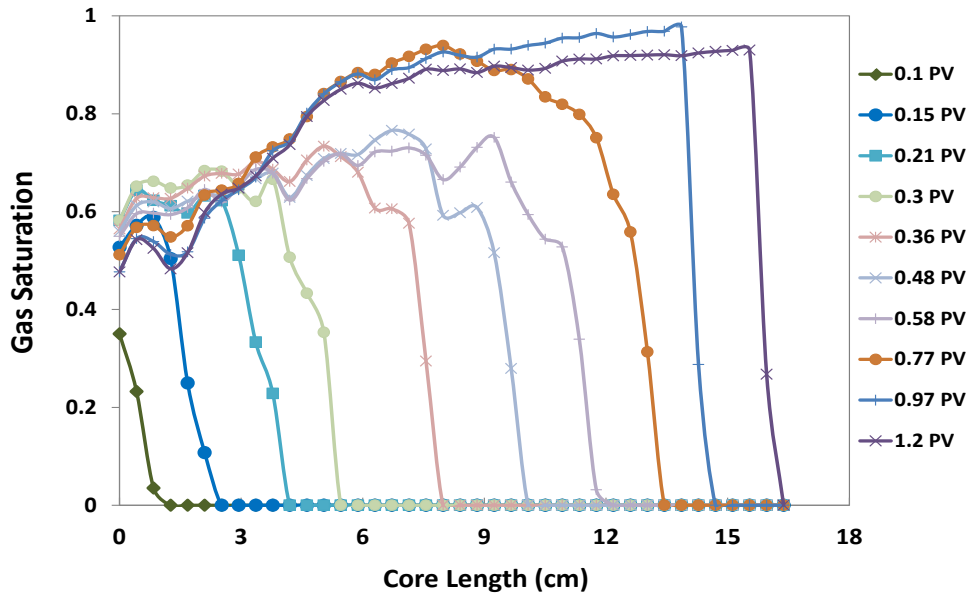


Fig. 5.6: Gas saturation profiles taken at every vertical position throughout the core before and after foam breakthrough obtained from the CT images shown in Fig. 5.5. Foam quality at inlet face of the core was 80%. A rapid in-situ foam generation and fairly piston-like front for the gas saturation propagation were observed.

Foam saturation profiles consist of a downward-concave shape and a horizontal part. At early times, for instance, 0.1 PV, gas saturation is below 0.40, then rises and reaches the average value of approximately 0.65. A progression of gas saturation curves illustrates a typical Buckley-Leverett front shape, including the effect of gas compressibility and capillarity. The inlet-effect, with a high water saturation near the core inlet over a length of approximately 2.5 cm, was observed and persisted over the entire duration of the experiment. It can be explained by the discontinuity of capillary pressure at the injection face of the core, due to the fact that the foam phase, including a high fraction of the non-wetting phase (gas), displaces the wetting phase (surfactant solution). This creates a large capillary pressure contrast as before the inlet, that is outside of porous media, where the capillarity is zero.

5.4.2 Displacement of oil by foam

5.4.2.1 Drainage and Imbibition

Primary drainage and imbibition are reported here, prior to discussing oil recovery by foam. Oil was injected into the core, previously fully saturated with brine at velocity of 2.24 ft/day, until no water was flowing out of the system. Then, oil saturation was measured, either by analysing CT scan images, or by measuring volume of the effluents. For the first and

second experiment (AS1 and AS2), the saturation was determined from the mass balance calculation of the measured effluent volumes of oil and water. CT scans of the cores were made throughout the whole experiments at time intervals for the third experiment (AS3), to determine precisely the *in-situ* saturations of water and oil, in addition to mass balance calculation of the effluent. The overall and sectional pressure drops along the core during drainage are plotted on Fig. 5.7. When oil was introduced to the inlet of the core, pressure drops abruptly raised. The sharp increase represents a characteristic of entry capillary pressure between water and oil according to the Young- Laplace equation ($P_{c_in} = 2\sigma_{ow} \cos(\theta) / r$).

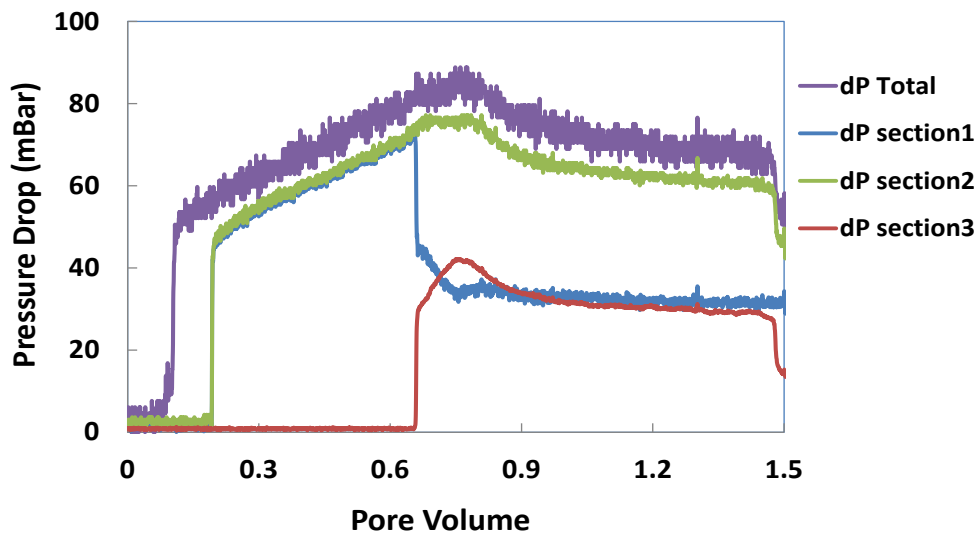


Fig. 5.7: Pressure drop profiles during primary drainage over the core and different section of the core (section 1: 11cm, section 2: 4.3cm and section 3: 4.75cm). Oil was injected at $0.5 \text{ cm}^3/\text{min}$ under gravity stable conditions. The initial jump in the pressure drop profiles corresponds to the entry capillary pressure.

Fig. 5.8 shows a series of CT scan images taken at different times during primary drainage. The blue colour corresponds to a core fully saturated with brine, while the light green colour corresponds to the presence of the oleic phase. Oil is injected from top to bottom of the core, so that the colour of the image varies from blue to light green from the left to right. The displacement is gravity-stable with a rather sharp front between the oil and water phase. The CT images were further analysed to quantify the oil saturation map at different PV injected. Oil saturation was calculated from the CT images according to the Eq. (5–5), by combining the images for the dry core, the fully brine-saturated core, the bulk attenuation coefficient of oil and the brine.

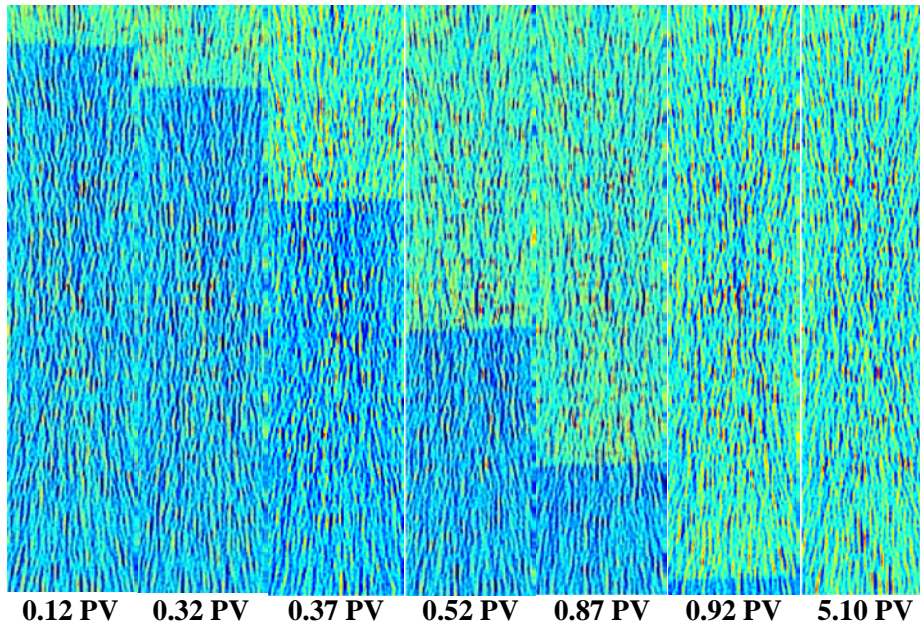


Fig. 5.8: Displacement profile during primary drainage (oil injection) with injection direction from top to bottom. Water phase (blue colour) was displaced by oil (light green).

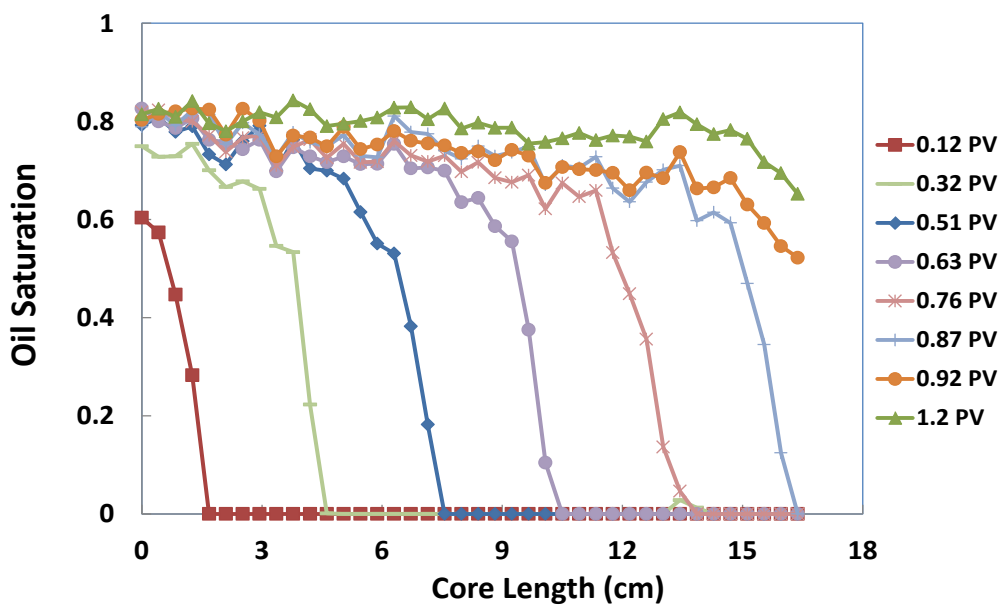


Fig. 5.9: Oil saturation profile for oil injection as a primary drainage obtained from the corresponding CT images shown in Fig. 5.8. Oil was injected from the top of the core, which is located on the left side of the figure. The average oil saturation at the end of primary drainage was 0.80 ± 0.02 .

Changes in oil saturation, plotted in Fig. 5.9, are in a piston-like profile and are consistent with a Buckley-Leverett theory for two phase flow (Willhite, 1986). When no more water was observed at the outlet, bump flood oil injection at a flow rate of $8 \text{ cm}^3/\text{min}$ was performed to reach connate water saturation. At the end of the primary drainage, the average oil saturation in

the core was $S_o = 0.81 \pm 0.02$ and thus, connate water saturation was $S_{wc} = 0.19 \pm 0.02$ (see Fig. 5.9). After drainage, the core was subjected to water flooding (imbibition) at a flow-rate of $0.5 \text{ cm}^3/\text{min}$, equal to the interstitial velocity of 2.24 ft/day , till no more oil was produced from the core. The sectional pressure drops and the total pressure drop over the core during water flooding are shown in Fig. 5.10.

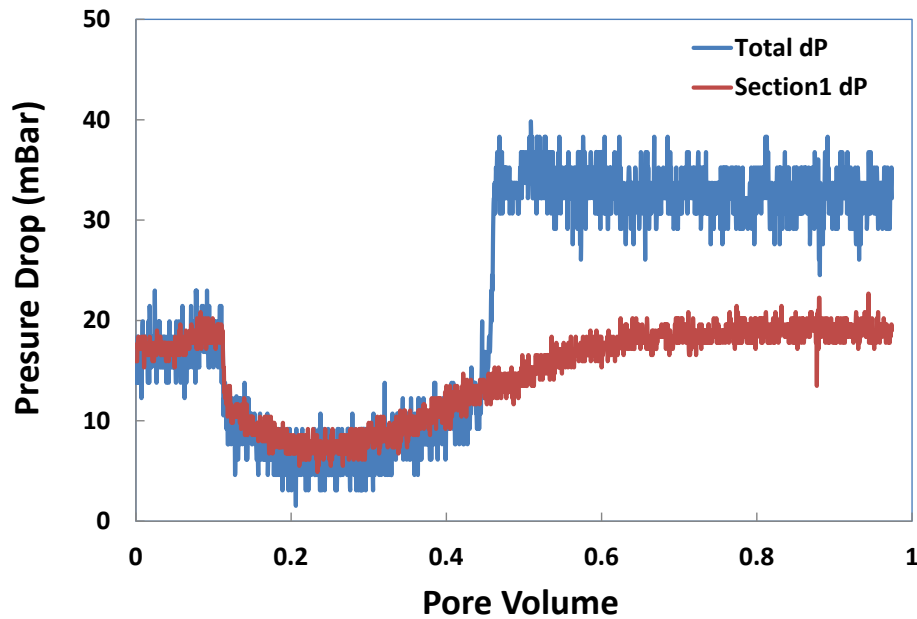


Fig. 5.10: Total and sectional pressure drop profile during water flooding at $0.5 \text{ cm}^3/\text{min}$ during the first two pore volumes injected. Water breakthrough coincides with the time at which pressure drop obtains a maximum value.

As imbibition was introduced into the core inlet, the pressure drop decreased indicating the capillary pressure between the two phases declined, due to the presence wetting phase (water) at the front. Pressure drop behaviour represents the characteristic of imbibition in a water flooding process with an early water breakthrough (BT) at 0.38 PV , accompanied by a long tailing oil production as the total pressure drop gradually levels off to a plateau. This is consistent with CT images of this test shown in Fig. 5.11, where the BT time close to 0.33 PV was determined.

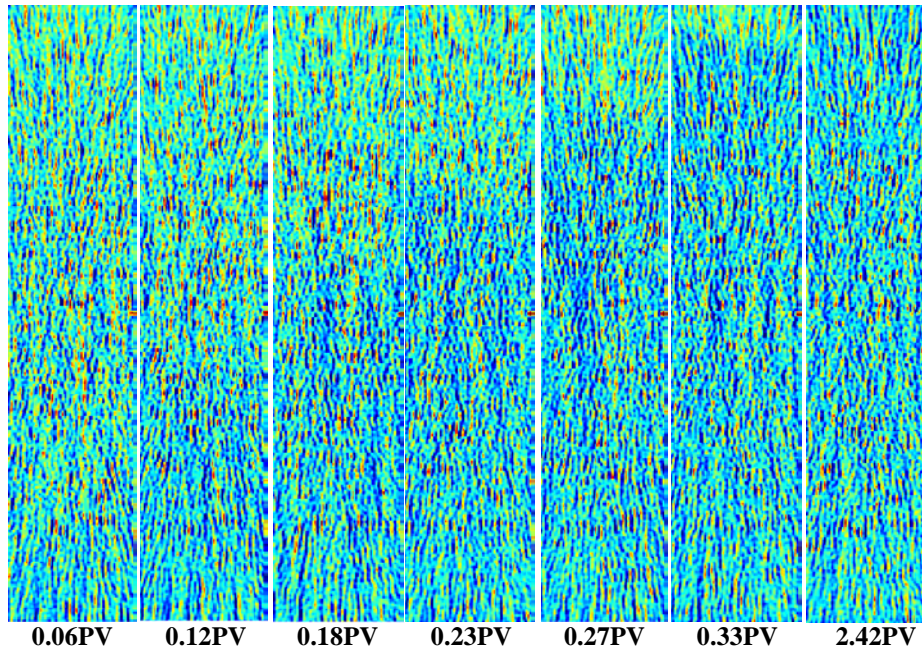


Fig. 5.11: Displacement profile during gravity stable water flooding (imbibition) with injection direction from the bottom to the top. Oil production by water flooding is evident by a colour change from light green to blue.

Fig. 5.11 demonstrates, during the imbibition, the change in colour of the images from left to right from light-green to a blueish tint, which reflects the removal of oil. Fingering and bypassing of oil by brine are also visible in the images. Fig. 5.12 shows the oil saturations obtained from the CT scan images that were presented in Fig. 5.11 by applying Eq. (5-5). The oil saturation front is wide, due to capillary diffusion and an unfavourable mobility ratio between displacing and displaced phases. The water flooding was followed by bump flood, i.e. by brine injection at $5.0 \text{ cm}^3/\text{min}$ to ensure that a residual oil saturation was reached. The last CT image was taken after bump water flooding, which gave a $1.7 \pm 0.1\%$ of the OIIP. By doing this, the remaining oil saturation reached an average of $S_{or} = 0.4 \pm 0.02$.

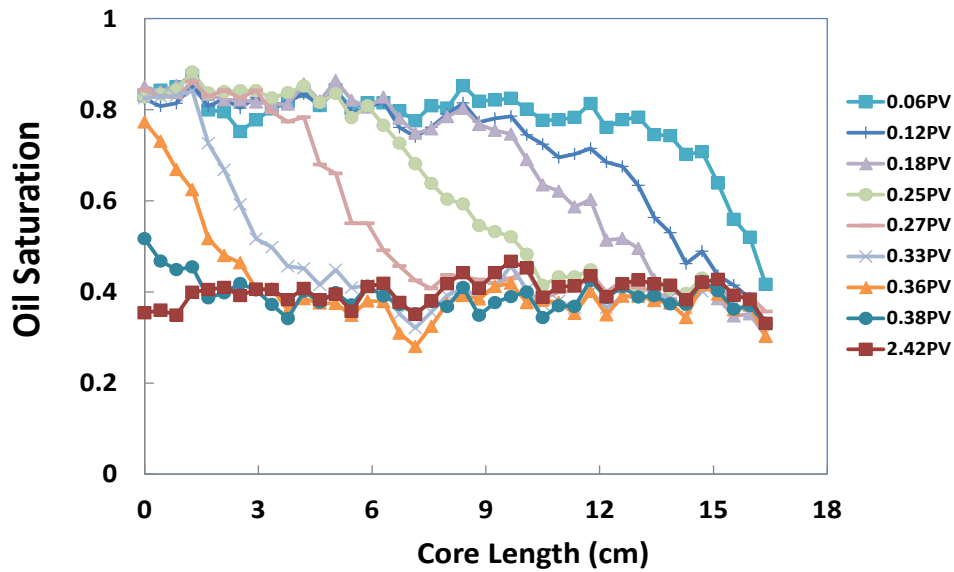


Fig. 5.12: Profile of oil saturation distribution for water flooding obtained from the corresponding CT images given in Fig. 5.11. Brine was injected from the bottom of the core, which is located on the left side of the figure. The average oil saturation at the end of water flooding was 0.4 ± 0.02 .

5.4.2.2 Oil Recovery by Alkali-Surfactant-Foam (ASF)

ASF flooding experiments were executed to examine the effects of the gas mobility reduction by foam and the IFT reduction on the oil displacement by foam. Prior to ASF flooding the core was pre-flushed by 3.0 PV of AS solution at the same flow-rate as water flooding. This was done to satisfy the adsorption capacity of the core surface, thus preventing the loss of surfactant and the delay in foam generation due to adsorption. During surfactant pre-flush, only a tiny amount of oil of about 0.5 ± 0.1 per cent of the OIIP was produced. Subsequently, N_2 and surfactant solutions were injected into the core. The MRFs obtained during foam flooding for the three cases of the chemical formulation (see Table 5.4) are depicted in Fig. 5.13 through Fig. 5.15. Here MRF is defined as the ratio of pressure drops for foam flooding to a single phase water injection at the same flow-rate. AS1 solution demonstrated a sharp increase in MRF after 0.7 PV. AS2 and AS3 tests provided smaller steady state MRF in the oil recovery experiment, as AS2 and AS3 contained less amount of AOS surfactant. For AS2 beyond 1.2 PV, MRF increases progressively and then levelled off to approximately 165. The average MRF during co-injection of N_2 with AS3 was rather low, which means that moderately stable foam was generated in the core under a considerably low IFT condition and in the presence of high residual oil saturation. The MRF fluctuation in

Fig. 5.15 was due to the wide range of pressure difference measurement (-40 to +40 Bar).

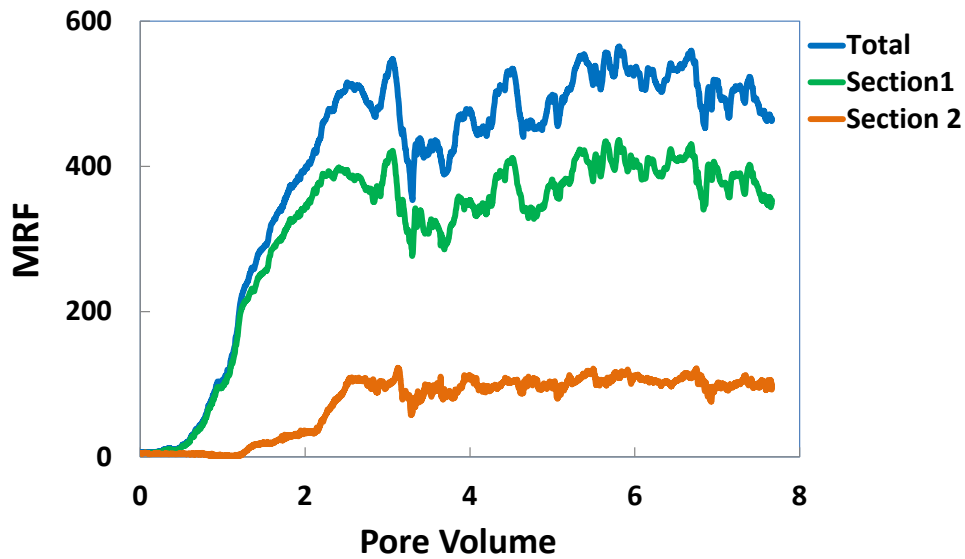


Fig. 5.13: Total and sectional MRF results along the core from the experiment of co-injection of N_2 and AS1 surfactant solution in the presence of remaining oil after water flooding. Foam quality and total velocity of 2.5 ft/day.

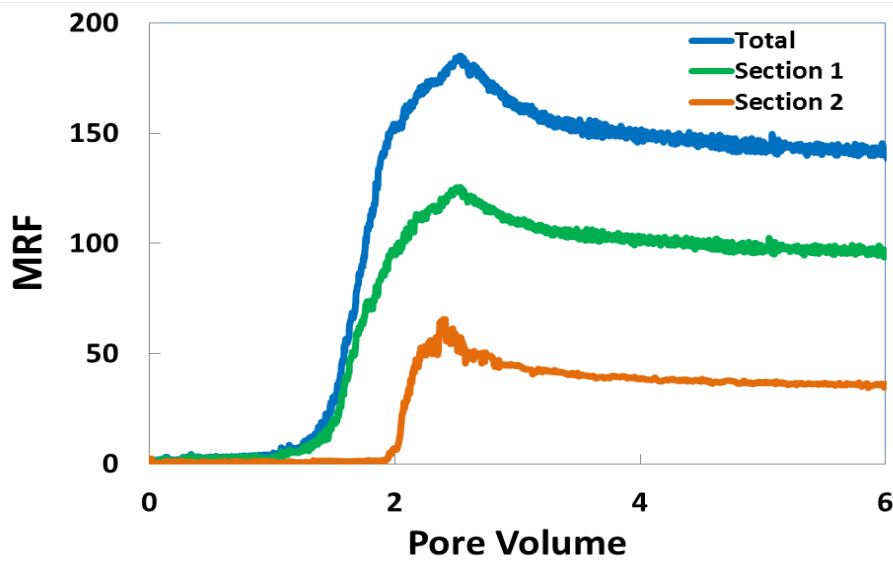


Fig. 5.14: Total and sectional MRF results along the core from the experiment of co-injection of N_2 and AS2 surfactant in the presence of remaining oil after water flooding. Foam quality and total velocity of 2.5 ft/day.

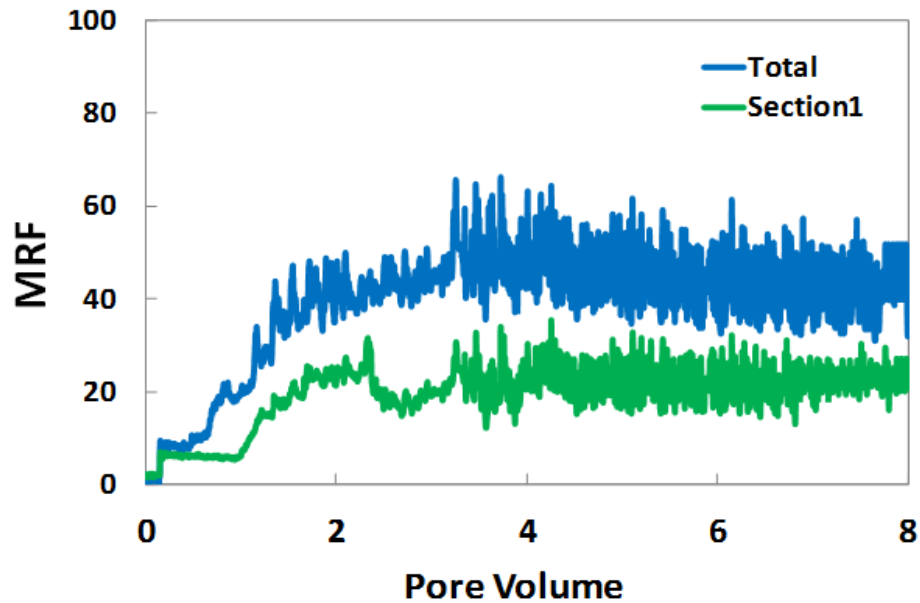


Fig. 5.15: Total and sectional MRF results along the core from the experiment of co-injection of N_2 and AS3 surfactant solution in the presence of remaining oil after water flooding. Foam quality of 80% and total velocity of 2.5 ft/day.

a) **CT scanning images.** For the experiment AS3 the core was CT scanned during foam flooding at transient and steady-state conditions, in order to discern the effects of the ultra-low IFT between the oil and the aqueous phase. The corresponding CT scan images are shown in Fig. 5.16. Light blue-green colour corresponds to the core containing surfactant solution and residual oil. Dark blue indicates the presence of foam. As gas (N_2) and the surfactant were co-injected downward into core, foam propagation is clearly visible in a change of the intensity of colour, from blue into a darker blue. This gives an insight about a change of fluid saturation from the two phase regions into the three-phase regions (i.e. oleic phase, surfactant solution and foamed gas). CT images, shown in Fig. 5.16, clearly confirms the ability of foam flooding of AS3 to displace a substantial volume of the liquid phase consisting oil.

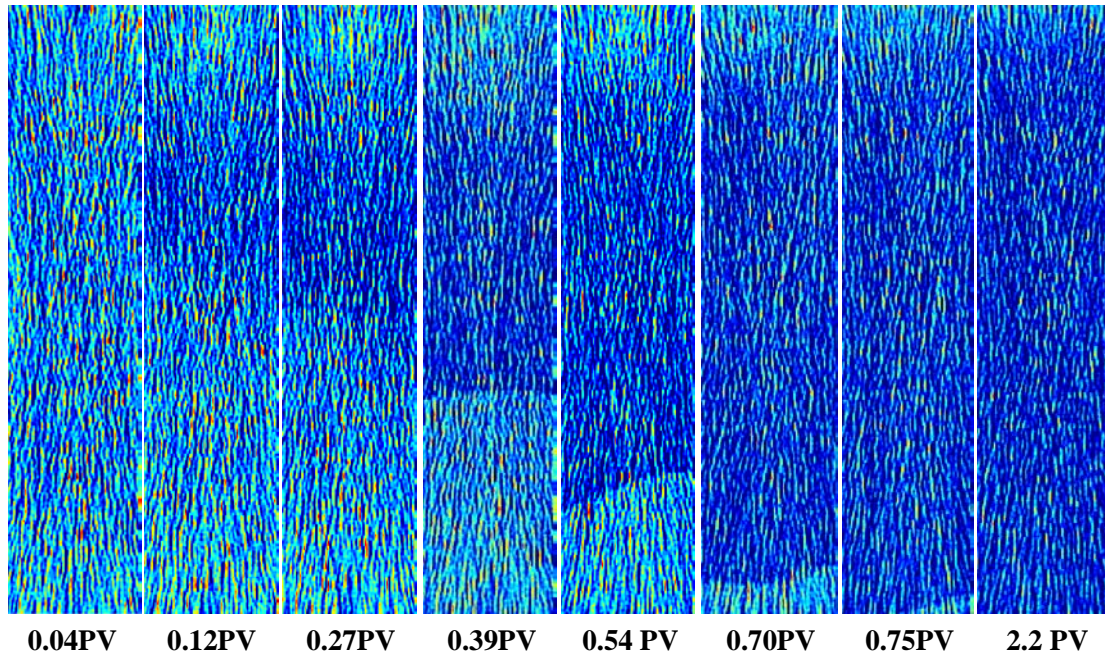


Fig. 5.16: CT images obtained during AS3 foam flooding. Foam breakthrough occurred at $0.76 \text{ PV} \pm 0.03 \text{ PV}$. Dark blue colour indicates the presence of foam phase.

Near the core inlet, over approximately 2.4 cm, a light blue/green colour remained for a long time after co-injection started indicating the persistence of high liquid saturations in the core inlet region. This was observed by others (Nguyen et al., 2007; Simjoo & Nguyen, 2011) and can be explained by the fact that the foam strength is too small to displace liquid. The amount of liquid is higher than in the case without oil (see Fig. 5.6), which supports the idea that presence of oil results in weaker foam. After the inlet face of the core, till 0.39 PV, we see that in the area, for approximately 10.5 cm distance, the foam texture is coarse and the foam is not yet fully developed, because the injected gas needed to travel a certain distance to reach a minimum pressure gradient before strong foam generates. As a result, a low amount of the liquid phase displaced, and no sharp front of gas flow together with the liquid as the foam phase formed.

According to both the CT images shown in Fig. 5.16 and the perspective of the population balance approach (Falls et al., 1988; Kavscek et al., 1997), we could argue that, total densities of flowing and stationary bubbles from the core inlet increase towards a certain value based on dominating parameters like oil saturation. It is also illustrated that as oil saturation varied during incremental oil recovery, subsequently the transient foam propagation was influenced. Then, as shown in Fig. 5.16, in the region of an advancing front from a 0.39 PV, sharp front is

characterized by a clear change in the image colour from the light blue-green colour to the dark blue. This region progressed over the core length by creating a sharp front in continuation, which indicates the formation of fairly strong foam. The CT images demonstrate excellent foam development: foam propagated as a sharp front until it reached the outlet face; moreover; the generated foam was strong enough to induce a gradual reduction of the liquid phase and oil saturations. This can be clearly seen from the colour change in the lower part (oil-bearing) of the core from, the light blue to a more intense blue. Recall the dark blue colour indicating the presence of stronger foam and, consequently, a larger liquid desaturation. Thus, the CT core-flood experiment of AS3 proved that stable foam can be generated using a chemical formulation, which provides ultra-low IFT between the oleic and liquid phases. Fig. 5.17 shows the total gas saturation corresponding to foam flow through the water-flooded section, in which a three phase (gas, oil, surfactant solution) flow occurred.

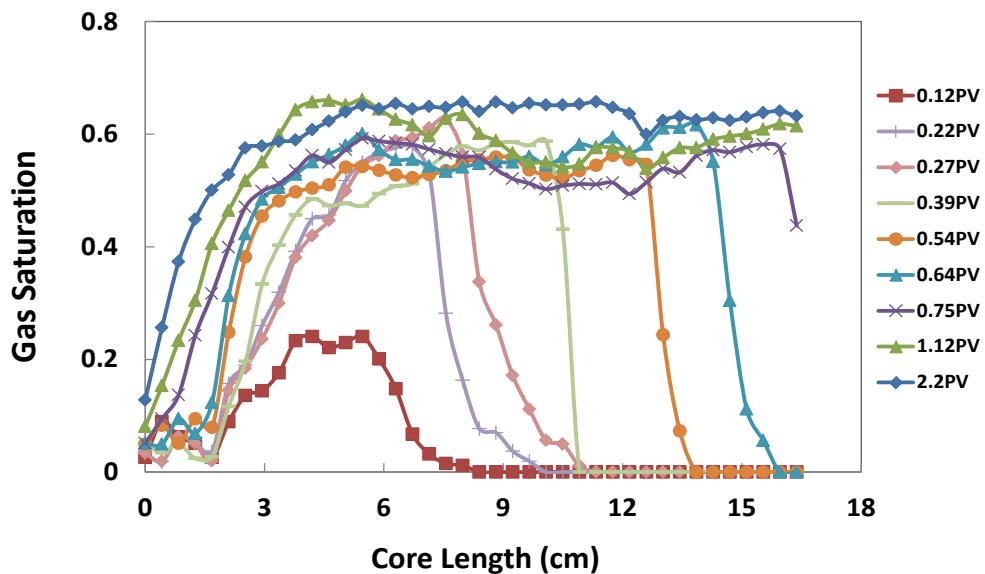


Fig. 5.17: Gas saturation profiles taken at every vertical position throughout the core before and after foam breakthrough obtained from the CT images shown in Fig. 5.16.

In this plot, the resulting average gas saturation profiles, as a function of the height of the rock sample, are illustrated. Gas saturation values are arithmetic averages of gas saturation in each horizontal line over each cross section along the rock sample. Focusing on the saturation profile taken at 0.39 PV, the region discussed above on CT images can be characterized as

follows. Gas saturation in the first 2.4 cm is low, because of the inlet effect, where capillary discontinuity resulted in retention water phase. After this inlet region, where the liquid saturation remained high, gas saturation raised to an average value of 0.63 ± 0.05 , then diminished to zero, a head of the foam front, between 5.2 cm to 17.0 cm, obviously $S_g = 0$. Fig. 5.17, after foam breakthrough, demonstrates a relatively constant saturation of $S_g = 0.65$ throughout the core with some minor fluctuations from this number. Throughout the whole time of experiments, gas saturation curves displayed a typical Buckley-Leverett shape, including the effect of gas compressibility.

b) Oil Recovery. We now analyze the tertiary oil recovery mechanism of three types co-injection of surfactant solutions and gas that exhibited different properties in terms of foam mobility control and IFT reduction. To discern the oil recovery mechanism for each EOR experiment, we examined the performance of the process in terms of cumulative oil recovery and oil cut. The cumulative oil recovery factor was defined as the ratio of the produced oil to oil initially in place (OIIP) and the oil cut defined as the fraction of oil in the produced fluid. Oil cut and cumulative oil recovery for the three studied cases are presented in Fig. 5.18 and Fig. 5.19, respectively. During all foam flooding tests, in the first 1.0 PV, the oil cut (oil production rate) increased, whereas during the later time of the testing it decreased progressively. Oil was produced first by the formation of a diffuse oil bank followed by a long tail production. For AS1, as foam injection continued for a longer time than 1PV of injection, oil recovery was at the slower rate, and mainly as a stable emulsion. An early oil breakthrough was observed during the AS1 experiment, at approximately 0.3PV (see Fig. 5.18), which is attributed to a poor oil displacement before the oil bank is formed. For the AS2 and AS3 experiments, oil breakthrough time was consistently longer, corresponding to the formation of oil with a sharper bank and a more stable oil displacement. Fig. 5.19 indicates that for AS3 oil production was larger with a higher rate and more slow in terms of breakthrough of the oil bank than others, although the MRF created by foam generation was the lowest (Fig. 5.15).

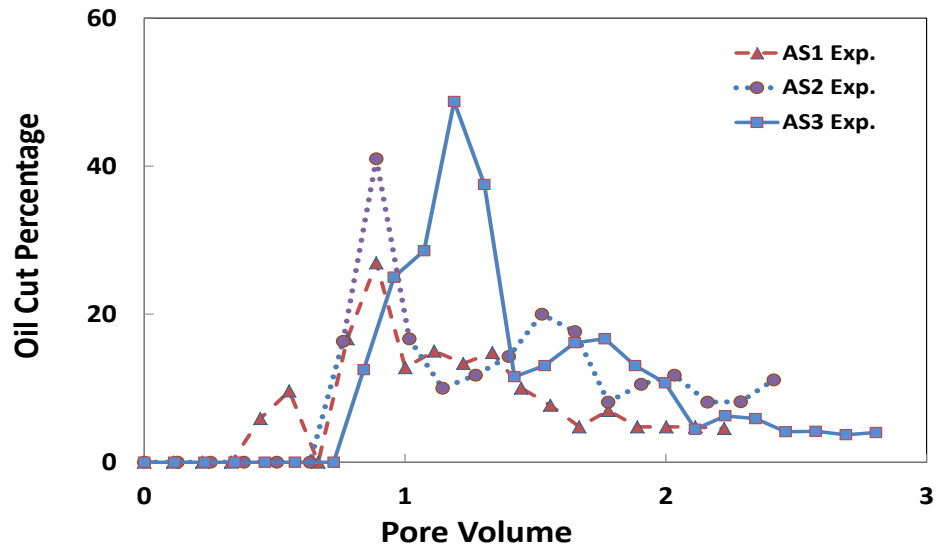


Fig. 5.18: Oil cut during foam flooding with different alkali-surfactant formulations (AS1, AS2 and AS3). Effect of IFT reduction on fraction flow of oil recovery can be seen. The first oil peaks are corresponding to oil bank formation.

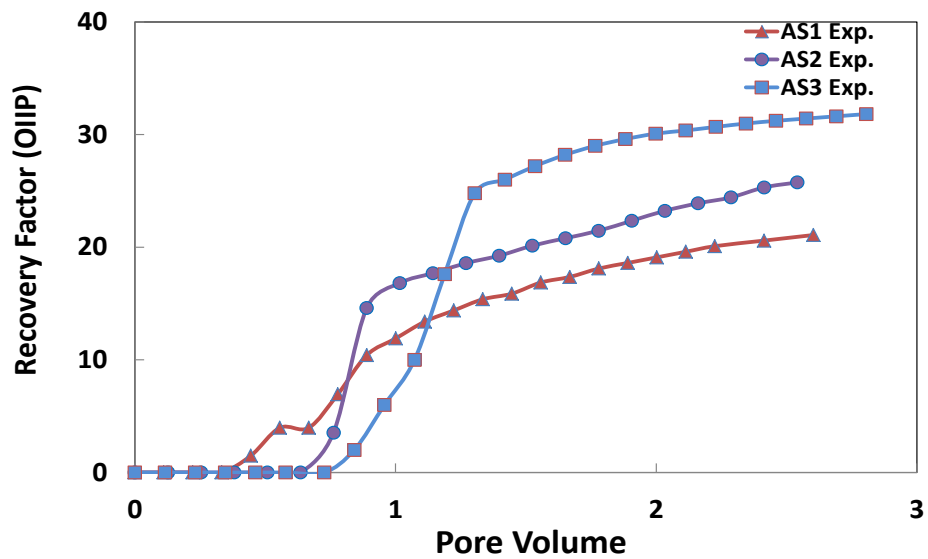


Fig. 5.19: Incremental oil recovery during foam flooding for different surfactant concentrations. Increased cumulative oil recovery was observed for lower IFT foam flooding.

Table 5.5 gives a summary of incremental oil recovery by co-injection of N₂ with three different chemical formulations investigated. For AS1 the cumulative oil effluent measurement indicated an oil recovery factor up to 22% of OIIP after injection of 2.5 PV of foam. For the AS3 case, injection of 2.5 PV of foam yielded an incremental oil recovery of 34% of OIIP. Since oil recovery by water flooding was 43±0.05 %, the overall oil recovery of foam flooding is 77.00±0.05 % OIIP. The results show that a decrease in the IFT led to substantially higher

oil recovery consisting with lower MRF (see Fig. 5.13, Fig. 5.15).

Table 5.5: Summary of incremental oil recovery by co-injection of gas with different chemical solutions.

EOR Process	S_{oi}	$R_{F,WF}$ (OIIO)	$S_{or,WF}$	$R_{F,EOR}$ (OIIO)	$S_{or,EOR}$	MRF	IFT (mN/m)	Foam BT (PV)
AS1	0.80±0.05	40±1	0.48±0.02	21.1 ± 1	0.32±0.02	570 ± 5	1.56 × 10 ⁰	0.81 ± 0.02
AS2	0.83±0.05	44±1	0.47±0.02	27.5 ± 1	0.25±0.02	165 ± 5	2.42 × 10 ⁻¹	0.79±0.02
AS3	0.81±0.05	43±1	0.46±0.02	33.7 ± 1	0.20±0.02	59 ± 5	1.17 × 10 ⁻²	0.76±0.02

The oil recovery increases substantially for AS3, when the IFT decreases compared to conventional foam flooding (AS1) EOR. Thus, in the case of AS3 foam, ultralow IFT reduction was the dominant mechanism in comparison to AS1 for the higher oil recovery. In Fig. 5.20, comparison of part of the oil recovery in effluents by foam flooding for experiments AS1 and AS3 is shown. As can be seen, produced oil by AS3 gave a more clean oil than AS1, and that, with AS1, a noticeable amount of oil production was containing emulsion formation.

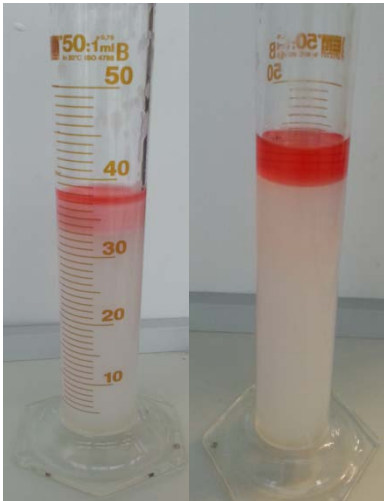


Fig. 5.20: Fluids at the outlet of the core for the AS1 foam (left image) and AS3 foam (right image). Oil is coloured red to visualize. Produced oil at the effluent of AS1 foam appearing more as an emulsion with surfactant solution. Clean oil is much more for AS3 foam. Larger liquid volume in the right column, is because of longer surfactant pre-flush.

5.5 Conclusions

- The oil displacement efficiency by chemically designed foam flooding was investigated experimentally. Three chemical formulations (AS1, AS2, AS3) capable of generating stable foam in porous media in the absence and presence of oil, while reducing the IFT to the low and ultralow values, have been examined.
- Core-floods were performed using an AS formulation providing low to ultra-low oil/water IFT, in addition to being good foaming agents with nitrogen into Bentheimer sandstone.
- The foaming of the three AS formulations in consolidated porous media in the absence of oil gave rise to gas mobility factors ranging from 894 to 282.
- A blend of two anionic surfactants with a co-solvent (AS3) was developed, both to increase the MRF and to decrease the IFT by at least three orders of magnitude. Experiments with the AS3 chemical formulation in the absence and presence of oil were monitored by an X-ray CT scanner, and during foam propagation demonstrated a stable foam front and liquid desaturation movements. CT images elucidated the transient foam flow behaviour, which is the most relevant to enhanced oil recovery.
- The chemical-foam flooding exhibited the similar characteristic of ASP flooding EOR such as the production of large oil bank at high oil cut before producing oil/emulsion. The obtained results proved that microscopic displacement efficiency in foam flooding can greatly be improved by reducing capillary pressure.
- The obtained results were compared against the typical AOS foam flooding as a base case (AS1), and resulted in the higher oil recovery and significantly less MRF for the low IFT foam than the base case experiment. Considerable portion of oil recovered in AS1 experiment formed oil-in-water emulsion, but produced oil by AS3 gave a much more clean oil-cut. These results indicated an improvement of lowering IFT during foam EOR, and necessity of having only a sufficient foam strength. This means that ultra-strong foam is not necessary to prevent a detrimental destabilization effect of oil on foam.
- This research demonstrated that low microscopic efficiency of foam flooding is due to

bypassing of trapped oil due to high capillary pressure. Fairly low IFT-foam flooding (AS2, AS3) recovered oil at the tertiary stage by a mechanism of improving volumetric sweep efficiency and increasing microscopic oil displacement.

- For future work, conducting the foam flow experiments at reservoir conditions, such as reservoir temperature and pressure, and formation wettability (oil-wet, mixed-wet), will more accurately reflect the foam behaviour during ASF EOR for oil displacement. Moreover, in addition to using blend of surfactants and co-solvent, the addition of viscosifying agent like polymer to AS slug and foam drive, is worth investigating for ASF EOR process.

Chapter 6

A New Chemical-Enhanced Oil Recovery Method?

6.1 Abstract

The efficiency of ASP flooding for EOR can be much less than expected under various reservoir conditions that include low permeability, high temperature, high formation brine salinity and the presence of divalent cations (Ca^{+2} , Mg^{+2}) in the formation brine. This is due to polymer degradation and low injectivity, alkali precipitation and scaling in the well and surface equipment. Moreover, polymers substantially reduce the capability of treatment of produced water to be used for re-injection, upcycling or discharge.

This chapter reports on an experimental study of a new chemical EOR approach that has the potential to overcome some of the above drawbacks. The new chemical formulation consists of a combination of a non-polymeric viscosity enhancement compound and a blend of two surfactants. The performance of this chemical formulation was evaluated by a series of core-flood tests on Bentheimer sandstone cores under stable gravity conditions, with the aid of X-ray Computed Tomography. A significant reduction in the residual oil saturation was observed by constructing the Capillary Desaturation Curves (CDC), suggesting that the proposed formulation is potentially a good chemical EOR agent.

The content described in this chapter is published in: Hosseini-Nasab et al., "A New Chemical Enhanced Oil Recovery Method?", *Journal of Colloids and Surfaces A: Physicochemical and Engineering Aspects*, Volume 507, 20 October 2016, Pages 89–95.

6.2 Introduction

Secondary oil recovery from water-wet or mixed-wet reservoirs by water flooding leaves a significant fraction of the OIIP in the reservoir. Roughly 65 % of OIIP remains trapped in the swept regions as residual oil (Ali & Thomas, 1989; Mai & Kantzas, 2009; Roehl & Choquette, 1985). Capillary forces responsible for the trapping of the non-wetting oil phase are mainly set by the IFT between the oil and water phases. Viscous forces on the other hand are mainly set by the viscosity of the displacing aqueous phase (Bryan & Kantzas, 2007; Bryan et al., 2008).

Chemical-enhanced oil recovery (cEOR) methods aim to reduce the residual oil saturation S_{or} by increasing the capillary number (ratio of viscous to capillary forces). This can be illustrated by constructing the CDC, i.e. the residual oil saturation plotted as a function of the capillary number. ASP is one of the most effective and attractive cEOR methods in terms of tertiary oil recovery factor (Dang et al., 2012; Lake & Johns, 2014; Sheng, 2013). In properly formulated ASP systems, the AS solution provides an ultralow IFT between the oil and water phases, while polymers ensure good mobility control, thus inducing the mobilization of the residual oil. The reaction of the alkali with fatty acids present in crude oils generates *in-situ* soap, which assists achieving ultralow IFT. The alkali also increases the pH, which reduces the adsorption of the anionic surfactant (Ojukwu et al., 2013; Stoll et al., 2011).

Despite its high efficiency, conventional ASP suffers from certain limitations that restrict their application range. The alkalis (such as NaOH, Na_2CO_3) react with divalent cation (Ca^{2+} , Mg^{2+}) present in the formation brine, causing the precipitation of insoluble salts. This will lead to permeability reduction and flow assurance problems in the production string and surface facilities (valves, flow meters, separators, etc.) (Kazemi Nia Korrani et al., 2014; Kazempour et al., 2013). In addition to the above scaling problems, the use of alkalis in a high salinity environment might induce the corrosion of the tubing and ancillary equipment and could affect the polymer performance by increasing the salinity, which are additional disadvantages of using alkalis in chemical flooding. Moreover, polymers substantially reduce the capability of treatment of produced water to be used for re-injection, upcycling or discharge. This is due to the fact that polymers, used for secondary and tertiary oil recovery, are linear anionic homopolymers or co-polymers, such as hydrolyzed polyacrylamide or acrylamide co-polymers.

Anionic polymers cause the water phase to have a strong anionic charge, which cannot be easily neutralized by the treatment processing of produced polymer water phase.

Other restrictions concern the use of high molecular weight polymers in low permeability, high salinity or high temperature (HPHT) reservoirs. Polymer injectivity is rather low in low permeability reservoirs, which may lead to clogging of the formation or even to unwanted fracturing (Delamaide et al., 2014; Zechner et al., 2013 & 2014). Above a certain temperature, polymers undergo hydrolysis, which may lead to precipitation due to interactions between the resulting polyion and anions present in the reservoir brine (Lange & Huh, 2013; Tovar et al., 2014; Yerramilli et al., 2013). The viscosity of the polymer is heavily reduced in high-salinity reservoirs due to the shrinking of the polymer molecules resulting from the screening of the electrostatic repulsions within polymer molecules (Algharaib et al., 2013; Ibrahim et al., 2006; Manichand & Seright, 2014). Therefore, a much higher polymer concentration is required to achieve the desired viscosity. In addition, in dealing with different types of crude oil, polymers can cause significant difficulties in producing the micro-emulsion solution, which is essential in the ASP flooding technique.

In this study, a new chemical formulation is introduced which hopefully will address the above limitations of traditional ASP formulations. The new chemical formulation consists of the combination of monomeric glycerol and a blend of two surfactants, namely Alpha-Olefin Sulfonate (AOS) and polymeric Fluoro-Carbon ester (FC), in the absence of any inorganic alkali. The glycerol (partially) replaces the polymer as a mobility control agent and the surfactant blend ensures sufficiently low IFT. Glycerol is a simple non-toxic sugar alcohol or polyol that is widely used in pharmaceutical formulations. It is a bio-based chemical produced by transesterification of fatty acids as a by-product in the manufacture of biodiesel (Rossi, 2008). The current cost of glycerol is high for a large-scale EOR application, but this can be expected to diminish as the abundance of glycerol grows (Pagliaro & Rossi, 2008).

This research aims to prove the feasibility of the new chemical EOR method under controlled laboratory conditions. To this end, a series of CT scans aided core-flooding experiments in the Bentheimer sandstone rock were undertaken, using the newly developed

water/glycerol/surfactant system. Then, resulting data from core-flooding experiments were used to construct the CDC.

6.3 Experimental Description

6.3.1 Materials

6.3.1.1 Chemicals

Brine containing 0.5 M (3.0 wt%) NaCl in deionized water ($\text{pH} = 6.8 \pm 0.1$) was used to prepare the surfactant solutions. A mixture of AOS and polymeric FC surfactant was used to perform the experiments. AOS is an anionic surfactant while FC is a neutral polymeric ester surfactant. Both surfactants were used as received from the supplier without further treatment. Their CMC, in the presence of 0.5 M NaCl were determined from the surface tension measurements and were found to be 4.8×10^{-3} wt% for the surfactant mixture with a weight ratio 1:1. The model oil used in the experiments was normal hexadecane (n-C16, Sigma-Aldrich) with a density of 0.78 ± 0.01 g/cm³ at 21 ± 0.5 °C. The properties of the chemicals used in this work are summarized in Table 6.1. Fluid viscosities were measured using a Brookfield Viscometer and the IFTs were measured using a KSV Sigma tensiometer using the Du Nouy ring method.

Table 6.1 Properties of the materials used to conduct the experiments

Chemical	Code	Molecular weight (g/mole)	Viscosity at 21°C (cP)	Active content (%)	Supplier
Salt	NaCl	58.50	solid	99.99	Merck
Oil	n-C16	226.00	3.3 ± 0.01	99.99	Sigma
Surfactant	AOS	315.00	1.0 ± 0.01	40.00	Stepan
Surfactant	FC 4434	No data	1.0 ± 0.01	25.00	3M
Glycerol	C ₃ H ₅ (OH) ₃	92.10	290.37 ± 0.1	99.00	Merck

6.3.1.2 Core Sample

Bentheimer sandstone cores were used to perform the experiments. The sandstone contains up to 97 % quartz and is consolidated and nearly homogeneous. The properties of the porous

samples are presented in Table 6.2. The average porosity of the core obtained from the CT scan is $21 \pm 1\%$. The absolute brine permeability of the used cores was 1.5 ± 0.1 Darcy. The core samples were drilled from a cubic block with sides of 40 cm and, then, sawn to the desired dimensions using a water-cooled diamond saw. Next, the cores were dried in an oven at $50\text{ }^{\circ}\text{C}$ for 48 hours. Then, they were cast in Araldite self-hardening glue to avoid production from the axial core sides (bypassing). From CT scans of the dry core, it was estimated that the glue had penetrated approximately 2.0 mm of the core sample. This effective thickness was used in the calculation of the total pore volumes of the cores. After hardening, the glue was machined so that the core fitted precisely into the core-holder. Several holes were drilled through the glue layer into the core surface along the core length for pressure measurements.

Table 6.2: Properties of the porous sample used for core-flooding experiments

Core sample	Bentheimer sandstone
Length (cm)	17 ± 0.1
Diameter (cm)	3.8 ± 0.1
Porosity (%)	22 ± 0.5
Pore volume (cc)	42.4 ± 0.5
Permeability (Darcy)	1.5 ± 0.1
Quartz content (wt%)	97.0 ± 2.0

6.3.1.3 Core-holder

The core-holder was made of PEEK. This synthetic material combines good mechanical properties with a low X-ray attenuation. It also transmits X-rays within a narrow energy window (re-filtering the polyenergetic source X-rays), which considerably minimizes the beam-hardening artifact due to the polychromaticity of the X-ray beam (Nguyen et al., 2005). The pressure connectors were also made of PEEK to prevent interference by the pressure lines with the CT scanning.

6.3.2 Experimental Setup

6.3.2.1 Core-flooding Setup

The setup used to conduct core-flooding experiments is shown schematically in Fig. 6.1. A high precision double-effect piston displacement pump (Pharmacia P 500) was used for liquid

injection. Several pressure difference transducers were used to monitor the pressure drop based on the inlet pressure over the core segments with increasing lengths. A backpressure regulator was used to set the outlet pressure during the experiment. The produced fluids were collected by graduated glass columns. A data acquisition system was used to automatically record the liquid injection rate, pressures and liquid production data. All experiments were conducted at room temperature (20 ± 2 °C).

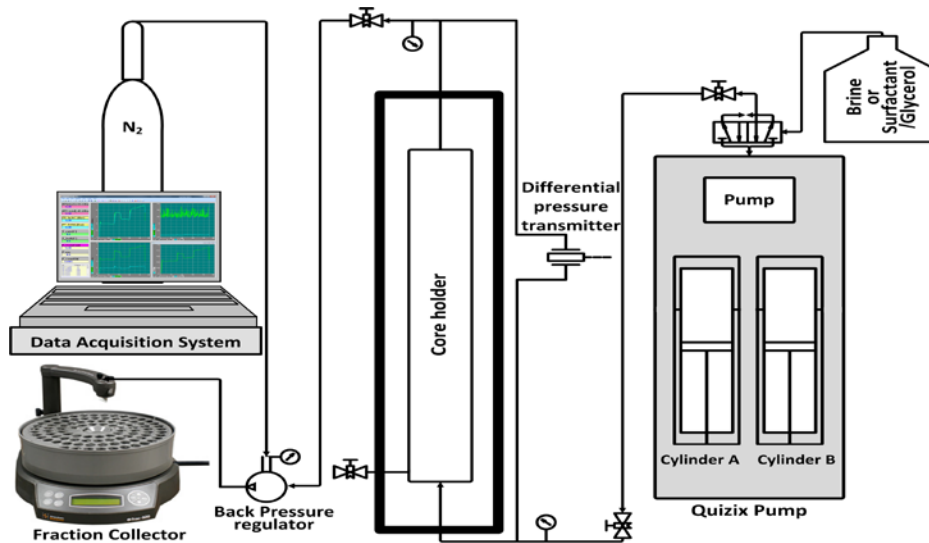


Fig. 6.1: Schematic of flow process and setup used for core-flooding experiments. The setup consists of four major parts: a test unit (core sample and core holder), measuring unit (pressure transducers), injection unit (pumps), and data acquisition system.

6.3.2.2 CT Scanner

X-ray Computed Tomography (CT) is a non-destructive testing technique for visualizing the static structure and dynamic process within opaque objects. The method is based on the attenuation of X-ray beams through the object being scanned, where a large number of the projection data of these X-rays are used to construct an image of the inside of the object. The output value of the CT scanner provides image matrices whose coefficients are the linear attenuation coefficient of the material for the selected effective energy. The CT data are expressed in Hounsfield (*HU*) units. The relationship between the attenuation coefficient in Hounsfield units and the attenuation coefficients in the inverse unit length is as follows:

$$CT = 1000 \left(\frac{\mu}{\mu_w} - 1 \right) \quad (6-1)$$

where CT is the CT-number value in Hounsfield units, μ_w is the attenuation coefficient of water in m^{-1} and μ is the local linear attenuation coefficient averaged over a voxel (or image pixel) in m^{-1} . The oil saturation is obtained from the measured CT data by using the following equation:

$$S_o = \frac{1}{\varphi} \frac{CT_{wo} - CT_{wet}}{CT_o - CT_w} \quad (6-2)$$

where CT_{oil} , CT_{wet} and CT_{wo} are respectively the measured attenuation coefficients for the oil-saturated core, water-saturated core and core containing oil and water phases. Note, that the contribution of rock to the total measured attenuation was eliminated by using a subtraction algorithm. The CT scanner used in this study is a third-generation SAMATOM Volume Zoom Quad slice scanner. The setup is placed on the end of the couch of the CT scanner and the core-holder is fixed vertically to the edge of the couch. The imaging settings used in the experiments are listed in Table 6.3. The X-ray tube of the CT scanner is operated at a voltage of 140 kV and a current of 250 mA. CT images were taken in the vertical direction from the top to the bottom of the core sample. The thickness of the CT image was 3 mm. The sequential scan mode is used for imaging acquisition with a CT slice thickness of 1 mm and 8 CT slices in each series of scans. A typical slice image consists of 512×512 pixels with a pixel size of 0.3×0.3 mm. Since the noise for CT images typically ranges from 3 to 20 HU, the accuracy of the measured fluid saturations error was within ± 2 %.

Table 6.3: Setting parameters for the CT Scan measurements

Parameter (units)	Value/Condition
Tube voltage (kV)	140
Tube current (mA)	250
Slice thickness (mm)	1.0
Pixel size (mm×mm)	0.3×0.3
Filter	B40-medium
Scan mode	Sequence

6.3.3 Experimental Procedure

The basic sequence used to perform the core-flooding experiments is as follows:

- (1) CO₂ was flushed through the dry core for 30 min at 5.0 bar injection pressure to remove the air,
- (2) Brine was injected at a flow rate of 1.0 cm³/min for more than 10 pore volumes, while maintaining the backpressure 25.0 bar to ensure complete CO₂ dissolution in brine and 100% core saturation with brine,
- 3) Primary drainage, i.e. oil was injected into the core under gravity-stable conditions (from top to bottom) at 1 cm³/min until a connate water saturation was reached,
- (4) Imbibition, i.e. brine was injected into the core (imbibition) equally under gravity-stable conditions (from bottom to top) until un-swept oil remained; water flooding continued at different flow rates to construct the first part of the CDC curve,
- (5) Combinations of the surfactant solution and glycerol, designed to increase capillary number (Ca) and to mobilize the residual oil, were injected into the core (chemical flooding).

Table 6.4 gives an overview of the experiments performed in this study. Two methods, A and B, were used for the chemical flooding to check whether the order in which chemicals are injected makes a difference to the ultimate recovery factor. In method A, water flooding was followed by the injection of glycerol at different concentrations, up to 85 wt%. Then, increasing amounts of the surfactant blend were added to the water phase that already contains 85 wt% glycerol. In method B, water flooding was followed by the injection of a surfactant solution blend, with increasing concentrations, from 0.0005 to 1.0 wt%, covering values below and above the critical micelle concentration. Then, increasing amounts of glycerol, up to 85 wt%, were added to the solution with the highest surfactant concentration (1.0 wt%).

Table 6.4: Overview of the experiments performed in this study using method A.

Displacing Fluid	Controlled Variable	Value	Velocity (m/day)	FlowRate (cm ³ /h)	Viscosity	IFT (mN/m)
Brine	Flow Rate (cm ³ /h)	15	0.32	15	1	45
Brine	Flow Rate (cm ³ /h)	30	0.64	30	1	45
Brine	Flow Rate (cm ³ /h)	60	1.27	60	1	45
30 wt% of Glycerol	Viscosity (cP)	2.5	1.27	60	2.5	45
50 wt% of Glycerol	Viscosity (cP)	5.82	1.27	60	5.82	45
65 wt% of Glycerol	Viscosity (cP)	10.5	1.27	60	10.5	45
75 wt% of Glycerol	Viscosity (cP)	24.6	1.27	60	24.6	45
85 wt% of Glycerol	IFT (mN/m)	37.8	1.27	60	37.8	45
0.0005 wt% of Surfactant + 85%Glycerol	IFT (mN/m)	41	1.27	60	37.8	41
0.001 wt% of Surfactant + 85%Glycerol	IFT (mN/m)	20.7	1.27	60	37.8	20.7
0.005 wt% of Surfactant + 85%Glycerol	IFT (mN/m)	5.5	1.27	60	37.8	5.5
0.1 wt% of Surfactant + 85%Glycerol	IFT (mN/m)	2.5	1.27	60	37.8	2.5
0.5 wt% of Surfactant + 85%Glycerol	IFT (mN/m)	1.9	1.27	60	37.8	1.9
1wt% of Surfactant + 85%Glycerol	IFT (mN/m)	1.5	1.27	60	37.8	1.5

6.4 Results and Discussion

This section presents the results of the three core-flooding experiments performed in this study. The first and second experiments were performed using method A. The second experiment was a repeat of the first one to check reproducibility. In the first experiment, the core was CT scanned at several time intervals to map the fluid saturations and to gain a better insight into the displacement processes. The third experiment, was performed using method B. Below we discuss the desaturation features induced by the different fluids in terms of the CT scan images and saturation profiles obtained by Eqs. (6–1) and (6–2), which applied slice-

averaged attenuation coefficients.

6.4.1 Fluids Properties

Fig. 6.2 shows the viscosity of the brine/glycerol mixtures and the IFT between the glycerol/brine mixture and hexadecane as a function of glycerol content in the aqueous phase. It was found that the glycerol/water viscosity ranges from 1 and 60 cP, as the glycerol content increases from 0 to 90 wt%, is in good agreement with data published in the literature (Cheng, 2008). In the experiments presented in this study, the shear rates of fluids inside the porous media varied between 1.0 to 30.0 1/s for the range of flow rates that were used (Yerramilli et al., 2013). However, glycerol is a Newtonian fluid, which has the (big) advantage that its viscosity is independent of shear rate, unlike polymers.

The IFT between hexadecane and brine/glycerol decreases slightly from 46.0 to 43.0 mN/m, i.e. by about 6.5%. These data clearly show that the addition of glycerol to the aqueous phase has a minor effect on the IFT between oil and brine/glycerol. Therefore, the premise of this study is that adding glycerol increases the capillary number by increasing the viscous forces and not by reducing the capillary force. Fig. 6.3 shows the Surface Tension (ST) between air and a 1:1 AOS:FC blend in brine versus surfactant concentration. The CMC could clearly be determined as $5.0 \pm 0.3 \times 10^{-3}$ mN/m. The downward concave shape of the ST curve suggests that the ST was not measured at equilibrium. The reason for the slight decreasing tendency of the ST above the CMC. is not completely clear. It is probably due to the slow kinetics of adsorption of the surfactant at the oil/water interface. Two concentrations below the CMC. and one above were selected and the corresponding residual oil saturation was obtained. The noteworthy point here is that the different surfactant concentrations were added to the last concentration of the glycerol/brine solution, which was 85% wt of glycerol in water. It was not possible to go above the 85% glycerol solution, because some water is needed in the solution in order to dissolve the surfactants in the glycerol solution.

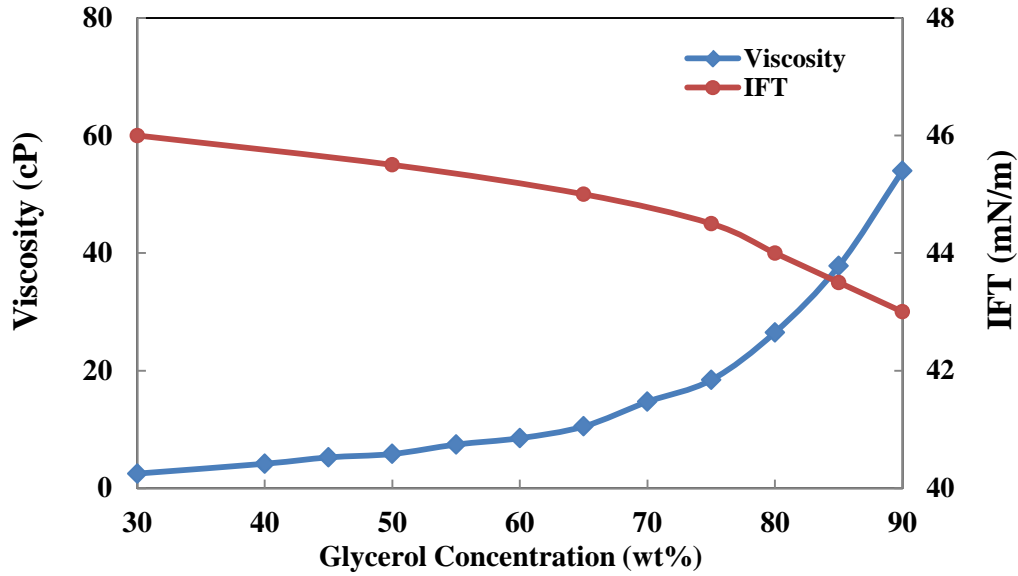


Fig. 6.2: Viscosity of glycerol/water mixture in the range of 1-60 cP as its concentration increases up to 90% weight percent. Interfacial tension (IFT) between the water/glycerol solution and n-hexadecane (oleic phase) slightly varies from 46 to 43 mN/m. The uncertainty of the measured viscosity and IFT data were within ± 0.05 and ± 0.1 , respectively.

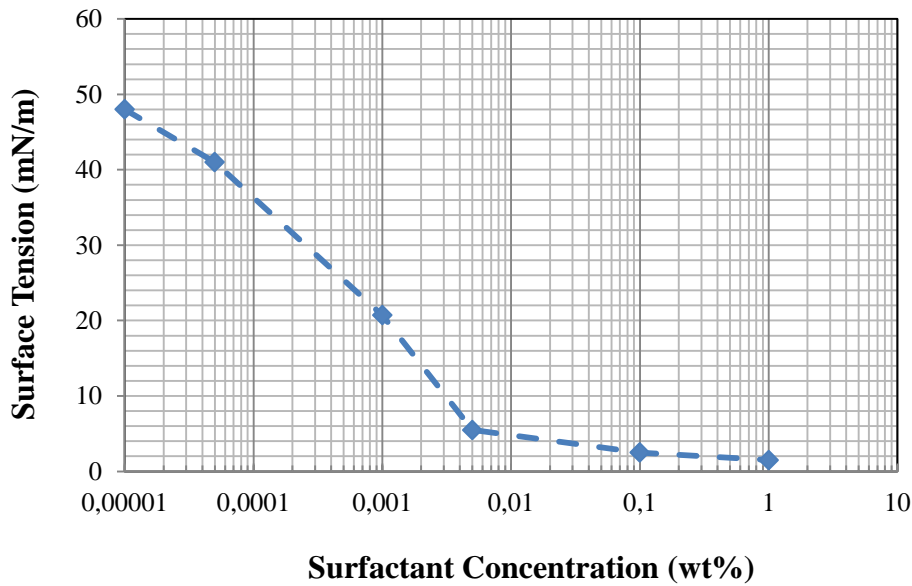
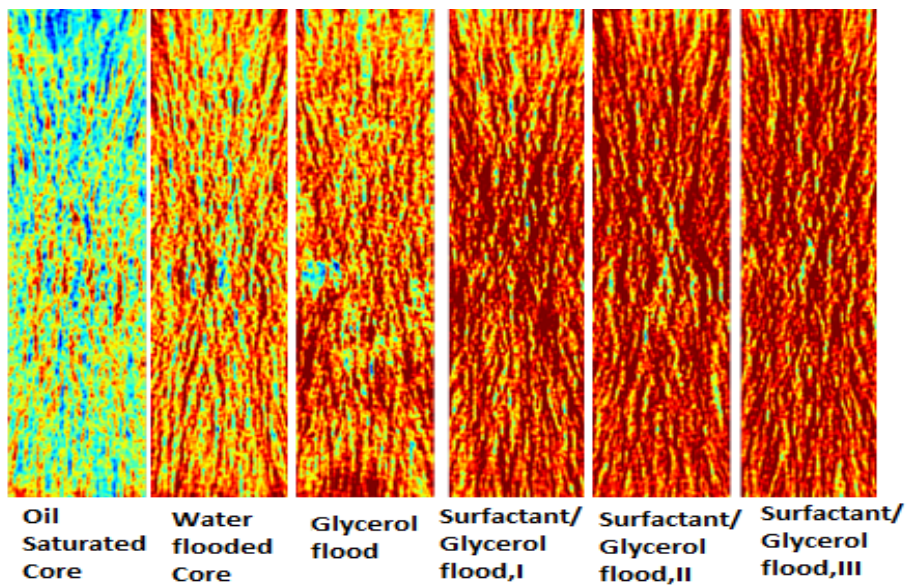


Fig. 6.3: Surface tension between air and different surfactant mixtures (1:1 AOS:FC) concentration. CMC of surfactant solution is 5×10^{-3} weight percent. The uncertainty of the measured surface tension data was within ± 0.1 .

6.4.2 Chemical Flooding

CT scans and saturation maps. Fig. 6.4 includes the CT scan images and corresponding saturation profiles obtained at the end of the primary drainage, the imbibition and at the different stages of the chemical injection. In the CT images, the colour blue/green represents the oil phase and the colour red indicates the water phase.

The first CT scan image was obtained at the end of the primary drainage. The second image is at the end of the water flooding. The third image was obtained at the end of glycerol flooding containing 85 wt% of glycerol. From the fourth image, surfactant-glycerol flooding was executed using 85 wt% of glycerol and the following surfactant concentrations: I) 0.1 wt%, II) 0.5 wt% and III) 1.0 wt%. As flooding switched from water to glycerol and, then, to surfactant-glycerol, the density of the colour red increased, which corresponds with the reducing oil saturation in the porous media.



a)

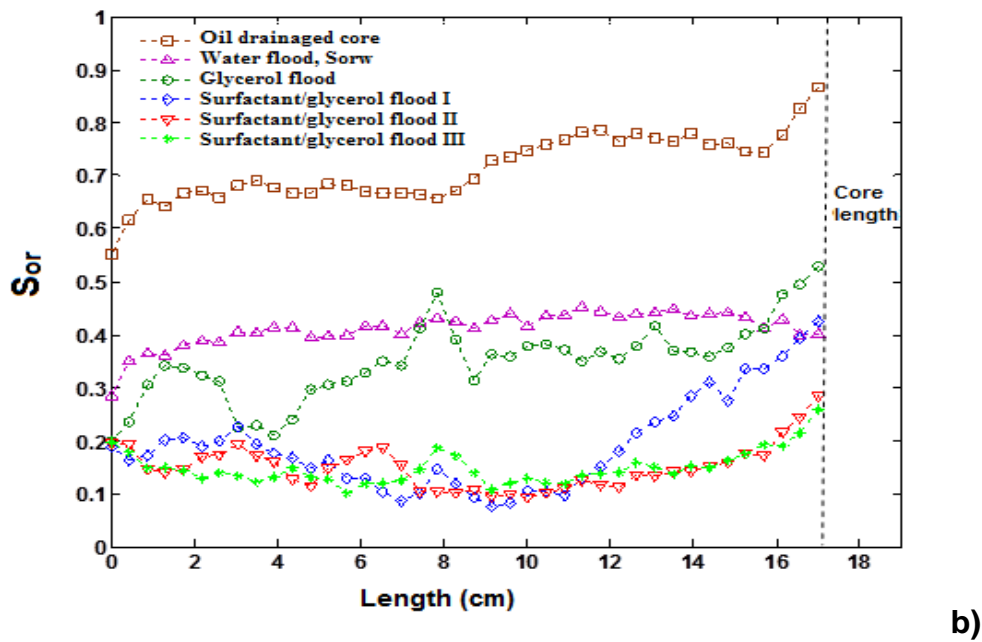


Fig. 6.4: (a) CT images and (b) corresponding oil saturation profiles, during different stages of core-flooding. The core was water-flooded by brine after primary drainage. Then it was flooded with a water/glycerol mixture containing 85 wt% of glycerol. Finally, it was flooded with surfactant/water/glycerol containing 85 wt% of glycerol and the following surfactant concentrations: I) 0.10 wt%, II) 0.5 wt% and III) 1.0 wt%. The average residual oil saturation at the end of surfactant-glycerol flooding was 0.15. The accuracy of the measured fluid saturations error was within $\pm 2\%$.

The oil saturation profiles during different stages of the core-flooding obtained from the images are shown in Fig. 6.4b. After primary drainage, the core was water-flooded with brine. The water-flooding residual oil saturation was approximately 0.40. This value is consistent with the data reported in the literature for similar core and fluids (Simjoo et al., 2013). Then, glycerol flooding, including 85 wt% of glycerol, was performed which led to an average residual oil saturation of 0.34. Residual oil saturation started decreasing further after injection of the surfactant-glycerol solution, including 85 wt% of glycerol and different surfactant concentrations: I) 0.1 wt%, II) 0.5 wt% and III) 1.0 wt%. The average residual oil saturation at the end of the surfactant-glycerol flooding was 0.15.

6.4.3 Capillary Desaturation Curves

Fig. 6.5 shows the capillary desaturation curves obtained from the three chemical injections experiments performed in this study. Note, that in this study the capillary number is defined by this equation:

$$Ca = u\mu_w/\sigma \quad (6-3)$$

where u is the Darcy velocity, μ_w is the viscosity of the displacing fluid and σ is the interfacial tension between the oil and the displacing fluid. Other definitions of the capillary number have been used in the literature (Larry et al., 2014) but Eq. (6-3) is the most adequate for the case where the displaced oil is at residual saturation when the chemical injection starts.

The first and second experiments in Fig. 6.5 were carried out under exactly the same conditions, based on procedure A (refer to Section 2.3) to check the reproducibility of the data. The third experiment was carried out using the second procedure (i.e. B), by injecting the surfactant solution after water flooding and, then, injecting the water/glycerol mixture. The CDC curves show that increasing the injection rate of the water (brine) flooding has hardly any effect on the residual oil saturation, i.e. there will be no extra oil production with increasing water injection rates in the range investigated. Regardless of the detailed injection procedures, at critical capillary numbers between 10^{-6} and 10^{-5} the residual oil saturation, the S_{or} decrease sharply until it they reach approximately 5% at a capillary number $Ca = 10^{-3}$. This value is lower than those obtained in optimized alkali-surfactant formulations (Chou & Shah, 1981; Larry & Johns, 2014). It clearly indicates that the brine/glycerol/surfactant composition is potentially a highly effective chemical for enhancing oil recovery.

The data in Fig. 6.5 also show that procedure B, surfactant flooding followed by surfactant/glycerol flooding, has a higher critical capillary number at which the residual oil saturation starts to decrease. This leads to a lower final residual oil saturation than procedure A, even though the final capillary number is higher. The reason for this difference is not completely clear, but we suspect that injecting the surfactant immediately after water flooding leads to the formation of emulsions and to redistribution of the residual oil, which complicates the displacement from the core. The CDC curves shown in Fig. 6.5 are qualitatively similar to those reported in the literature (Abeyasinghe et al., 2012; Bashiri & Kasiri, 2011; Ding & Kantzas, 2004; Johannesen & Graue, 2007; Maldal et al., 1999). However, they are innovative in two essential ways: 1) the CDC curves for the system consisting of glycerol and surfactants (AOS/FC blend) as the aqueous solution displacing the oil phase are reported here for the first

time, as far as this study’s authors are aware, and 2) the same core was used to cover the entire range of capillary numbers required to observe the desaturation, whereas in the literature authors often used different cores.

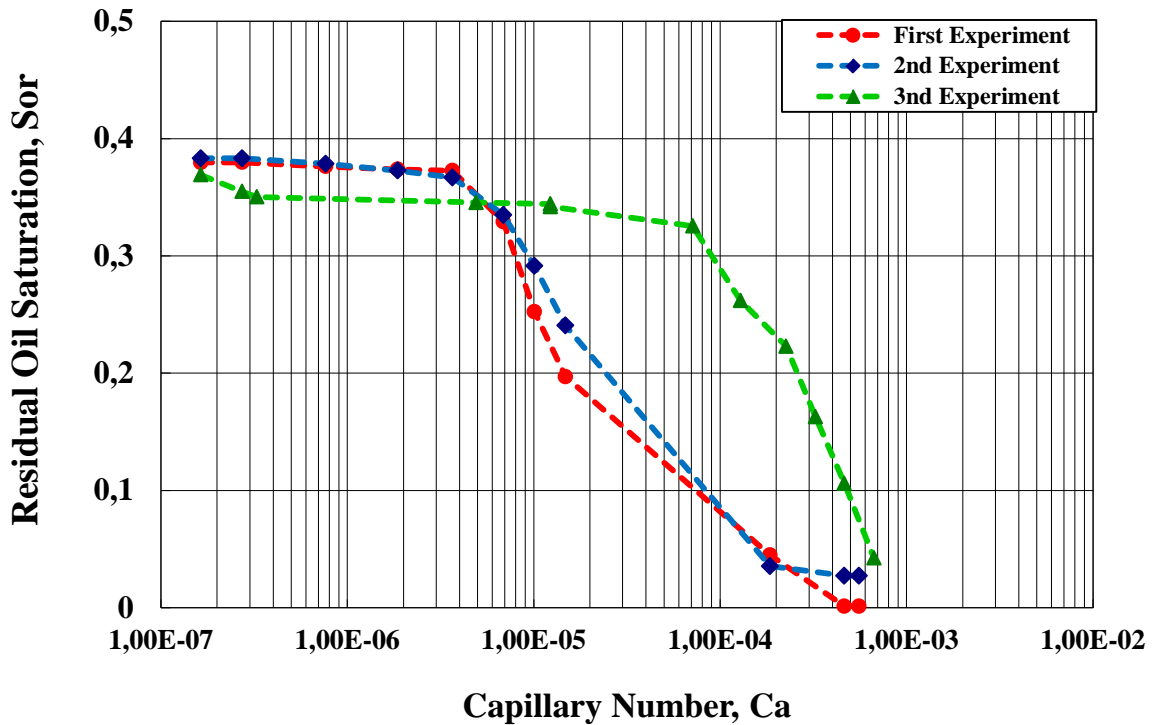


Fig. 6.5: Capillary Desaturation Curve (CDC) for the Bentheimer sandstone with two different procedures: 1) The blue and red curves are according to procedure A, which was stated in Section 2.3 and in Table 6.4: Water flooding → Water+Glycerol solution injection→Water+Glycerol+AOS:FC solution injection. 2) The green curve is according to procedure B (mentioned in Section 2.3): Water flooding→ AOS:FC solution injection→Water+Glycerol+AOS:FC solution injection. CT images and oil saturation profiles of the first scenario (A) of the construction of CDC were illustrated in Fig. 6.4. The accuracy of the measured residual oil saturation error was within $\pm 2\%$.

6.5 Conclusion Remarks

We have investigated whether aqueous solutions of glycerol and AOS+FC surfactant blend have the potential to enhance oil recovery from water-flooded sandstone reservoirs. The CDC for the system n-hexadecane/brine in Bentheimer sandstone cores was obtained by injecting brine at increasing superficial velocities, at increasing viscosities (by the addition of glycerol) and at decreasing interfacial tensions between the oil and displacing fluids (by the addition of an AOS+FC surfactant blend). Upon increasing the capillary number from approximately 10^{-7} to nearly 10^{-2} , a steep decrease in residual oil saturation above a certain critical capillary

number was observed. This is a clear indication that an adequately formulated system of brine/glycerol/surfactant could be an EOR system with a performance similar to those of the more classical ASP systems. We do not claim that our new formulation is more successful than traditional chemical EOR methods (mainly ASP) in terms of the recovery factor, but we believe that, at an equal recovery factor, the new chemical formulation, consisting of a glycerol/water/surfactant blend, has distinctive advantages under certain reservoir conditions, as explained in this chapter.

Chapter 7

Summary and Conclusion

7.1 Summary

This thesis presented an extensive study on various aspects of ASF flooding process for EOR. It provides insight into hybrid EOR processes that are of a combination of immiscible gas and chemicals injection in sandstone reservoir. We wanted to discover the mechanism of oil displacement by ASF flooding in terms of 1) formation of oil bank, 2) transport of dispersed oil, and 3) movement and pushing of oil bank and dispersed oil by foam. The main premise of this thesis is whether immiscible foam flooding as an EOR technique can be improved by ASF flooding by a combination of the mechanisms of ASP EOR and Foam EOR methods? The first part of the thesis, chapters two and three, is devoted to numerical simulation and mechanistic modelling of the Foam flooding EOR process and the ASP flooding EOR process. Knowledge obtained from these two chapters formed the basis for further study of the behavior of foam in bulk and porous media in the presence of oil. The second part, chapters four to six, is based on the systematic laboratory experimental study of ASF EOR in the bulk and in the consolidated porous media conditions, and subsequently proposing a novel chemical EOR approach. Below we will give a summary of the main findings obtained in this thesis.

7.2 Conclusion

The study presented in **Chapter 2** demonstrated an integrated approach for the numerical simulation of foam transport in porous media with and without the oleic phase. First, the LE-IT) foam model was matched to the foam core-flood experiments in the absence of the oleic phase, by taking into account the foam dry-out phenomena, the rheological characteristics along with shear thinning properties and the foam-quality regimes. The parameters of the water-saturation and the shear-rate dependent functions (F_2 and F_4) were determined by history-matching the foam quality-scan data at the steady-state condition in the low/high quality regimes. The corresponding parameters of F_2 and F_4 functions were then used to model the effect of surfactant concentration on the pressure build-up induced by foam. The parameters of the surfactant-dependent function (F_1) were obtained by matching the numerical and experimental pressure drop data for the transient and steady-state conditions.

Then, the numerical simulation of foam flooding in the presence of water-flooding residual oil was performed by estimating the oil-saturation dependent function of the foam mobility interpolation factor. The numerically calculated pressure drop fitted well with the experimental lab data of the transient and steady-state foam generation and propagation in the presence of oil. Two distinct regimes of incremental oil production were captured by the numerical simulation, first by the formation of an oil bank and, then, followed by a long tail production. The results obtained showed that the developed numerical model reproduced the main feature of the transient and steady-state foam flow regimes in presence of the oleic phase. This was supported by a good match between pressure and oil recovery profiles, obtained numerically with those obtained from the foam flooding EOR experiment in the Bentheimer sandstone core samples.

In **Chapter 3**, a mechanistic model was developed to explore the causes behind the high oil recovery factor of the ASP flooding EOR at under-optimum salinity conditions. The ASP flooding process was modelled by a predictive model with appropriate physics to fully capture the underlying mechanisms including the surfactant phase behaviour as a function of effective salinity, temperature and co-solvent concentration, fluid rheology, oil desaturation, and

geochemical reactions. To take into account the effect of geochemical reactions occurring in the core, EQBATCH, the built-in geochemical module of UTCHEM, was used through which the initial equilibrium conditions, the CEC (cation exchange capacity) and HEC (hydrogen exchange capacity), were calculated.

From the study, it was noticed that there are other factors influencing the injected ASP slug salinity that affect the surfactant phase behaviour of the process. These factors were identified as: alkali-rock reactions, the initial salinity state of the reservoir, the influence of brine in water flooding and the chemicals in the ASP slug, causing a shift in the ASP slug salinity. The obtained results from numerical simulation showed an excellent match of the numerical simulations with the experiments and results obtained for the oil-cut, pressure drop, cumulative oil recovery, pH profile, surfactant, and carbonate concentration in the effluents. Based on the ASP flooding design, the effective salinity was perpetually under-optimum below the lower salinity limit. The high oil recovery factors were independent of ultralow IFT values (less than 10^{-2} mN/m) and low residual saturation values were obtained at the lower optimum salinity limit.

After the chemical breakthrough, higher values of effective salinity for the ASP slug (0.466 mequiv/mL, 2.5 wt% NaCl) were noticed than the designed salinity for the experiment (0.34 mequiv/mL). This variation in salinity is attributed to the geochemical reactions, including a desorption of ions such as Na^+ from the rock through a cation exchange, which influences the alkali consumption as well. The divalent cations form complexes with the surfactants that influence the salinities. Furthermore, the alcohol co-solvent in the ASP slug also influences the optimal salinities of the micro-emulsion. Thus, the presence of surfactants and alcohol in the ASP slug causes higher effective salinities than the polymer drive through the divalent cations complexes included in the geochemical reaction model. According to the effective salinity calculated during the ASP EOR process, the numerical simulation developed in this work can be used to reject the ASP flooding systems which could lead to the over-optimum salinity condition. This reduces the risk of a surfactant trapping and losses due to a migration of surfactant into the oil-rich phase in over-optimum salinity conditions in the field.

The pH profile of the simulation showed a higher value for the alkali front than the

measured data, even though less carbonate was recovered in the simulation than in the measured data. The main source of alkali consumption was found to be the exchange reactions between H^+ and Na^+ . This exchange capacity was seen to shift the point of the chemical breakthrough and corresponding pH and carbonate fronts. The alkali consumption after the chemical breakthrough in the simulation was lower than in the experiment. This could be improved by taking into account (1) the dissolution of minerals such as quartz even at a pH below 10, and (2) the dissolution and precipitation of clays such as kaolinite ($Al_2Si_2O_5(OH)_4$) in the geochemical model.

The study in **Chapter 4** aimed to discover a synergistic effect between micro-emulsion phase behaviour and foam stability in bulk and to design a high-performance chemical system for an optimal Alkali-Surfactant-Foam (ASF) EOR process. A surfactant formulation, giving ultralow IFT at the optimum salinity and with fairly good foaming characteristics for the slug/drive of the ASF flooding process, was experimentally achieved.

A water and oil solubilization ratio of 10 in the micro-emulsion phase behaviour test, as a criterion to get a sufficiently low IFT for a high tertiary oil recovery, was met by all systems containing 1.0 wt% surfactant. However, for the system of 0.5 wt% of surfactant, this criterion was only met for the system interacting with acidic oil, where there is *in-situ* soap generation assisting IFT reduction. The presented alkali-surfactant formulation in this study lowered IFT between the oil and aqueous phase from nearly 30 mN/m to $10^{-1} - 10^{-3}$ mN/m. This allows the chemical formulation to create a considerably lower IFT-foam flooding with a higher capillary number than conventional foam for displacing trapped oil from porous media.

The effect of the alkalinity on foam stability could be attributed either to screening the repulsive forces between the ionic head group resulting from cationic-anionic-type interaction and decreasing double layer repulsion or to the change in the micelle structure from spherical micelles to other more complex structures. A large amount of *in-situ* soap generation resulted in diminishing foam stability. This observation could be interpreted by the rapid spreading of oil droplets that have a low surface tension over the lamella, resulting in augmenting the curvature radius of the bubbles and decreasing the surface elasticity and surface viscosity. This

subsequently can cause a rupture in the foam structure by creating weak spots over the interfacial lamella film.

Less foam stability at a significantly low IFT between the aqueous phase and oleic phase can also be explained by the fact that the gas-liquid interface is more mobile at a lower surface tension, which tends to increase the rate of liquid drained out of the plateau border. At lower surface tensions, the capillary suction at the plateau border (which is against gravity) is smaller and, therefore, the rate of foam drainage is greater. Thus, uneven thinning and instabilities of the film might happen, which will cause acceleration of film drainage and lamellar rupture. The classical phenomenological parameters, such as spreading and entering coefficients, have been used with some success and similarities in the current trend of research; however, foam performance by these parameters does not correlate with the foam stability to oil for most of the experiments.

In **Chapter 5**, the oil displacement efficiency by chemically designed foam flooding was investigated experimentally. Three chemical formulations (AS1, AS2, AS3), capable of generating stable foam in porous media in absence and presence of oil while reducing the IFT to low and ultralow values, have been examined. Core-floods were performed, using an AS formulations providing low to ultra-low oil/water IFT, in addition to being good foaming agents with nitrogen into Bentheimer sandstone. The foaming of the three AS formulations in core-floods experiments in the absence of oil gave rise to gas mobility factors ranging from 894 to 282. A blend of two anionic surfactants with co-solvent (AS3) was developed both to increase the MRF and to decrease the IFT by at least three orders of magnitude. Experiments with the AS3 chemical formulation in the absence and presence of oil were monitored by an X-ray CT scanner and, during foam propagation, demonstrated the stable foam front and liquid desaturation movements. CT images elucidated the transient foam flow behaviour, which is the most relevant to enhanced oil recovery.

The obtained results were compared against the typical AOS foam flooding as a base case (AS1), and resulted in the higher oil recovery and significantly less MRF for the low IFT foam than the base case experiment. Considerable portions of oil, recovered in the AS1 experiment, formed an oil-in-water emulsion, but produced oil by AS3 gave much higher level of clean-oil-

cut. Fairly low IFT-foam flooding (AS2, AS3) recovered oil at the tertiary stage by a mechanism of improving volumetric sweep efficiency and by increasing microscopic oil displacement. These results indicated an improvement of lowering IFT during foam EOR and necessity of having a sufficient foam strength. This means that ultra-strong foam is not necessary to prevent a detrimental destabilization effect of oil on foam. The chemical-foam flooding exhibited a similar characteristic of ASP flooding EOR, such as the production of a large oil bank at a high oil-cut before producing oil/emulsion. The obtained results proved that microscopic displacement efficiency in foam flooding can greatly be improved by reducing capillary pressure. This research demonstrated that low microscopic efficiency of foam flooding is due to the bypassing of trapped oil due to a high capillary pressure.

Chapter 6 reports on an experimental study of new chemical EOR method that has the potential to overcome several of the drawbacks of using polymer and alkali. The new chemical EOR method consists of the combination of a non-polymeric viscosity enhancement compound and a blend of two surfactants. We have investigated whether aqueous solutions of glycerol and a AOS+FC surfactant blend have the potential to enhance oil recovery from water-flooded sandstone reservoirs. The performance of this chemical formulation was evaluated by a series of core-flood tests on Bentheimer sandstone cores under stable gravity conditions with the aid of X-ray Computed Tomography. The capillary desaturation curves of a new chemical EOR method for the Bentheimer rock was constructed. Upon increasing the capillary number from approximately 10^{-7} to nearly 10^{-2} , a steep decrease in residual oil saturation above a certain critical capillary number was observed. This is a clear indication that an adequately formulated system of brine/glycerol/surfactant could be an EOR system with a performance similar to those of more classical ASP systems. For the proposed new chemical EOR method, the use of polymer and alkali is not required, which prevents the polymer and alkali issues for EOR, such as degradation and low injectivity of polymer, alkali precipitation and scaling in the well and surface equipment. This makes the presented new chemical EOR robust.

Bibliography

- Abeysinghe, K. P., Fjelde, I., & Lohne, A. (2012). Dependency of Remaining Oil Saturation on Wettability and Capillary Number. In *SPE Saudi Arabia Section Technical Symposium and Exhibition*. Society of Petroleum Engineers. <http://doi.org/10.2118/160883-MS>
- Alagic, E., & Skauge, A. (2010). Combined Low Salinity Brine Injection and Surfactant Flooding in Mixed–Wet Sandstone Cores. *Energy & Fuels*, 24(6), 3551–3559. <http://doi.org/10.1021/ef1000908>
- Algharaib, M., Alajmi, A., & Gharbi, R. (2013). Investigation of Polymer Flood Performance in High Salinity Oil Reservoirs. In *SPE/DGS Saudi Arabia Section Technical Symposium and Exhibition*. Society of Petroleum Engineers. <http://doi.org/10.2118/149133-MS>
- Ali, S. M. F., & Thomas, S. (1989). The Promise And Problems Of Enhanced Oil Recovery Methods. In *Technical Meeting / Petroleum Conference of The South Saskatchewan Section*. Petroleum Society of Canada. <http://doi.org/10.2118/SS-89-26>
- Alvarado, V., & Manrique, E. (2010). Enhanced Oil Recovery: An Update Review. *Energies*, 3(9), 1529–1575. <http://doi.org/10.3390/en3091529>
- Arhore, O. J. (2012). *Experimental investigation of non optimum conditions for alkaline surfactant polymer flooding*.
- Ashoori, E., Marchesin, D., & Rossen, W. R. (2011). Dynamic foam behavior in the entrance region of a porous medium. *Colloids and Surfaces A: Physicochemical and Engineering Aspects*, 377(1), 217–227. <http://doi.org/10.1016/j.colsurfa.2010.12.043>
- Barnes, J. R., Dirkzwager, H., Smit, J. R., & Smit, J. P. (2010). SPE 129766 Application of Internal Olefin Sulfonates and Other Surfactants to EOR . Part 1 : Structure - Performance Relationships for Selection at Different Reservoir Conditions. In *SPE Improved Oil Recovery Symposium held in Tulsa, Oklahoma, USA, 24–28 April* (pp. 1–16).
- Barnes, J. R., Groen, K., Dubey, S., Reznik, C., & Shepherd, A. G. (2012). Controlled Hydrophobe Branching to Match Surfactant to Crude Oil Composition for Chemical EOR. In *SPE Improved Oil Recovery Symposium, 14-18 April, Tulsa, Oklahoma, USA*.
- Barnes, J. R., Smit, J. P., Smit, J. R., Shpakoff, P. G., Raney, K. H., & Puerto, M. C. (2008). Phase Behaviour Methods for the Evaluation of Surfactants for Chemical Flooding at Higher Temperature Reservoir Conditions. In *SPE/DOE Improved Oil Recovery Symposium held in Tulsa, Oklahoma, U.S.A., 19–23 April* .

- Bashiri, A., & Kasiri, N. (2011). Properly Use Effect of Capillary Number on Residual Oil Saturation. In *Nigeria Annual International Conference and Exhibition*. Society of Petroleum Engineers. <http://doi.org/10.2118/150800-MS>
- Battistutta, E., van Kuijk, S. R., Groen, K. V., & Zitha, P. L. J. (2015). Alkaline-Surfactant-Polymer (ASP) Flooding of Crude Oil at Under-Optimum Salinity Conditions. In *SPE Asia Pacific Enhanced Oil Recovery Conference* (pp. 1–20). Society of Petroleum Engineers. <http://doi.org/10.2118/174666-MS>
- Boeije, C. S., & Rossen, W. R. (2013). Fitting Foam Simulation Model Parameters to Data, (April 2013), 16–18.
- Boeije, C. S., & Rossen, W. R. (2015). Fitting Foam-Simulation-Model Parameters to Data : I. Coinjection of Gas and Liquid, (February).
- Bourrel, M. M., & Schechter, R. R. (1988). MICROEMULSIONS AND RELATED SYSTEMS: Formulations, Solvency and Physical Properties. Retrieved February 12, 2015, from <http://www.amazon.com/MICROEMULSIONS-AND-RELATED-SYSTEMS-Formulations/dp/2710809567>
- Bryan, J. L., & Kantzas, A. (2007). Enhanced Heavy-Oil Recovery by Alkali-Surfactant Flooding. In *SPE Annual Technical Conference and Exhibition*. Society of Petroleum Engineers. <http://doi.org/10.2118/110738-MS>
- Bryan, J. L., Mai, A. T., & Kantzas, A. (2008). Investigation Into the Processes Responsible for Heavy Oil Recovery by Alkali-Surfactant Flooding. In *SPE Symposium on Improved Oil Recovery*. Society of Petroleum Engineers. <http://doi.org/10.2118/113993-MS>
- Buchavzov, N., & Stubenrauch, C. (2007). A disjoining pressure study of foam films stabilized by mixtures of nonionic and ionic surfactants. *Langmuir*, 23(10), 5315–5323. <http://doi.org/10.1021/la063642u>
- Campbell, R. A., Yanez Arteta, M., Angus-Smyth, A., Nylander, T., & Varga, I. (2011). Effects of bulk colloidal stability on adsorption layers of poly(diallyldimethylammonium chloride)/sodium dodecyl sulfate at the air-water interface studied by neutron reflectometry. *The Journal of Physical Chemistry. B*, 115(51), 15202–13. <http://doi.org/10.1021/jp2088803>
- Carey, E., & Stubenrauch, C. (2009). Properties of aqueous foams stabilized by dodecyltrimethylammonium bromide. *Journal of Colloid and Interface Science*, 333(2), 619–27. <http://doi.org/10.1016/j.jcis.2009.02.038>
- Cheng, L., Reme, A. B., Shan, D., Coombe, D. A., & Rossen, W. R. (2000). Simulating Foam Processes at High and Low Foam Qualities. In *SPE/DOE Improved Oil Recovery Symposium*. Society of Petroleum Engineers. <http://doi.org/10.2118/59287-MS>
- Cheng, N.-S. (2008). Formula for the Viscosity of a Glycerol–Water Mixture. *Industrial & Engineering Chemistry Research*, 47(9), 3285–3288. <http://doi.org/10.1021/ie071349z>
- Chou, S. in, & Shah, D. O. (1981). Optimal Salinity Concept for Oil Displacement By Oil-External Microemulsions and Graded Salinity Slugs. *Journal of Canadian Petroleum Technology*, 20(3), 83–91. <http://doi.org/10.2118/81-03-08>
- Christensen, J. R., Stenby, E. H., & Skauge, A. (2001). Review of WAG Field Experience. *SPE Reservoir Evaluation & Engineering*, 4(02), 97–106. <http://doi.org/10.2118/71203-PA>
- Christiansen, R. L., & Howarth, S. M. (1995). *Literature Review and Recommendation of Methods for Measuring Relative Permeability of Anhydrite from the Salado Formation at*

the Waste Isolation Pilot Plant.

- Cottin, C., Morel, D., Levitt, D., Cordelier, P., & Pope, G. (2012). Alkali Surfactant Gas Injection: Attractive Laboratory Results Under the Harsh Salinity and Temperature Conditions of Middle East Carbonates. In *Abu Dhabi International Petroleum Exhibition & Conference held in Abu Dhabi, UAE, 11–14 November.*
- Crogh, N. A., Eide, K., & Morterud, S. E. (2002). WAG Injection at the Staffjord Field, A Success Story. In *European Petroleum Conference.* Society of Petroleum Engineers. <http://doi.org/10.2118/78348-MS>
- Dang, C., Nguyen, N., Chen, Z., Nguyen, H., Bae, W., & Phung, T. H. (2012). A Comprehensive Evaluation of the Performances of Alkaline/Surfactant/Polymer in Conventional and Unconventional Reservoirs. *Proceedings of SPE Asia Pacific Oil and Gas Conference and Exhibition.* <http://doi.org/10.2118/160444-MS>
- Delamaide, E., Tabary, R., & Rousseau, D. (2014). Chemical EOR in Low Permeability Reservoirs. In *SPE EOR Conference at Oil and Gas West Asia.* Society of Petroleum Engineers. <http://doi.org/10.2118/169673-MS>
- Delshad, M., Han, C., Veedu, F. K., & Pope, G. a. (2013). A simplified model for simulations of alkaline-surfactant-polymer floods. *Journal of Petroleum Science and Engineering*, *108*, 1–9. <http://doi.org/10.1016/j.petrol.2013.04.006>
- Demin, W., Jiecheng, C., Junzheng, W., Zhenyu, Y., Yuming, Y., & Hongfu, L. (1999). Summary of ASP Pilots in Daqing Oil Field.
- DeZabala, E. F., Vislocky, J. M., Rubin, E., & Radke, C. J. (1982). A Chemical Theory for Linear Alkaline Flooding. *Society of Petroleum Engineers Journal*, *22*(02), 245–258. <http://doi.org/10.2118/8997-PA>
- Ding, M., & Kantzas, A. (2004). Capillary Number Correlations for Gas-Liquid Systems. In *Canadian International Petroleum Conference.* Petroleum Society of Canada. <http://doi.org/10.2118/2004-062>
- DoE. (2016). Department of Energy, Enhanced Oil Recovery |. Retrieved from <http://energy.gov/fe/science-innovation/oil-gas-research/enhanced-oil-recovery>
- Ekserova, D. R. (Dochi R., & Krugliakov, P. M. (Petr M. (1998). *Foam and foam films : theory, experiment, application.* Elsevier.
- Ettinger, R. A., & Radke, C. J. (1992). Influence of Texture on Steady Foam Flow in Berea Sandstone. *SPE Reservoir Engineering*, *7*(01), 83–90. <http://doi.org/10.2118/19688-PA>
- Falls, A. H., Hirasaki, G. J., Patzek, T. W., Gauglitz, D. A., Miller, D. D., & Ratulowski, T. (1988). Development of a Mechanistic Foam Simulator: The Population Balance and Generation by Snap-Off. *SPE Reservoir Engineering*, *3*(03), 884–892. <http://doi.org/10.2118/14961-PA>
- Farajzadeh, R., Andrianov, A., & Zitha, P. L. J. (2010). Investigation of immiscible and miscible foam for enhancing oil recovery. *Industrial and Engineering Chemistry Research*, *49*(4), 1910–1919. <http://doi.org/10.1021/ie901109d>
- Farajzadeh, R., Lotfollahi, M., Eftekhari, a. a., Rossen, W. R., & Hirasaki, G. J. H. (2015). Effect of Permeability on Implicit-Texture Foam Model Parameters and the Limiting Capillary Pressure. *Energy & Fuels*, *29*(5), 3011–3018. <http://doi.org/10.1021/acs.energyfuels.5b00248>
- Fayers, F. (1989). Extension of Stone's method 1 and conditions for real characteristics in three-phase flow. *SPE Res Eng*, *4*(4), 437–445. SPE-16965-PA.

<http://doi.org/10.2118/16965-PA>

- Gauchet, S., Durand, M., & Langevin, D. (2014). Foam drainage. Possible influence of a non-newtonian surface shear viscosity. *Journal of Colloid and Interface Science*. <http://doi.org/10.1016/j.jcis.2014.12.060>
- Gauglitz, P. A., Friedmann, F., Kam, S. I., & Rossen, W. . . (2002). Foam generation in homogeneous porous media. *Chemical Engineering Science*, 57(19), 4037–4052. [http://doi.org/10.1016/S0009-2509\(02\)00340-8](http://doi.org/10.1016/S0009-2509(02)00340-8)
- Gerbacia, W., & McMillen, T. J. (1982). Oil-Recovery Surfactant Formulation Development Using Surface Design Experiments. *Society of Petroleum Engineers Journal*, 22(02), 237–244. <http://doi.org/10.2118/8878-PA>
- Gozalpour, F., Ren, S. R., & Tohidi, B. (2005). CO2 EOR and Storage in Oil Reservoir, 60(3), 537–546. <http://doi.org/10.2516/ogst:2005036>
- Guo, H., Zitha, P., Faber, R., & Buijse, M. (2012). A Novel Alkaline/Surfactant/Foam Enhanced Oil Recovery Process. *SPE Journal*, 17(4), 19–21. <http://doi.org/10.2118/145043-PA>
- Harkins, W. D. (1941). A General Thermodynamic Theory of the Spreading of Liquids to Form Duplex Films and of Liquids or Solids to Form Monolayers. *The Journal of Chemical Physics*, 9(7), 552. <http://doi.org/10.1063/1.1750953>
- Healy, R. N., Reed, R. L., & Stenmark, D. G. (1976). Multiphase Microemulsion Systems. *Society of Petroleum Engineers Journal*, 16(03), 147–160. <http://doi.org/10.2118/5565-PA>
- Hirasaki, G. J., & Lawson, J. B. (1985). Mechanisms of Foam Flow in Porous Media: Apparent Viscosity in Smooth Capillaries. *Society of Petroleum Engineers Journal*, 25(02), 176–190. <http://doi.org/10.2118/12129-PA>
- Hirasaki, G. J., Miller, C. A., Pope, G. A., & Jackson, R. E. (2004). *SURFACTANT BASED ENHANCED OIL RECOVERY AND FOAM MOBILITY CONTROL*. Pittsburgh, PA, and Morgantown, WV. Retrieved from http://www.researchgate.net/publication/242127259_SURFACTANT_BASED_ENHANCED_OIL_RECOVERY_AND_FOAM_MOBILITY_CONTROL
- Hiraski, G. J. (1989). The Steam-Foam Process. *Journal of Petroleum Technology*, 41(05), 449–456. <http://doi.org/10.2118/19505-PA>
- Holm, L. W. (2013). Foam Injection Test in the Siggins Field, Illinois. *Journal of Petroleum Technology*, 22(12), 1499–1506. <http://doi.org/10.2118/2750-PA>
- Hosseini-Nasab, S. M., Padalkar, C., Battistutta, E., & Zitha, P. L. J. (2016). Mechanistic Modeling of the Alkaline/Surfactant/Polymer Flooding Process under Sub-optimum Salinity Conditions for Enhanced Oil Recovery. *Industrial and Engineering Chemistry Research*, 55(24), 6875–6888. <http://doi.org/10.1021/acs.iecr.6b01094>
- Hosseini-Nasab, S. M., Zitha, P. L. J., Mirhaj, S. A., & Simjoo, M. (2016). A New Chemical-Enhanced Oil Recovery Method? *Colloids and Surfaces A: Physicochemical and Engineering Aspects*, 507, 89–95. <http://doi.org/10.1016/j.colsurfa.2016.07.087>
- Huh, C. (1979). Interfacial tensions and solubilizing ability of a microemulsion phase that coexists with oil and brine. *Journal of Colloid and Interface Science*, 71(2), 408–426. [http://doi.org/10.1016/0021-9797\(79\)90249-2](http://doi.org/10.1016/0021-9797(79)90249-2)
- Huh, D. G., & Handy, L. L. (1989). Comparison of Steady- and Unsteady- State Flow of Gas and Foaming Solution in Porous Media. *Spe*, (February), 77–84.

- <http://doi.org/10.2118/15078-PA>
- Ibrahim, Z. B., Manap, A. A. A., Hamid, P. A., Hon, V. Y., Lim, P. H., & Wyatt, K. (2006). Laboratory Aspect of Chemical EOR Processes Evaluation for Malaysian Oilfields. In *SPE Asia Pacific Oil & Gas Conference and Exhibition*. Society of Petroleum Engineers. <http://doi.org/10.2118/100943-MS>
- IEA - World Energy Outlook. (2016). Retrieved from <http://www.worldenergyoutlook.org/>
- Iglauer, S., Wu, Y., Shuler, P., Tang, Y., & Goddard, W. (2010). Alkyl Polyglycoside/1-naphthol Formulations with Ultra-low Interfacial Tensions Against N-octane for Enhanced Oil Recovery. *Proceedings of SPE EUROPEC/EAGE Annual Conference and Exhibition*, 1–11. <http://doi.org/10.2118/130404-MS>
- Jacquard, P. (1991). Improved oil recovery in the global energy perspective. <http://doi.org/10.3997/2214-4609.201411291>
- Johannesen, E. B., & Graue, A. (2007). Mobilization of Remaining Oil - Emphasis on Capillary Number and Wettability. In *International Oil Conference and Exhibition in Mexico*. Society of Petroleum Engineers. <http://doi.org/10.2118/108724-MS>
- Johannessen, A. M., & Spildo, K. (2013). Enhanced Oil Recovery (EOR) by Combining Surfactant with Low Salinity Injection. *Energy & Fuels*, 27(10), 5738–5749. <http://doi.org/10.1021/ef400596b>
- Jones, S. A., Laskaris, G., Vincent-Bonnieu, S., Farajzadeh, R., & Rossen, W. R. (2016). Effect of surfactant concentration on foam: From coreflood experiments to implicit-texture foam-model parameters. *Journal of Industrial and Engineering Chemistry*. <http://doi.org/10.1016/j.jiec.2016.03.041>
- Kam, S. I., & Rossen, W. R. (2003). A Model for Foam Generation in Homogeneous Media. *SPE Journal*, 8(04), 417–425. <http://doi.org/10.2118/87334-PA>
- Kang, W., Liu, S., Meng, L., Cao, D., & Fan, H. (2010). A Novel Ultra-low Interfacial Tension Foam Flooding Agent to Enhance Heavy Oil Recovery. *Proceedings of SPE Improved Oil Recovery Symposium*. <http://doi.org/10.2118/129175-MS>
- Kapetas, L., Vincent-Bonnieu, S., Farajzadeh, R., Eftekhari, a. a., Mohd-Shafian, S. R., Kamarul Bahrim, R. Z., & Rossen, W. R. (2015). Effect of Permeability on Foam-model parameters - An Integrated Approach from Coreflood Experiments through to Foam Diversion Calculations. *IOR 2015 – 18th European Symposium on Improved Oil Recovery*, (April 2015), 14–16. <http://doi.org/10.3997/2214-4609.201412124>
- Karakashev, S. I., Georgiev, P., & Balashev, K. (2012). Foam production--ratio between foaminess and rate of foam decay. *Journal of Colloid and Interface Science*, 379(1), 144–7. <http://doi.org/10.1016/j.jcis.2012.04.048>
- Kazemi Nia Korrani, A., Sepehrnoori, K., & Delshad, M. (2014). A Comprehensive Geochemical-Based Approach to Quantify the Scale Problems. *SPE International Symposium and Exhibition on Formation Damage Control*. <http://doi.org/10.2118/168196-MS>
- Kazempour, M., Manrique, E. J., Alvarado, V., Zhang, J., & Lantz, M. (2013). Role of active clays on alkaline–surfactant–polymer formulation performance in sandstone formations. *Fuel*, 104, 593–606. <http://doi.org/10.1016/j.fuel.2012.04.034>
- Khatib, Z. I., Hirasaki, G. J., & Falls, A. H. (1988). Effects of Capillary Pressure on Coalescence and Phase Mobilities in Foams Flowing Through Porous Media. *SPE Reservoir Engineering*, 3(03), 919–926. <http://doi.org/10.2118/15442-PA>

- Khoshnevis Gargar, N., Mailybaev, A. A., Marchesin, D., & Bruining, H. (2014). Effects of water on light oil recovery by air injection. *Fuel*, *137*, 200–210. <http://doi.org/10.1016/j.fuel.2014.07.083>
- Koczo, K., Lobo, L. ., & Wasan, D. . (1992). Effect of oil on foam stability: Aqueous foams stabilized by emulsions. *Journal of Colloid and Interface Science*, *150*(2), 492–506. [http://doi.org/10.1016/0021-9797\(92\)90218-B](http://doi.org/10.1016/0021-9797(92)90218-B)
- Kokal, S., & Al-Kaabi, a. (2010). Enhanced oil recovery: challenges and opportunities. *Global Energy Solutions*, 64–69. Retrieved from http://www.world-petroleum.org/docs/docs/publications/2010yearbook/P64-69_Kokal-Al_Kaabi.pdf
- Kovscek, A. R., Chen, Q., & Gerritsen, M. (2010). Modeling Foam Displacement With the Local-Equilibrium Approximation: Theory and Experimental Verification. *SPE Journal*, *15*(01), 171–183. <http://doi.org/10.2118/116735-PA>
- Kovscek, A. R., Patzek, T. W., & Radke, C. J. (1995). A mechanistic population balance model for transient and steady-state foam flow in Boise sandstone. *Chemical Engineering Science*, *50*(23), 3783–3799. [http://doi.org/10.1016/0009-2509\(95\)00199-F](http://doi.org/10.1016/0009-2509(95)00199-F)
- Kovscek, A. R., & Radke, C. J. (1994). Fundamentals of Foam Transport in Porous Media (pp. 115–163). <http://doi.org/10.1021/ba-1994-0242.ch003>
- Kovscek, A. R., Tadeusz, W. P., & Radke, C. J. (1997). Mechanistic Foam Flow Simulation in Heterogeneous and Multidimensional Porous Media. *SPE Journal*, *2*(04), 511–526. <http://doi.org/10.2118/39102-PA>
- Lake, L. W., Russell, J., & Rossen, B. (2014). Fundamentals of Enhanced Oil Recovery. Retrieved February 1, 2015, from http://txessarchive.org/documents/J_EOR_ppt.pdf
- Lange, E. A., & Huh, C. (2013). A Polymer Thermal Decomposition Model and Its Application in Chemical EOR Process Simulation. In *SPE/DOE Improved Oil Recovery Symposium*. Society of Petroleum Engineers. <http://doi.org/10.2118/27822-MS>
- Lashgari, H. R., Sepehrnoori, K., & Delshad, M. (2015). Modeling of Low-Tension Surfactant-Gas Flooding Process in a Four-Phase Flow Simulator, (1973).
- Lau, H. C., & O'Brien, S. M. (1988). Effects of Spreading and Nonspreading Oils on Foam Propagation Through Porous Media. *SPE Reservoir Engineering*, (August), 893–896.
- Lavergne, A., Zhu, Y., Pizzino, A., Molinier, V., & Aubry, J. M. (2011). Synthesis and foaming properties of new anionic surfactants based on a renewable building block: Sodium dodecyl isosorbide sulfates. *Journal of Colloid and Interface Science*, *360*(2), 645–653. <http://doi.org/10.1016/j.jcis.2011.04.110>
- Lawson, J. B., & Reisberg, J. (1980). Alternate Slugs Of Gas And Dilute Surfactant For Mobility Control During Chemical Flooding. In *SPE/DOE Enhanced Oil Recovery Symposium*. Society of Petroleum Engineers. <http://doi.org/10.2118/8839-MS>
- Levitt, D. B., Chamerois, M., Bourrel, M., France, T. P., Gauer, P., Morel, D., & Total, E. (2011). The Effect of a Non-negative Salinity Gradient on ASP Flood Performance, (2010).
- Levitt, D. B., Jackson, A. C., Heinson, C., Britton, L. N., Malik, T., Dwarakanath, V., & Pope, G. A. (2009). Identification and Evaluation of High-Performance EOR Surfactants. *SPE/DOE Symposium on Improved Oil Recovery*, (April), 243–253. <http://doi.org/10.2118/100089-MS>
- Li, R. F., Hirasaki, G. J., Miller, C. a., & Masalmeh, S. K. (2012). Wettability Alteration and Foam Mobility Control in a Layered , 2D Heterogeneous Sandpack. *SPE Journal*,

- (December), 1207–1220. <http://doi.org/10.2118/141462-MS>
- Li, R. F., Yan, W., Liu, S., Hirasaki, G. J., & Miller, C. A. (2010). Foam Mobility Control for Surfactant Enhanced Oil Recovery. *SPE Journal*, 15(November 2009), 20–23. <http://doi.org/10.2118/113910-PA>
- Li, R. F., Yan, W., Liu, S., Hirasaki, G. J., Miller, C. A., & Oil, O. (2010). Foam Mobility Control for Surfactant Enhanced Oil Recovery. *SPE Journal*, 15(November 2009), 20–23. <http://doi.org/10.2118/113910-PA>
- Liyanage, P., Solairaj, S., Pinnawala Arachchilage, G. W. P., Linnemeyer, H., Kim, D. H., Weerasooriya, U., & Pope, G. (2012). Alkaline Surfactant Polymer Flooding using a Novel Class of Large Hydrophobe Surfactants. *Proceedings of SPE Improved Oil Recovery Symposium*, 1–17. <http://doi.org/10.2118/154274-MS>
- Lotfollahi, M., Varavei, A., Delshad, M., Farajzadeh, R., & Pope, G. a. (2015). A Four-Phase Flow Model to Simulate Chemical EOR with Gas. *SPE Reservoir Simulation Symposium*. <http://doi.org/10.2118/173322-MS>
- Ma, K., Liontas, R., Conn, C. a., Hirasaki, G. J., & Biswal, S. L. (2012). Visualization of improved sweep with foam in heterogeneous porous media using microfluidics. *Soft Matter*, 8(41), 10669. <http://doi.org/10.1039/c2sm25833a>
- Ma, K., Lopez-salinas, J. L., Puerto, M. C., Miller, C. A., Biswal, S. L., & Hirasaki, G. J. (2013). Estimation of Parameters for the Simulation of Foam Flow through Porous Media . Part 1 : The Dry-Out Effect.
- Ma, K., Ren, G., Mateen, K., Morel, D., & Cordelier, P. (2015). Modeling Techniques for Foam Flow in Porous Media. *SPE Journal*, (June).
- Mai, A., & Kantzas, A. (2009). Heavy Oil Waterflooding: Effects of Flow Rate and Oil Viscosity. *Journal of Canadian Petroleum Technology*, 48(03), 42–51. <http://doi.org/10.2118/09-03-42>
- Maldal, T., Jakobsen, S. R., Alvestad, J., & Arland, K. S. (1999). Relationship between remaining oil saturation after waterflooding and rock/flow properties at laboratory and reservoir scale. *Petroleum Geoscience*, 5(1), 31–35. <http://doi.org/10.1144/petgeo.5.1.31>
- Manichand, R. N., & Seright, R. (2014). Field vs. Laboratory Polymer-Retention Values for a Polymer Flood in the Tambaredjo Field. *SPE Reservoir Evaluation & Engineering*, 17(03), 314–325. <http://doi.org/10.2118/169027-PA>
- Mannhardt, K., Novosad, J. J., & Schramm, L. L. (2000). Comparative Evaluation of Foam Stability to Oil. *SPE Reservoir Evaluation & Engineering*, 3(01), 23–34. <http://doi.org/10.2118/60686-PA>
- McGuire, P. L., & Holt, B. M. (2003). Unconventional Miscible EOR Experience at Prudhoe Bay: A Project Summary. *SPE Reservoir Evaluation & Engineering*, 6(01), 17–27. <http://doi.org/10.2118/82140-PA>
- Mohammadi, H., Delshad, M., & Pope, G. A. (2009). Mechanistic Modeling of Alkaline / Surfactant / Polymer Floods, (August).
- Mohammadi, S. S., Van Slyke, D. C., & Ganong, B. L. (1989). Steam-Foam Pilot Project in Dome-Tumbador, Midway-Sunset Field. *SPE Reservoir Engineering*, 4(01), 7–16. <http://doi.org/10.2118/16736-PA>
- Myers, D. (2005). *Surfactant Science and Technology*. Hoboken, NJ, USA: John Wiley & Sons, Inc. <http://doi.org/10.1002/047174607X>

- Nelson, R. C., Lawson, J. B., Thigpen, D. R., & Stegemeier, G. L. (1984). Cosurfactant-Enhanced Alkaline Flooding.
- Nguyen, Q. P., Currie, P. K., Buijse, M., & Zitha, P. L. J. (2007). Mapping of foam mobility in porous media. *Journal of Petroleum Science and Engineering*, 58(1-2), 119–132. <http://doi.org/10.1016/j.petrol.2006.12.007>
- Nguyen, Q. P., Rossen, W. R., Zitha, P. L. J., & Currie, P. K. (2005). Determination of Gas Trapping With Foam Using X-Ray Computed Tomography and Effluent Analysis. *SPE Journal*, 14(02), 222–236. <http://doi.org/10.2118/94764-PA>
- Nikolov, A. D., Wasan, D. T., Huang, D. W., & Edwards, D. A. (2013). The Effect of Oil on Foam Stability: Mechanisms and Implications for Oil Displacement by Foam in Porous Media. In *SPE Annual Technical Conference and Exhibition*. Society of Petroleum Engineers. <http://doi.org/10.2118/15443-MS>
- OGJ Survey. (2014). OGJ Survey. Retrieved January 13, 2017, from <http://www.ogj.com/articles/print/volume-112/issue-4/special-report-eor-heavy-oil-survey/2014-worldwide-eor-survey.html>
- Ogolo, N. A., Olafuyi, O. A., & Onyekonwu, M. O. (2012). Enhanced Oil Recovery Using Nanoparticles. In *SPE Saudi Arabia Section Technical Symposium and Exhibition*. Society of Petroleum Engineers. <http://doi.org/10.2118/160847-MS>
- Ojukwu, C., Onyekonwu, M. O., Ogolo, N. A., & Ubani, C. (2013). Alkaline Surfactant Polymer (Local) Enhanced Oil Recovery: An Experimental Approach. In *SPE Nigeria Annual International Conference and Exhibition*. Society of Petroleum Engineers. <http://doi.org/10.2118/167529-MS>
- OPEC : World Oil Outlook. (2016). Retrieved from http://www.opec.org/opec_web/en/publications
- Pagliaro, M., & Rossi, M. (2008). *Future of Glycerol*. Cambridge: Royal Society of Chemistry. <http://doi.org/10.1039/9781847558305>
- Petkova, R., Tcholakova, S., & Denkov, N. D. (2012). Foaming and foam stability for mixed polymer-surfactant solutions: effects of surfactant type and polymer charge. *Langmuir : The ACS Journal of Surfaces and Colloids*, 28(11), 4996–5009. <http://doi.org/10.1021/la3003096>
- Pitts, M. J., Dowling, P., Wyatt, K., Surkalo, H., Adams, C., & Oil, C. (2006). Alkaline-Surfactant-Polymer Flood of the Tanner Field, (September 1997), 1–5.
- Qi, Q., Gu, H., Li, D., & Dong, L. (2000). The Pilot Test of ASP Combination Flooding in Karamay Oil Field. In *International Oil and Gas Conference and Exhibition in China*. Society of Petroleum Engineers. <http://doi.org/10.2118/64726-MS>
- Quintero, L., Jones, T. A., Pietrangeli, G., & Hughes, B. (2011). Phase Boundaries of Microemulsion Systems Help to Increase Productivity. In *SPE European Formation Damage Conference held in Noordwijk, The Netherlands, 7–10 June*.
- Robinson, J. V., & Woods, W. W. (1948). A method of selecting foam inhibitors. *Journal of the Society of Chemical Industry*, 67(9), 361–365. <http://doi.org/10.1002/jctb.5000670908>
- Roehl, P. O., & Choquette, P. W. (1985). *Carbonate Petroleum Reservoirs* | Springer. Retrieved January 26, 2015, from <http://www.springer.com/us/book/9781461250401>
- Rossen, W. ., & Gauglitz, P. . (1990). Percolation Theory of Foam in Porous Media. *Spe*, 36(8). <http://doi.org/10.2118/20239-MS>

- Rossen, W. R. (1996). "Foams in Enhanced Oil Recovery," in R. K. Prud'homme and S. Khan, ed., *Foams: Theory, Measurements and Applications*. Marcel Dekker, New York.
- Rossen, W. R., & Boeije, C. S. (2015). Fitting Foam-Simulation-Model Parameters to Data: II. Surfactant-Alternating-Gas Foam Applications. *Spe Reservoir Evaluation & Engineering*, 18(2), 273–283. Retrieved from <Go to ISI>://WOS:000356157200013
- Rossen, W. R., & Bruining, J. (2007). Foam Displacements with Multiple Steady States. *SPE Journal*, 12(01), 5–18. <http://doi.org/10.2118/89397-PA>
- Rossen, W. R., & Shen, C. (2007). Gravity Segregation in Gas-Injection IOR. In *SPE EUROPEC/EAGE Conference and Exhibition*. Society of Petroleum Engineers. <http://doi.org/10.2118/107262-MS>
- Rossen, W. R., & Wang, M. W. (1999). Modeling Foams for Acid Diversion. *SPE Journal*, 4(02), 92–100. <http://doi.org/10.2118/56396-PA>
- Rossi, M. P. and M. (2008). Glycerol: Properties and Production. In *The Future of Glycerol: New Uses of a Versatile Raw Material* (pp. 1–18). Springer.
- Sagar, N. S., & Castanier, L. M. (1997). *Oil-foam interactions in a micromodel*. U.S. Department for Energy Assistant Secretary for Fossil Energy DE-FG22-96BC 14994. Pittsburgh, PA, and Morgantown, WV. Retrieved from <http://65.54.113.26/Publication/60740022/oil-foam-interactions-in-a-micromodel>
- Schlumberger. (2015). Enhanced Oil Recovery (EOR) | Schlumberger. Retrieved from http://www.slb.com/services/technical_challenges/enhanced_oil_recovery.aspx
- Schramm, L. L., & Novosad, J. J. (1990). Micro-visualization of foam interactions with a crude oil. *Colloids and Surfaces*, 46(1), 21–43. [http://doi.org/10.1016/0166-6622\(90\)80046-7](http://doi.org/10.1016/0166-6622(90)80046-7)
- Schramm, L. L., & Novosad, J. J. (1992). The destabilization of foams for improved oil recovery by crude oils: Effect of the nature of the oil. *Journal of Petroleum Science and Engineering*, 7(1-2), 77–90. [http://doi.org/10.1016/0920-4105\(92\)90010-X](http://doi.org/10.1016/0920-4105(92)90010-X)
- Schramm, L. L., & Smith, D. H. (1996). *Foams: Fundamentals and Applications in the Petroleum Industry*. American Chemical Society (Vol. 10). American Chemical Society. <http://doi.org/10.1021/ef950077m>
- Schramm, L. L., Turta, A. T., & Novosad, J. J. (1993). Microvisual and Coreflood Studies of Foam Interactions With a Light Crude Oil. *SPE Reservoir Engineering*, 8(03), 201–206. <http://doi.org/10.2118/20197-PA>
- Schulze-Schlarman, J., Buchavzov, N., & Stubenrauch, C. (2006). A disjoining pressure study of foam films stabilized by tetradecyl trimethyl ammonium bromide C14TAB. *Soft Matter*, 2(7), 584. <http://doi.org/10.1039/b602975b>
- Sheng, J. (2011). Modern Chemical Enhanced Oil Recovery. Retrieved February 5, 2015, from <http://www.elsevier.com/books/modern-chemical-enhanced-oil-recovery/sheng/978-1-85617-745-0>
- Sheng, J. (2013). A Comprehensive Review of Alkaline-Surfactant-Polymer (ASP) Flooding, (April).
- Sheng, J. (2014). A comprehensive review of alkaline-surfactant-polymer (ASP) flooding. *Asia-Pacific Journal of Chemical Engineering*, 9, 471–489. <http://doi.org/10.1002/apj.1824>
- Simjoo, M., Dong, Y., Andrianov, A., Talanana, M., & Zitha, P. (2012). Novel Insight into

- Foam Mobility Control. *Proceedings of International Petroleum Technology Conference*, (September), 1–15. <http://doi.org/10.2523/15338-MS>
- Simjoo, M., Dong, Y., Andrianov, A., Talanana, M., & Zitha, P. L. J. (2013). CT Scan Study of Immiscible Foam Flow in Porous Media for Enhancing Oil Recovery. *Industrial & Engineering Chemistry Research*, 52(18), 6221–6233. <http://doi.org/10.1021/ie300603v>
- Simjoo, M., & Nguyen, Q. P. (2011). Rheological Transition during Foam Flow in Porous Media.
- Simjoo, M., Rezaei, T., Andrianov, a., & Zitha, P. L. J. (2013). Foam stability in the presence of oil: Effect of surfactant concentration and oil type. *Colloids and Surfaces A: Physicochemical and Engineering Aspects*. <http://doi.org/10.1016/j.colsurfa.2013.05.062>
- Simjoo, M., & Zitha, P. (2013). Effects of Oil on Foam Generation and Propagation in Porous Media. In *SPE Enhanced Oil Recovery Conference*. Society of Petroleum Engineers. <http://doi.org/10.2118/165271-MS>
- Sohrabi, M., & Farzaneh, S. A. (2013). A Review of the Status of Foam Applications in Enhanced Oil Recovery. *Proceedings of 75th EAGE Conference & Exhibition Incorporating SPE EUROPEC 2013*. <http://doi.org/10.2118/164917-MS>
- Spildo, K., Johannessen, A. M., Skauge, A., & Integrated, C. (2012). Low Salinity Waterflood at Reduced Capillarity. In *SPE Improved Oil Recovery Symposium, 14-18 April, Tulsa, Oklahoma, USA*. Society of Petroleum Engineers.
- Srivastava, M., & Nguyen, Q. (2010). Application of Gas for Mobility Control in Chemical EOR in Problematic Carbonate Reservoirs. *Proceedings of SPE Improved Oil Recovery Symposium*. <http://doi.org/10.2118/129840-MS>
- Srivastava, M., Zhang, J., Nguyen, Q., & Pope, G. (2009). A Systematic Study of Alkaline-Surfactant-Gas Injection as an EOR Technique. *Proceedings of SPE Annual Technical Conference and Exhibition*. <http://doi.org/10.2118/124752-MS>
- Stoll, W. M., Shureqi, H., Finol, J., Oman, S. T., Oyemade, S., Kruijf, A. De, ... Ep, S. I. (2011). Alkaline / Surfactant / Polymer Flood: From the Laboratory to the Field, (December).
- Stone, H. L. (1973). Estimation of Three-Phase Relative Permeability and Residual Oil Data. *Journal of Canadian Petroleum Technology*, 12(4), 53–61. <http://doi.org/10.2118/73-04-06>
- Stubenrauch, C., & Klitzing, R. von. (2003). Disjoining pressure in thin liquid foam and emulsion films—new concepts and perspectives. *Journal of Physics: Condensed Matter*, 15(27), R1197–R1232. <http://doi.org/10.1088/0953-8984/15/27/201>
- Su, S. (2012). *Laboratory Investigation of Polymer-flooding, ASP-flooding, and Foam-flooding in Heavy Oil System*. University of CALGARY.
- Szlendak, S. M., Nguyen, N., & Nguyen, Q. P. (2013). Laboratory Investigation of Low-Tension- Gas Flooding for Improved Oil Recovery in Tight Formations. *SPE Journal*, 8–10.
- Tang, S., Tian, L., Lu, J., Wang, Z., Xie, Y., Yang, X., & Lei, X. (2014). A Novel Low Tension Foam Flooding for Improving Post-Chemical-Flood in Shuanghe Oilfield. *SPE Improved Oil Recovery Symposium*, 1–11. <http://doi.org/10.2118/169074-MS>
- Tanzil, D., Hirasaki, G. J., & Miller, C. A. (2002). Conditions for Foam Generation in Homogeneous Porous Media. In *SPE/DOE Improved Oil Recovery Symposium*. Society of Petroleum Engineers. <http://doi.org/10.2118/75176-MS>

- Tovar, F. D., Barrufet, M. A., & Schechter, D. S. (2014). Long Term Stability of Acrylamide Based Polymers during Chemically Assisted CO₂ WAG EOR. In *SPE Improved Oil Recovery Symposium*. Society of Petroleum Engineers. <http://doi.org/10.2118/169053-MS>
- UTCHEM technical documentation. (2011). UTCHEM Technical Documentation: A three-dimensional chemical simulator. Retrieved from Downloaded from
- Veedu, F. K., Delshad, M., & Pope, G. A. (2010). Scaleup Methodology for Chemical Flooding, (September), 19–22.
- Vikingstad, A. K., Skauge, A., Høiland, H., & Aarra, M. (2005). Foam–oil interactions analyzed by static foam tests. *Colloids and Surfaces A: Physicochemical and Engineering Aspects*, 260(1-3), 189–198. <http://doi.org/10.1016/j.colsurfa.2005.02.034>
- Willhite, G. P. (1986). *Waterflooding*. Society of Petroleum Engineers.
- Winsor, P. (1954). *Solvent properties of amphiphilic compounds*. London: Butterworths.
- World Energy Outlook. (2016). *Carbon Capture and Storage: a WEC "*.
- Worthen, A. J., Bagaria, H. G., Chen, Y., Bryant, S. L., Huh, C., & Johnston, K. P. (2013). Nanoparticle-stabilized carbon dioxide-in-water foams with fine texture. *Journal of Colloid and Interface Science*, 391, 142–51. <http://doi.org/10.1016/j.jcis.2012.09.043>
- Wu, W., Pan, J., & Guo, M. (2010). Mechanisms of oil displacement by ASP-foam and its influencing factors. *Petroleum Science*, 7(1), 100–105. <http://doi.org/10.1007/s12182-010-0012-1>
- Wu, Y., Iglauer, S., Shuler, P., Tang, Y., & Goddard, W. a. (2010). Branched Alkyl Alcohol Propoxylated Sulfate Surfactants for Improved Oil Recovery. *Tenside Surfactants Detergents*, 47(3), 152–161. <http://doi.org/10.3139/113.110064>
- Xu, Q., & Rossen, W. R. (2003). Effective viscosity of foam in periodically constricted tubes. *Colloids and Surfaces A: Physicochemical and Engineering Aspects*, 216(1), 175–194. [http://doi.org/10.1016/S0927-7757\(02\)00547-2](http://doi.org/10.1016/S0927-7757(02)00547-2)
- Yerramilli, S. S., Zitha, P. L. J., & Yerramilli, R. C. (2013). Novel Insight into Polymer Injectivity for Polymer Flooding Modeling of Polymer Flow in Porous Media, (2009), 1–23.
- Young, N. R. S. (2011, January 1). New Advancements In Emulsifier Technologies. *Offshore Mediterranean Conference and Exhibition*. Offshore Mediterranean Conference. Retrieved from <https://www.onepetro.org/conference-paper/OMC-2011-089>
- Yuqiang, P., Dehuang, S., & Shaocheng, X. (2008). Experimental study on nitrogen foam flooding to enhance oil recovery in heavy oil reservoir-taking Qinhuangdao 32-6 Oilfield with heavy oil as an example. *Petroleum Geology and Recovery Efficiency*, 59–61.
- Zechner, M., Buchgraber, M., Clemens, T., Gumpenberger, T., Castanier, L. M., & Kovsky, A. R. (2013). Flow of Polyacrylamide Polymers in the Near-Wellbore-Region, Rheological Behavior within Induced Fractures and Near-Wellbore-Area. In *SPE Annual Technical Conference and Exhibition*. Society of Petroleum Engineers. <http://doi.org/10.2118/166085-MS>
- Zechner, M., Clemens, T., Suri, A., & Sharma, M. M. (2014). Simulation of Polymer Injection under Fracturing Conditions - A Field Pilot in the Matzen Field, Austria. In *SPE Improved Oil Recovery Symposium*. Society of Petroleum Engineers. <http://doi.org/10.2118/169043-MS>
- Zhao, P., Jackson, A. C., Britton, C., Kim, D. H., Britton, L. N., Levitt, D. B., & Pope, G. A.

(2008). Development of High-Performance Surfactants for Difficult Oils. In *SPE/DOE Improved Oil Recovery Symposium held in Tulsa, Oklahoma, U.S.A., 19–23 April* .

List of Figures

Fig. 2.1: Schematic of the experimental set-up used to perform the core-flooding experiments. The core-holder was held vertically on the bench of the CT scanner.	20
Fig. 2.2: History match of the pressure drop of foam-quality scan experiment without oil at fixed total superficial velocity ($U_g + U_w$) in Bentheimer core by the LE-IT foam model and the simulation parameters presented in Table 2.5., Numerically simulated behaviour of foam-quality scans at a fixed superficial velocity that are higher and lower superficial velocities than the experimental condition are also shown in this figure.	24
Fig. 2.3: Comparison of numerically calculated and measurement pressure drops of foam flooding in the absence of oil at two different surfactant concentrations. Total superficial velocity and foam quality at injection side of the core was fixed at 4.58 ft/day and 91%, respectively.	25
Fig. 2.4: Comparison of numerically calculated and measured pressure drops and oil recovery factor (OIF) during oil displacement by foam flooding.	29
Fig. 2.5: Comparison of numerically calculated and measured oil-cut by foam flooding.	29
Fig. 2.6: CT images obtained during foam flooding in a core containing water-flooded residual oil (Simjoo & Zitha, 2013). The red colour stands for the water-flooded core including residual oil saturation, and the blue colour indicates the presence of the foam phase. Foam was injected from top to bottom to ensure gravity stable conditions. Foam breakthrough occurred at 0.63 ± 0.02 PV.	30
Fig. 3.1: Schematic of the experimental setup used to perform ASP core-flood experiments. .	40
Fig. 3.2: Three-dimensional (3D) image from the cross section of core obtained by the medical computed tomography (CT) scan apparatus.	40
Fig. 3.3: Simulated and measured solubilization ratio of oil and water versus salinity for	

surfactant phase behaviour tests.	44
Fig. 3.4: Viscosity of polymer of ASP slug and polymer drive for the 1450 ppm polymer concentration at salinity of 1.98 wt% NaCl, for two different temperatures.....	46
Fig. 3.5: Relative permeability of the water and oil phases for ASP flooding in under-optimum conditions, in comparison to relative permeabilities of water flooding and optimum salinity (Type III) ASP flooding.....	48
Fig. 3.6: Oil and water relative permeability ratio for under-optimum(Type II-) ASP flooding against water flooding and optimum condition (Type III) of ASP flooding	48
Fig. 3.7: Residual oil saturation (S_{or}) and connate water saturation (S_{wc}), as a function of trapping number at high and low capillary numbers. Capillary desaturation curves (CDCs) used in the simulations are shown.....	50
Fig. 3.8: Comparison of the pressure drop between the simulation results and the laboratory data.....	50
Fig. 3.9: Recovery history obtained from simulation and experimental data for oil cut production and cumulative oil. Chemical breakthrough occurred at 0.8 PV.....	51
Fig. 3.10: Comparison of calculated carbonate, surfactant concentration and pH profiles at effluents with laboratory data.	52
Fig. 3.11: Comparison of history plots of simulated pH, carbonate concentration, oil saturation and surfactant concentration comparable at effluents. Concentration normalized at a factor of 100%.....	53
Fig. 3.12: Calculated effective salinity and surfactant concentration over pore volumes (PV) at effluent.	54
Fig. 3.13: Progression of effective salinities at 0.1 PV, 0.48 PV, and 1 PV along the core.	55
Fig. 3.14: Interfacial tension and effective salinity profiles at 0.1 PV (left image) 0.48 PV (right image)	55
Fig. 3.15: Effect of the ASP slug size on cumulative oil recovery (% of OIIP).	57
Fig. 3.16: Effect of surfactant concentration on cumulative oil recovery factor (% of OIIP) ..	58
Fig. 3.17: Cumulative oil recovery at different ASP slug sizes and surfactant concentrations	59
Fig. 3.18: Comparison of the profile of the oil-cut recovered for cases 2A and 2E with the	

original simulation (Case 2C).....	60
Fig. 4.1: Phase behaviour of IOS and n-hexadecane with the glass tube salinity scan method. Salinity (NaCl) varies from left to right 1.0 to 6.0 weight per cent in the surfactant solution....	72
Fig. 4.2: Photograph of the spinning drop tensiometer with temperature controller of the cell with capillary diameter 2.5 mm. Measuring range in IFT measurement is from 10^{-5} mN/m. Rotational speed up to 15,000 rpm (optionally up to 20,000).....	72
Fig. 4.3: Schematic representation of the spinning drop method.....	73
Fig. 4.4: Schematic representation and snapshot of the Foam Scan set-up showing the mass flowmeter to control the air flow, and the optical camera for monitoring the height of foam column to determine the foam volume. Liquid volume in the foam structure was obtained by the conductivity measurement along the glass column.	74
Fig. 4.5: Solubilization ratio of oil and water for systems containing 0.5 wt% IOS surfactant solution contacting hexadecane model oil with a variation of NaCl concentration. Dotted line: connecting water phase solubilization ratio; dashed line: connecting oil phase solubilization ratio.....	77
Fig. 4.6: Solubilization ratio of oil and water for systems containing 1.0 wt% IOS surfactant solution contacting hexadecane model oil with a variation of NaCl concentration. Dotted line: connecting water phase solubilization ratio; dashed line: connecting oil phase solubilization ratio.....	78
Fig. 4.7: Oil droplet shapes in the range of IFT values with the aqueous solution of IOS surfactant with salinity and alkali in the capillary tube of a spinning drop tensiometer: (a) relatively low IFT (1 to 5 mN/m) (b) low IFT (1 to 10^{-2} mN/m) (c) ultralow IFT (less than 10^{-2} mN/m).	79
Fig. 4.8: Effect of IOS surfactant concentration in the absence of an oil phase illustrated by a change in the liquid volume of foam during foam generation and after termination of gas sparging as a function of time. The initial liquid volume of the generated foam is 50 cm^3 and the maximum volume of generated foam are illustrated.	80
Fig. 4.9: The change in the liquid volume of foam during foam generation and after termination of gas sparging as a function of time for the various oil saturations (Volume per cent). The initial liquid volume of the generated foam is 50 cm^3 and the maximum volume of generated foam from 1.0 wt% IOS surfactant in the presence of the oil phase using the foam scan is illustrated.	81

Fig. 4.10: Effect of the different oil saturations on the foam maximum density (<i>MD</i>) and foam capacity (<i>FC</i>) of 1 wt% IOS generated foam.	82
Fig. 4.11: Effect of different levels of oil saturations of n-Hexadecane on the foam half-decay time generated by 1.0 wt% IOS.	83
Fig. 4.12: Foam column stabilized by IOS surfactant in the presence of n-hexadecane. The oil phase was coloured red to visualize. The left-hand image was taken at an early time in the foam decay and the right-hand one was taken at a later time. The images confirm that the capability of the generated foam to be tolerant to the oleic phase while drained liquid stayed in the column.	84
Fig. 4.13: Effect of IOS surfactant concentration on the foam half-decay time in the absence and presence of 5.0 volume per cent of n-Hexadecane.	84
Fig. 4.14: Effect of the IOS surfactant concentration on the foaming capacity (<i>FC</i>) in the absence and presence of 5 volume per cent n-Hexadecane. The initial surfactant solution volume of the generated foam is 50 cc and in the case of the presence of n-Hexadecane, oil saturation is 5 volume per cent.	85
Fig. 4.15: Effect of salt (NaCl) and alkali (Na ₂ CO ₃) concentration on the foam half-decay time of 1.0 wt% IOS surfactant.	86
Fig. 4.16: Effect of salt (NaCl) and alkali (Na ₂ CO ₃) concentration on the maximum density (<i>MD</i>) of generated foam with 1.0 wt% IOS surfactant.	86
Fig. 4.17: Foam volume as a function of time for 0.5 wt% IOS foam contacting n-Hexadecane in the absence and presence of naphthenic acid (Decanoic acid). The effect of <i>in-situ</i> soap generation and surface tension on the stability of foam is illustrated.	87
Fig. 5.1: Schematic overview of the core-flooding set-up for foam flow and oil displacement experiment used in CT scan visualization. The core-holder was placed vertically on the table of CT scanner.	97
Fig. 5.2: Total and sectional MRF results along the core from the experiment of co-injection of N ₂ and AS1 surfactant in the absence of oil phase. Foam quality 80% and total velocity of 2.54 ft/day. (section 1: 11cm, section 2: 4.3cm).....	103
Fig. 5.3: Total and sectional MRF results along the core from the experiment of co-injection of N ₂ and AS2 surfactant in the absence of oil phase. Foam quality 80% and total velocity of 2.54 ft/day. (section 1: 11cm, section 2: 4.3cm).....	103

- Fig. 5.4:** Total and sectional MRF results along the core from the experiment of co-injection of N_2 and AS3 surfactant in the absence of oil phase. Foam quality 80% and total velocity of 2.54 ft/day. (section 1: 11cm, section 2: 4.3cm)104
- Fig. 5.5:** CT images obtained during co-injection of N_2 and of ASF chemical agent (AS3). Foam flow was studied in a single core of Bentheimer sandstone. First sharp foam front advances through the core after about 0.8 PV injection. Sharp front of generated foam is evident of stable foam displacement in the core.105
- Fig. 5.6:** Gas saturation profiles taken at every vertical position throughout the core before and after foam breakthrough obtained from the CT images shown in Fig. 5.5. Foam quality at inlet face of the core was 80%. A rapid in-situ foam generation and fairly piston-like front for the gas saturation propagation were observed.....106
- Fig. 5.7:** Pressure drop profiles during primary drainage over the core and different section of the core (section 1: 11cm, section 2: 4.3cm and section 3: 4.75cm). Oil was injected at 0.5 cm^3/min under gravity stable conditions. The initial jump in the pressure drop profiles corresponds to the entry capillary pressure.107
- Fig. 5.8:** Displacement profile during primary drainage (oil injection) with injection direction from top to bottom. Water phase (blue colour) was displaced by oil (light green).....108
- Fig. 5.9:** Oil saturation profile for oil injection as a primary drainage obtained from the corresponding CT images shown in Fig. 5.8. Oil was injected from the top of the core, which is located on the left side of the figure. The average oil saturation at the end of primary drainage was 0.80 ± 0.02108
- Fig. 5.10:** Total and sectional pressure drop profile during water flooding at 0.5 cm^3/min during the first two pore volumes injected. Water breakthrough coincides with the time at which pressure drop obtains a maximum value.109
- Fig. 5.11:** Displacement profile during gravity stable water flooding (imbibition) with injection direction from the bottom to the top. Oil production by water flooding is evident by a colour change from light green to blue.....110
- Fig. 5.12:** Profile of oil saturation distribution for water flooding obtained from the corresponding CT images given in Fig. 5.11. Brine was injected from the bottom of the core, which is located on the left side of the figure. The average oil saturation at the end of water flooding was 0.4 ± 0.02111

Fig. 5.13: Total and sectional MRF results along the core from the experiment of co-injection of N ₂ and AS1 surfactant solution in the presence of remaining oil after water flooding. Foam quality and total velocity of 2.5 ft/day.....	112
Fig. 5.14: Total and sectional MRF results along the core from the experiment of co-injection of N ₂ and AS2 surfactant in the presence of remaining oil after water flooding. Foam quality and total velocity of 2.5 ft/day.....	112
Fig. 5.15: Total and sectional MRF results along the core from the experiment of co-injection of N ₂ and AS3 surfactant solution in the presence of remaining oil after water flooding. Foam quality of 80% and total velocity of 2.5 ft/day.....	113
Fig. 5.16: CT images obtained during AS3 foam flooding. Foam breakthrough occurred at 0.76 PV \pm 0.03.....	114
Fig. 5.17: Gas saturation profiles taken at every vertical position throughout the core before and after foam breakthrough obtained from the CT images shown in Fig. 5.16.....	115
Fig. 5.18: Oil cut during foam flooding with different alkali-surfactant formulations (AS1, AS2 and AS3). Effect of IFT reduction on fraction flow of oil recovery can be seen. The first oil peaks are corresponding to oil bank formation.....	117
Fig. 5.19: Incremental oil recovery during foam flooding for different surfactant concentrations. Increased cumulative oil recovery was observed for lower IFT foam flooding.....	117
Fig. 5.20: Fluids at the outlet of the core for the AS1 foam (left image) and AS3 foam (right image). Oil is coloured red to visualize. Produced oil at the effluent of AS1 foam appearing more as an emulsion with surfactant solution. Clean oil is much more for AS3 foam. Larger liquid volume in the right column, is because of longer surfactant-preflush.....	118
Fig. 6.1: Schematic of flow process and setup used for core-flooding experiments. The setup consists of four major parts: a test unit (core sample and core holder), measuring unit (pressure transducers), injection unit (pumps), and data acquisition system.....	126
Fig. 6.2: Viscosity of glycerol/water mixture in the range of 1-60 cP as its concentration increases up to 90% weight percent. Interfacial tension (IFT) between the water/glycerol solution and n-hexadecane (oleic phase) slightly varies from 46 to 43 mN/m. The uncertainty of the measured viscosity and IFT data were within \pm 0.05 and \pm 0.1, respectively.....	131
Fig. 6.3: Surface tension between air and different surfactant mixtures (1:1 AOS:FC)	

concentration. CMC of surfactant solution is 5×10^{-3} weight percent. The uncertainty of the measured surface tension data was within ± 0.1131

Fig. 6.4: (a) CT images and (b) corresponding oil saturation profiles, during different stages of core-flooding. The core was water-flooded by brine after primary drainage. Then it was flooded with a water/glycerol mixture containing 85 wt% of glycerol. Finally, it was flooded with surfactant/water/glycerol containing 85 wt% of glycerol and the following surfactant concentrations: I) 0.10 wt%, II) 0.5 wt% and III) 1.0 wt%. The average residual oil saturation at the end of surfactant-glycerol flooding was 0.15. The accuracy of the measured fluid saturations error was within ± 2 %.133

Fig. 6.5: Capillary Desaturation Curve (CDC) for the Bentheimer sandstone with two different procedures: 1) The blue and red curves are according to procedure A, which was stated in Section 2.3 and in Table 4: Water flooding \rightarrow Water+Glycerol solution injection \rightarrow Water+Glycerol+AOS:FC solution injection. 2) The green curve is according to procedure B (mentioned in Section 2.3): Water flooding \rightarrow AOS:FC solution injection \rightarrow Water+Glycerol+AOS:FC solution injection. CT images and oil saturation profiles of the first scenario (A) of the construction of CDC were illustrated in Fig. 4. The accuracy of the measured residual oil saturation error was within ± 2 %135

List of Tables

Table 2.1: Properties of the materials used to conduct the experiments at the ambient.....	19
Table 2.2: Physical properties of the core samples used in the	19
Table 2.3: Overview of the experimental procedure used for the foam flooding experiments .	21
Table 2.4: Input values of rock, fluids and relative permeability parameters in the simulation	23
Table 2.5: Foam model parameters for the numerical modelling of foam flooding	24
Table 2.6: Input values of the parameters of the reservoir model in the simulation	27
Table 2.7: Foam model parameters for numerical simulation of the pressure	28
Table 3.1: Advantages and disadvantages of three types of micro-emulsion systems for surfactant-based flooding EOR	37
Table 3.2: Physical properties and mineralogical composition of Bentheimer sandstone core	39
Table 3.3: Summary of injection profile and basic properties for ASP core-flood experiments	41
Table 3.4: Representative reservoir properties and values of modelling parameters	43
Table 3.5: Input parameters of rock and fluid properties for numerical.....	46
Table 3.6: Simulation parameters and physical properties from the ASP flooding experiment.	47
Table 3.7: Relative permeability and capillary desaturation parameters.....	49
Table 3.8: Effect of the ASP slug size and surfactant slug concentration.....	56
Table 3.9: ASP slug injection design with sensitivity on the combined effect	58
Table 4.1: Foam stability prediction by the negative/positive signs of the E , S	67

Table 4.2: Foam stability prediction by the lamella number theory	68
Table 4.3: Overview of the all surfactant phase behaviour experiments by the	76
Table 4.4: Overview of all the foamability and foam stability experiments by the foam scan method	76
Table 4.5: Experimental data of the surfactant phase behaviour study for three types of chemical	78
Table 4.6: Entering, spreading, and bridging coefficients and lamella number for different ...	88
Table 5.1: Physical properties of the core samples used for core-flood test.....	96
Table 5.2: Setting parameters for the CT Scan measurements	99
Table 5.3: Sequence and conditions of injection step used for the core-flooding experiment	101
Table 5.4: Surfactant formulations used in foam strength test and oil displacement experiments	101
Table 5.5: Summary of incremental oil recovery by co-injection of gas with different chemical solutions.....	118
Table 6.1 Properties of the materials used to conduct the experiments	124
Table 6.2: Properties of the porous sample used for core-flooding experiments	125
Table 6.3: Setting parameters for the CT Scan measurements	127
Table 6.4: Overview of the experiments performed in this study using method A.....	129

Nomenclature

$\bar{C}_{f,W}^{ref}$	reference surfactant concentration
e_c	exponent of capillary number function,
e_o	exponent of oil effect function
e_s	exponent of surfactant-dependent function
f_w	constant of driving foam evolution
f_g	foam quality
F_1	surfactant dependent function
F_2	water saturation dependent function
F_3	capillary number dependent function
F_4	oil saturation dependent function
k	absolute permeability of rock for water phase
k_{ref}	reference permeability
k_{rg}^{gas}	gas relative permeability in absence of foam
k_{rg}^{foam}	gas relative permeability in presence of foam
k_{rw}^0	endpoint of water for water/gas relative permeability
k_{rg}^0	endpoint of gas for water/gas relative permeability
M_{ref}	reference foam mobility reduction factor
n_w	exponent of water for water/gas relative permeability
n_g	exponent of gas for water/gas relative permeability
N_c^{ref}	reference capillary number
P_c^*	limiting capillary pressure
q_g	flow rate of the gas phase
q_l	flow rate of the water phase
S_{wc}	connate water saturation
S_{gr}	residual gas saturation
S_w^*	critical water saturation
S_o^*	critical oil saturation
S_{oi}	initial oil saturation
u	total superficial velocity
∇p	pressure gradient
φ	porosity of rock sample
μ_{app}	Apparent viscosity of displacing fluid (foam)
σ_{wg}	surface tension between gas and surfactant solution
σ_{og}	surface tension between oil and gas
σ_{ow}	surface tension between oil and surfactant solution
μ_w	viscosity of water phase

μ_p^0	polymer viscosity at a zero-shear rate
C_{SEP}	effective salinity
\hat{C}_i	Langmuir isotherm
k_{ref}	reference permeability
r_o	radius of an oil droplet
r_p	radius of Plateau border
ρ_w	density of water phase
ρ_o	density of oleic phase
ω	rotational velocity
CT_{wet}	attenuation coefficients for fully water-saturated core
CT_{dry}	attenuation coefficients for dry core
CT_w	attenuation coefficients of water phase
CT_g	attenuation coefficients of gas phase
CT_o	attenuation coefficients of oleic phase

Acknowledgement

This thesis is the result of nearly five years of work at the Geoscience & Engineering department at the Delft University of Technology (TU Delft). Certainly, I would have never reached the point of finishing my dissertation without the help and support of others, and I would like to take this opportunity to thank them. Firstly, I would like to express my gratitude to my promoter Prof. Dr. Pacelli Zitha for giving me the opportunity to carry out this research and indeed for his guidance from the beginning to the completion of this thesis. My appreciation is also extended to my PhD committee members, Dr. F. Douarche, Prof.dr. H.J. Bertin, Prof.dr. J. Bruining, Prof.dr. W.R. Rossen, Prof.dr.ir. T.J. Heimovaara. Thank you for reviewing my PhD thesis and providing useful comments to improve this dissertation. I am also thankful to Prof. George J. Hirasaki from Rice University, USA, for brilliant suggestions that he provide me to improve the technology of Alkali-Surfactant-Foam (ASF) flooding for Enhanced Oil Recovery (EOR). I am grateful to Dr. Noushine Shahidzadeh, Associate Professor, University of Amsterdam, for the condition that she facilitated to enable me to use the equipment and apparatuses in the Van der Waals-Zeeman Institute- IOP, at the University of Amsterdam.

During my PhD, I also had a great opportunity to work as a visiting researcher at the IFP Energy Nouvel (IFPEN), Paris, France. I would like to specifically thank Dr. Lahcen Nabzar for inviting and hosting me at this institute, that enabled me to perform a part of my PhD thesis in an outstanding professional environment. I had many fruitful discussions with him, and I benefited from his vast knowledge of laboratory experiments on foam flow porous media. I am very grateful to Dr. F. Douarche, Dr. F. Roggero, and Dr. B. Bourbiaux from Reservoir

Simulation Department of IFPEN, France, for their input, ideas and consistent collaboration to conduct the numerical simulations for foam transport in porous media in the absence and presence of oleic phase.

I want to convey my special gratitude to the technical staffs of the Dietz laboratory of the Department of Geoscience and Engineering, TU Delft. I got a great experience by working with the skillful, professional and distinguished technician like Marc Friebel, Ellen Meivogel, Jolanda van Haagen, Karel Heller, Michiel Slob, Henk Asten, Joost van Meel, Wim Verwaal, Jens van den Berg, Guus Lohlefink and Arno Mulder. Thanks very much to all of them for being always helpful and friendly.

I greatly thank Dr. Hassan Mahani and Mr. Hilbert van der Linde from Shell company for their support for conducting interfacial tension (IFT) measurements in the Rock & Fluid Physics Laboratory of Shell Global Solution BV., Rijswijk, the Netherlands. Hassan also provided me his excellent comments on Chapter 4. I also dedicate my acknowledgment to Shell Global Solutions International B.V. for making some of the experimental data available and their permission to publish them. I am grateful to Dr. S. Jones from Technical University of Denmark for careful reading of the Chapter 4, Dr. C. Boeije, the University of Bordeaux, for reviewing Chapter 5, Mr. Cor Kuijvenhoven from Shell Global Solution, Houston, USA, for reading Chapter 6 and providing me with many fruitful suggestions and valuable comments.

I am very thankful to Dr. M. Simjoo for careful reading of Chapter 2 and Chapter 6 and providing me with many fruitful comments, and also many helpful discussion that we had about analyzing X-Ray CT Scan data. My sincere thanks go to Dr. Mohammad Chahardowli who was my genius colleague and supportive friend, and I had excellent scientific discussions with him. I am particularly thankful to C. Padalkar, S.R. van Kuijk, and Dr. E. Battistutta for consistent collaboration and help for the research presented in Chapter 3 of this dissertation.

In addition, I would like to express my appreciation to my friends and colleagues on the TU Delft: Jinyu Tang, Jakolien van der Meer, Rouhi Farajzadeh, Sebastien VincentBonnie, Nikita Lenchenkov, Matei Tene, Eduardo Dias de Barros, Sivash Kahrobaei, Anna Peksa, Bander Alquaimi, Ehsan Eftekhari, Mark Khait, Rahul Fonseca, Leon Kapetas, Sin Jones,

Guanqun Yu, Mohsen Mirzaei-Yeganeh, Matteo Cusini, Ahmed Hussain, Durgesh Kawale, Christian Kosack, Rafael Morae, Rodrigo Salazar, Swej Shah, Boris Boullenger. We had an excellent collaboration and several good discussions together. Thank you very much for your friendship and support. A special thank you to the administrative side of the Geosciences and Engineering department, Anke, Marlijn, Lydia, Margot, Ralf and Hannie for their compassionate supports. I truly appreciate all my friends and colleagues at the petroleum engineering department.

My appreciation extended to my Iranian friends in the Netherlands who have been a great support for me. My special thank goes to my friend, Mohammad Reza Karimian for all of his compassion and supports. With the risk of forgetting someone who I definitely should have mentioned, I would like to thank Mr. Alemi, Madadi, Najafi, Shahbazi, Mehrara, Bakhshandeh, Latifi, Mirzaei, Derakhshani, Abouhamzeh, Abbasi, Saeedi, Fasihi, Ghaemi nia, Bornaee, Tohidian, Ahmadi mehr, Karimian, Behdani, Hesani, Rahimi, Kaviani. I am very grateful of all of you, and I had very beneficial scientific discussions and unforgettable moments with all of you.

Most importantly, I express my highest emotional appreciation to my family, especially my friend. I am extremely grateful to my parents for unconditional love and support. I am really proud of you. In fact, it is beyond my ability to compensate even a small part of your support. You are so supportive and helpful that I cannot express my feeling in only a few sentences. Last, but certainly not least, comes to my lovely wife who provided me great inspiration, infinite support, kindness and encouragement, I would like to express my highest emotional appreciation for all of this, also for her efforts and innovative idea to design the cover of my PhD thesis book.

Seyed Mojtaba Hosseini-Nasab

Delft, March 2017

About the Author

Seyed Mojtaba Hosseini-Nasab received the B.S.E degree and the M.S.E degree in Chemical Engineering (with honors) from Shahid Bahonar University and Tarbiat Modares University, Iran, in 2007 and 2010, respectively. During master research project, he obtained modeling and laboratory experiments experience on “Gas Hydrate Formation Condition in presence of Chemical Inhibitors”. Then, he chose to pursue for PhD program of Petroleum Engineering at Delft University of Technology (TU Delft), The Netherlands. His research interests include Enhanced Oil Recovery (EOR), Numerical Simulation of Multi-Phase Flow, Fluids Conformance Control in Reservoirs, and Formation Damage.

During his PhD program, he spent approximately a half of year in the Institut français du pétrole, IFP Energies Nouvelles (IFPEN), Paris, France, to perform a part of his PhD thesis by collaboration with Reservoir Simulation group of this institute. To perform the laboratory experiments of PhD thesis, he worked in Dietz laboratory of the Department of Geoscience and Engineering of TU Delft; Rock & Fluid Physics Laboratory of Shell Global Solution BV., Rijswijk, the Netherlands; and the Van der Waals-Zeeman Institute- IOP, at the University of Amsterdam.

Mojtaba, with 10 years of experience as Research Engineer in the area of petroleum engineering industry, ‘Research and Development skills’, ‘Statistical data analysis’, ‘Project management skills’, ‘working with customers and different companies’, and ‘planning and organizing for coaching and leading the project’ are his key skills and strengths.

Scientific Publications

Journal Papers

- 1) **Hosseini-Nasab, S.M**, Padalkar, C., Battistutta, Zitha, P.L.J., "Mechanist Modelling of Alkaline/Surfactant/ Polymer Flooding Process at Sub-Optimum Salinity Condition for Enhanced Oil Recovery", journal of Industrial & Engineering Chemistry Research, (ACS), 2016, 55, pp 6875–6888.
- 2) **Hosseini-Nasab, S.M**, Zitha, P.L.J, Mirhaj, S.A, Simjoo, M., "A New Chemical Enhanced Oil Recovery Method?", Journal of Colloids and Surfaces A: Physicochemical and Engineering Aspects, Volume 507, 20 October 2016, Pages 89–95.
- 3) **Hosseini-Nasab, S.M**, Zitha, P.L.J , "Chemical-Foam Design as a Novel Approach Towards Immiscible Foam Flooding for Enhanced Oil Recovery", Just Accepted in journal of Energy and Fuels, ACS.
- 4) **Hosseini-Nasab, S.M**, Zitha, P.L.J , "Investigation of Certain Physical-Chemical Features of Oil Recovery by an Optimized Alkali-Surfactant-Foam (ASF) System for Enhanced Oil Recovery", Just Accepted in Journal of Colloid and Polymer Science. July, 2017.
- 5) **Hosseini-Nasab, S.M**, F. Douarache; M. Simjoo; L. Nabzar; B. Bourbiaux; P.L.J. Zitha, F. Roggero, "Numerical Simulation of Foam Flooding in Porous Media in Absence and Presence of Oil", Under review in the Journal of Fuel, Elsevier.

Conference Papers

- 1) **Hosseini-Nasab, S.M**, Zitha, P.L.J , "Chemical-Foam Design as a Novel Approach Towards Immiscible Foam Flooding for Enhanced Oil Recovery", Accepted to present in IOR 19th European Symposium on Improved Oil Recovery, Stavanger, Norway, 24-27 April 2017.
- 2) **Hosseini-Nasab, S.M**, Taal, M, Zitha, P.L.J , "Effect of Newtonian and Non-Newtonian Viscosifying Agents on the Stability of Foam for EOR - Part I: under Bulk Condition", Accepted to present in IOR 19th European Symposium on Improved Oil Recovery, Stavanger, Norway, 24-27 April 2017

- 3) **Hosseini-Nasab, S.M**, Chahardowli, M., Zitha, P.L.J , “Simplified Numerical Model for Simulation of Surfactant/Polymer (SP) Flooding Process for Enhanced Oil Recovery”, Presented in 78th EAGE Vienna Conference and Exhibition on 30 May-2 June 2016, Viena, Austria.
- 4) **Hosseini-Nasab, S.M**, Zitha, P.L.J, Mirhaj, S.A, Simjoo, M., “A New Chemical Enhanced Oil Recovery Method?”, SPE International Symposium on Oilfield Chemistry held in The Woodlands, Texas, USA, 13–15 April 2015.
- 5) **Hosseini-Nasab, S.M**, Zitha, P.L.J , “Systematic Phase Behaviour Study and Foam Stability Analysis for Optimal Alkaline/Surfactant/Foam Enhanced Oil Recovery”, IOR 18th European Symposium on Improved Oil Recovery, Dresden, Germany, 14-16 April 2015.
- 6) **Hosseini-Nasab, S.M**, Simjoo. M, Zitha, P.L.J, Douarche, F., Nabzar, L., “Numerical Simulation of Foam Flooding in Porous Media in Absence and Presence of Oil”, 8th International Conference on Porous Media & Annual Meeting (InterPore) on May 9 - 12, 2016, Cincinnati, Ohio, USA.
- 7) **Hosseini-Nasab, S.M**, Padalkar, C., Battistutta, E, Zitha, P., “Mechanist Modelling of Alkaline/Surfactant/ Polymer Flooding Process at Under-Optimum Salinity Condition for Enhanced Oil Recovery”, SPE Asia Pacific Enhanced Oil Recovery Conference (Malaysia, 11-13 Aug, 2015).
- 8) Al-Mudhafar, W.J, Rao, D.N, **Hosseini-Nasab, S.M** , “Optimization of Cyclic CO₂ Flooding through the Gas Assisted Gravity Drainage Process under Geological Uncertainties”, 15th European Conference on the Mathematics of Oil Recovery (ECMOR XV), 29 August - 1 September 2016, Amsterdam, Netherlands.
- 9) Al-Mudhafar, W.M, **Hosseini-Nasab, S.M** , “Lessons Learned from Numerical Modelling of IOR Steam flooding in a Bitumen-Light Oil Heterogeneous Reservoir”, IOR 2015 – 18th European Symposium on Improved Oil Recovery Dresden, Germany, 14-16 April 2015.